MODELING AND SIMULATION OF ION IMPLANTATION INDUCED DAMAGE

MOK KAI RINE, CAROLINE

NATIONAL UNIVERSITY OF SINGAPORE

2006

MODELING AND SIMULATION OF ION IMPLANTATION INDUCED DAMAGE

MOK KAI RINE, CAROLINE
(B. Eng (Hons.), NUS)

A THESIS SUBMITTED
FOR THE DEGREE OF DOCTOR OF PHILOSOPHY
DEPARTMENT OF CHEMICAL AND BIOMOLECULAR ENGINEERING
NATIONAL UNIVERSITY OF SINGAPORE

2006

Acknowledgements

In the course of this work, I am truly thankful and grateful to the many wonderful people I have had the honor of meeting, interacting with and learning from.

First, I wish to thank my supervisor, Associate Professor M. P. Srinivasan for his support, patience and kind guidance in my work at the National University of Singapore (NUS). Without him and the support from the Department of Chemical & Biomolecular Engineering, this work would not have been possible.

Secondly, I would like to thank those from the industry at Chartered Semiconductor Manufacturing (CSM). I am grateful to Dr Lap Chan for encouraging me to enter the intriguing world of microelectronics, to Dr Francis Benistant for introducing me to TCAD and for showing me the practical purpose of my work, to Dr Benjamin Colombeau for being helpful, supportive and for our many interesting discussions. Their infectious enthusiasm has provided the motivation that sustained me throughout this process.

In addition, this work would have been impossible without the guidance of Professor Martin Jaraiz and the support of the Department of Electronics, University of Valladolid (UVa). I am grateful to all for their hospitality and especially to members of the DADOS team for help with the software. I am grateful to Dr P. Castrillo, Dr J. E. Rubio, Dr R. Pinacho and Dr I. Martin-Bragado. I have benefited a lot from their deep knowledge in the field of modeling and simulation.

Furthermore, my scholarship from the Agency of Science, Technology and Research (A*STAR, Singapore) and support from Dr Jin Hongmei from the Institute of High Performance Computing (iHPC, A*STAR) are also gratefully acknowledged.

Validation of models and simulation results would have been impossible without

experimental data. I thank the many experimentalists, whose experimental data I have used to validate my work, especially to J. J. Hamilton, for exchange of ideas and for providing his experimental SIMS data.

I am grateful to all fellow students at NUS, UVa and CSM for all the fun and joy, especially to Chan H. Y., Serene and Yeong S. H., Allen, fellow chemical engineering students working with CSM. I thank them for teaching me, working with me, whining with me and keeping me sane.

Lastly, I would like to express my love and gratitude to my parents for supporting me in whatever I do.

Table of Contents

Page

Acknowledgements i

Table of Contents iii

Summary vii

List of Tables ix

List of Figures x

List of Symbols xvii

1 Introduction 1

1.1 Motivation 2

1.1.1 Challenges of Ultra-Shallow Junction Formation 2

1.1.2 Modeling and Simulation of Ion Implantation Induced Damage 6

1.2 Objectives 8

1.3 Overview 10

2 Background Literature 12

2.1 Defects in silicon 12

2.1.1 Point Defects 13

2.1.2 Amorphous Pockets 13

2.1.3 Extended Defects 18

2.2 Experimental observations of ion-implantation induced damage accumulation 22

2.3 Simulation techniques 28
2.3.1 Binary Collision Approximation 28
2.3.2 Molecular Dynamics 32
2.3.3 Continuum Approach 33
2.3.4 Kinetic Monte Carlo 34
2.4 Existing models of damage accumulation 38
2.4.1 Homogeneous Amorphization Mechanism 38
2.4.2 Heterogeneous Amorphization Mechanism 43
2.4.3 Dynamic Annealing 44
2.5 Conclusion 47
3 Model Description 48
3.1 Simulation Technique 48
3.2 Amorphous pockets 52
3.2.1 Structure 52
3.2.2 Rate of Amorphous Pocket Recrystallization . 53
3.2.3 Amorphous Pockets and Clusters 54
3.3 Amorphization 57
3.4 Recrystallization 61
3.4.1 Damage Smoothing 65
4 Effect of Defect Spatial Correlation 67
4.1 Introduction 68
4.2 Model 68
4.3 Results 69
4.4 Conclusion 76
5 Model Validation 77
5.1 Amorphous-Crystalline Transition Temperatures . . . 78
5.2 Noble Gas Effect 81

5.3 Amorphous Layer Thickness 83
5.3.1 Ge Preamorphization Implants 84
5.4 Dose Effect 90
5.5 Temperature dependence 94
5.6 Conclusion 99
6 Bimodal Distribution of Damage Morphology 100
6.1 Introduction 101
6.2 Model 101
6.3 Results 103
6.4 Conclusions 107
7 Extended Defects Simulations 108
7.1 Introduction 109
7.2 Model 111
7.3 Results 117
7.3.1 {311} defects 117
7.3.2 Non-amorphizing Si implantation 121
7.3.3 Amorphizing Si implantation 122
7.3.4 Damage Evolution of a Buried Amorphous Layer 126
7.4 Conclusion 130
8 Influence of SOI Structure on Defects 131
8.1 Introduction 131
8.2 Results 135
8.2.1 Damage evolution 135
8.2.2 Dopant Concentration Profile 136
8.2.3 Sheet Resistance 139
8.3 Discussion 142
8.4 Conclusion 145

9 Conclusion 146
9.1 Summary of work 146
9.2 Recommendations for future work 149
9.2.1 Effect of dopant atoms on damage 149
9.2.2 Effect of stress on damage 150
9.2.3 Effect of SOI on damage accumulation 151
Bibliography 152
Appendix 164

Summary

Ion implantation is a well-established processing technique in integrated circuit fabrication. However, this process induces extensive damage to the silicon crystal structure. Understanding of ion implantation induced damage is crucial as it affects device performance. In addition, modeling and simulation of ion implantation induced damage is complicated due to the many interdependent parameters and defect configurations. Defect production mechanisms, damage kinetics during ion implantation, damage evolution, amorphization and recrystallization must be accurately simulated in silicon and emerging new substrates such as silicon-on-insulator (SOI).

In order to model damage accumulation taking into account dynamic annealing, the most viable option is to use the binary collision approximation (BCA)/kinetic Monte Carlo (kMC) coupled simulation technique. The software that is used in this work incorporates an implant function that uses MARLOWE to generate the coordinates of the interstitials (I) and the vacancies (V) for each cascade. The coordinates of this damage are then fed into DADOS, a kMC simulator, which simulates defect reactions.

Central to this model are defect structures known as the amorphous pockets (AP). Instead of undergoing immediate recrystallization, I's and V's are assumed to form a distinct, disordered region (AP), preventing their diffusion when they are within a capture distance (second neighbor distance) of each other. Although the AP recrystallization rate is only size dependent, it is essential to preserve the I, V spatial correlation in the collision cascades to form the initial APs with a size distribution dependent on ion mass.

The parameters used in this model have been obtained from experimental

amorphous-crystalline transition temperatures for a range of implanted ions (C to Xe) to reproduce the experimentally observed dose rate effects. The thicknesses of the amorphous layers have also been well-simulated in a range of amorphizing conditions. In terms of the dose effect, the proportion of APs and amorphous regions as a function of dose, and the two-layered damage distribution along the path of a high-energy ion are consistent with experimental observations. Furthermore, this model is able to show that dynamic annealing is more effective at removing damage than post-cryogenic implantation annealing at the same temperature.

In addition, it was shown that different implant conditions can lead to different damage morphology. Since APs and clusters have different thermal stability, with clusters being more stable and hence more difficult to anneal, the same amount of damage with different morphology consequently leads to different annealing behavior.

An important aspect of damage evolution during post-implantation thermal annealing involves the transformation of extended defects from {311} defects to dislocation loops. Based on a size-dependent energy barrier, the transformation model has been successfully tested against experimental data.

Finally, it has been shown that the damage models developed in this work can be successfully used in technologically relevant processes involved in the formation of ultra-shallow junctions. Dopant concentration and activation calculated in terms of sheet resistance have been simulated in both bulk silicon and SOI. It was demonstrated that the buried oxide interface has an impact on both defect evolution and dopant diffusion and activation.

The good agreement between simulation results and various experimental data shows that the simulations are predictive and can provide valuable insights for process optimization.

List of Tables

3.1 Parameter values for interstitials and vacancies diffusion. 51

3.2 Parameter values of amorphous pocket defect recrystallization. . . . 53

3.3 Experimental activation energies for 80 keV implantation of silicon with various ions. From Ref. [Goldberg et al., 1995]. 55

3.4 Parameter values for the recrystallization of an amorphous-crystalline plane. 61

4.1 Details on implantation parameters used in the simulations to attain the same level of damage induced by C (10 keV) and Xe (80 keV). Dose rate and temperature were kept constant at $5\times10^{12}\,cm^{-2}s^{-1}$ and 100 K respectively. 71

7.1 Parameter values for the transition of {311} defects to dislocation loops. 113

List of Figures

1.1 Cross-section of an NMOSFET doping regions. 3

1.2 The implantation-diffusion interaction matrix. 5

2.1 Some configurations for (a) vacancy (b) interstitial (I) (c) dopant-interstitial pair (AI) when one of the dark spheres is a dopant atom (A). From Ref. [Fahey et al., 1989]. 14

2.2 Molecular dynamics simulation of 5 keV Si ion cascades in crystalline Si target. (a) 0.1 ps (b) 2.5 ps (c) 9 ps. The surface of the incoming ion is the (100) surface plane of the silicon lattice. Perpendicular line at the top surface of the box indicates the incoming direction of the ion. The computational cell is 13.5 nm on each edge, and contains 1.6×10^5 Si atoms. Only atoms with potential energy larger than 0.2 eV are plotted. From Ref. [Law et al., 2000]. 15

2.3 Molecular dynamics simulations showing atoms with potential energy higher than 0.2 eV for (a) 3 keV B and (b) 2 keV As implant in Si at 300 K after 10 ps. The damage energy is the same for both ions (1.3 keV). From Ref. [Caturla et al., 1996]. 16

2.4 Image of amorphous zones resulting from an impact of a single 200 keV Xe ion. (Total micrograph width = 30 nm) From Ref. [Donnelly et al., 2003]. 17

2.5 Cross-section high-resolution electron micrograph showing {311} defects. From Ref. [Eaglesham et al., 1994]. 19

2.6 Transmission electron microscopy micrographs showing faulted and perfect dislocation loops. From Ref. [Cristiano et al., 2000]. 20

2.7 Channeling Rutherford backscattering spectra of the same silicon implant at different substrate temperatures. Ref. [Schultz et al., 1991]. 23

2.8 Experimental crystalline-amorphous transition temperatures for (100) Si implanted with 80 keV ions to a fluence of 1×10^{15} ions/cm^2 for Si, Ar, Ge, Kr and Xe ions. Data points for carbon are for irradiations to 2×10^{15} ions/cm^2. From Ref. [Goldberg et al., 1995]. 26

2.9 Schematic drawing of two-body scattering theory in center-of-mass (CM) coordinates. 30

2.10 Schematic showing the energy barrier in a process that leads to a (a) higher-energy state and (b) lower-energy state. 35

2.11 Schematic showing the kMC algorithm that selects random events according to their corresponding rates. 36

2.12 Critical point defect density determined from the position of the amorphous-crystalline interface and simulated BCA point defect profiles. 39

2.13 Critical point defect density (CPDD) extracted from the measured depths of amorphous layers and BCA simulations. Figure from Ref. [Hobler and Otto, 2003]. 40

2.14 Dose dependence of damage produced by 100 keV Si^{+} ions in Si (100) single crystal at room temperature. Damage curves corresponding to both single alignment (SA) and double alignment (DA) Rutherford Backscattering Spectra (RBS) measurements, as well as the different damage components determined from the annealing results. From Ref. [Holland et al., 1989]. 41

2.15 <100> aligned spectra from Si(100) samples implanted at various doses with 1.25 MeV self-ions. From Ref. [Holland and White, 1991]. 42

2.16 Scheme of damage topology. Each gray circle represents an IV pair and the dashed lines their interaction radius. Isolated IV pairs (A) annihilate first as they do not have any IV neighbor. The amorphous pockets start recombining by the outer IV pairs (B and C) as the inner ones (F or H) have more IV neighbors. When an IV pair in a planar structure recombines, the whole layer regrows as the surrounding defects (D or E) have less IV neighbors than the other defects in the layer (G). From Ref. [Pelaz et al., 2003]. 45

3.1 Schematic showing the division of three-dimensional space in DADOS into small BitBoxes. 50

3.2 Amorphous pockets are irregularly-shaped agglomerates of interstitials and vacancies, formed when the point defects are within an interaction radius of each other. Dashed line represents the interaction radius. 52

3.3 Activation energy of recrystallization as a function of size of the amorphous pockets. 55

3.4 Amorphous pockets formed in simulation. (a) In terms of I (yellow) and V(green) (b) In terms of the number of IV pairs. 56

3.5 Schematic showing the consistent treatment of APs and clusters. Once an AP is completely recrystallized, remaining I or V behave as pure clusters (point defect capture/emission). Pure cluster can transform back into AP by capturing defect of the opposite type within its capture radius. 56

3.6 Simulated damage (total I+V) profiles for 200 keV B implant at 100 K and a dose rate of 1.25×10^{12} cm^{-2}s^{-1}. (a) Up to the critical dose of 1×10^{15} cm^{-2}. (b) Up to a dose of 5×10^{14} cm^{-2}. Dimension of BitBox: 0.977 nm × 0.938 nm × 0.938 nm. 59

3.7 Simulated damage (total I+V) profiles for 200 keV B implant at 100 K and a dose rate of 1.25×10^{12} cm^{-2}s^{-1}. (a) Up to the critical dose of 1×10^{15} cm^{-2}. (b) Up to a dose of 5×10^{14} cm^{-2}. Dimension of BitBox: 0.977 nm × 1.875 nm × 1.875 nm. 60

3.8 Source and gate time evolution of a transistor during a 600 °C anneal, following a typical Ge pre-amorphization implant at 20 keV, 1×10^{15} cm^{-2} (RT and a dose rate of 1×10^{13} cm^{-2}s^{-1}). Snapshots show annealing at (a) t=0 s, (b) t=20 s, (c) t=40 s, (d) t=60 s, (e) t=80 s and (f) t=100 s. White represents amorphous damage, yellow represents amorphous pockets and red represents {311} defects. . . 63

3.9 Source and gate time evolution of a transistor during a 600 °C anneal, following a non-amorphizing Ge implant at 20 keV, 5×10^{13} cm^{-2} (RT and a dose rate of 1×10^{13} cm^{-2}s^{-1}). Snapshots show annealing at (a) t=0 s, (b) t=20 s, (c) t=40 s, (d) t=60 s, (e) t=80 s and (f) t=100 s. Yellow represents amorphous pockets. 64

3.10 Simulated damage (total I+V) profiles for 200 keV B implant at 100 K and a dose rate of 1.25×10^{12} cm^{-2}s^{-1} without damage smoothing, up to the critical dose of 1×10^{15} cm^{-2}. Dimension of BitBox: 0.977 nm × 0.938 nm × 0.938 nm. 66

4.1 AP histograms obtained from C (lines with symbols) and Xe (dotted lines) implants using BCA at different damage concentrations. Implantations were simulated with conditions specified in Table 4.1. 70

4.2 Normalized AP distribution obtained from Xe implants using BCA at different damage concentrations. Implantations were simulated with conditions specified in Table 4.1. 72

4.3 2D color maps showing the AP size distribution at a constant damage of 1×10^{20} cm^{-3} generated by BCA implants of (a) C and (b) Xe. 74

4.4 AP histograms at a constant damage concentration of 1×10^{20} cm^{-3}, of BCA H, C and Xe implants and by loading damage profiles of C and Xe. 75

5.1 Simulation (lines) compared to experimental data (symbols) from Ref. [Goldberg et al., 1995] for amorphous-crystalline transition temperatures as a function of dose rate, for (100) silicon implanted with 80 keV ions to a dose of $1 \times 10^{15}\,\mathrm{cm}^{-2}$ for Si, Ar, Ge, Kr and Xe, and $2 \times 10^{15}\,\mathrm{cm}^{-2}$ for C. 79

5.2 Activation energy of recrystallization as a function of ion mass from experimental data [Goldberg et al., 1995]. (Lines drawn to guide the eyes.) 82

5.3 Sequence of simulations showing the development of the amorphous layer in silicon with increasing dose of 300 keV Si (a) $1 \times 10^{15}\,\mathrm{cm}^{-2}$, (b) $2 \times 10^{15}\,\mathrm{cm}^{-2}$, (c) $5 \times 10^{15}\,\mathrm{cm}^{-2}$, implanted at 300 K with a dose rate of $1.5 \times 10^{12}\,\mathrm{cm}^{-2}\mathrm{s}^{-1}$. White represents amorphous regions and yellow represents amorphous pockets. 86

5.4 Simulated amorphous layer thickness as a function of dose rate for 80 keV, $1 \times 10^{15}\,\mathrm{cm}^{-2}$ Si implant at room temperature. 87

5.5 Amorphous layer thickness as a function of implant energy for Ge PAI at a dose of $1 \times 10^{15}\,\mathrm{cm}^{-2}$. Simulations were done at room temperature and at a dose rate of $1 \times 10^{13}\,\mathrm{cm}^{-2}\mathrm{s}^{-1}$. Filled symbols represent experimental data [Pawlak et al., 2002, Cristiano et al., 2004, Lindsay et al., 2004, Hamilton et al., 2005], open symbols are from simulations. Experimental characterization methods are indicated when specified. 88

5.6 Amorphous layer thickness as a function of dose for 150 keV Ge PAI. Simulations were done at room temperature and at a dose rate of $1 \times 10^{13}\,\mathrm{cm}^{-2}\mathrm{s}^{-1}$. Filled symbols represent experimental data measured by TEM [Colombeau et al., 2001], open symbols are from simulations. 89

5.7 Dose dependence of damage produced by 100 keV Si ions at room temperature and a dose rate of $5 \times 10^{12}\,\mathrm{cm}^{2}$. Symbols show different damage components determined from the experimental annealing results, dotted lines are results obtained from simulations. Experimental data from Ref. [Holland et al., 1989]. See also Fig. 2.14. . . 91

5.8 Simulated damage profile resulting from 1 MeV Si implantation at room temperature at various doses. 93

5.9 Simulated normalized damage as a function of temperature for 80 keV C implantations. Post-cryogenic implantation annealing represents 10 minutes annealing after cryogenic temperature implantation. . . . 95

5.10 2D histograms of APs composition at (a) cryogenic (-150 °C) C implantation to a dose of 2×10^{14} cm^{-2}, (b) post-cryogenic implantation annealing at 20 °C, (c) 20 °C C implantation to a dose of 1×10^{15} cm^{-2} (dynamic annealing). 98

6.1 2D histogram of AP composition of an amorphizing 80 keV Carbon implant at (a) 10% and (b) 80% of the total dose of 2×10^{15} cm^{-2}. Simulations were done at 20 °C and at a dose rate of 5×10^{12} cm^{-2}s^{-1}.102

6.2 2D histograms of AP composition showing damage composition at a constant damage level of 1×10^{21} cm^{-3}, resulting from 80 keV Si implant at a dose rate of 5×10^{12} cm^{-2}s^{-1}. (a) Implant temperature of -100 °C and dose of 1×10^{13} cm^{-2} (b) Implant at room temperature and a dose of 1×10^{14} cm^{-2} (c) Implant temperature of 200 °C and dose of 1×10^{15} cm^{-2}. 105

6.3 Annealing behavior of damage induced by room temperature implant and by 200 °C implant at 800 °C. 106

7.1 Formation energies of the different extrinsic defects as a function of their size from Ref. [Calvo et al., 2004]. FDL: Faulted dislocation loops. PDL: Perfect dislocation loops. 112

7.2 Energy barrier for the transformation from {311} defects to dislocation loops as a function of the size (number of interstitials, y) of the {311} defects. 114

7.3 The resulting transition rate, $R(y)$, at 800 °C. 114

7.4 Examples of size distribution, $g(y)$ of two different defect populations, with mean size of 300 and mean size of 2500. 115

7.5 Transformation rate as a function of the size of the {311} defects, $R(y)\times g(y)$ at 800 °C. 115

7.6 Number of interstitials in {311} defects as a function of time at various temperatures after 40 keV, 5×10^{13} cm^{-2} Si . Symbols represent experimental data and lines represent simulations. Experimental data is obtained from [Stolk et al., 1997]. 118

7.7 Interstitial supersaturation as a function of annealing time at various tempeartures after 40 keV, 2×10^{13} cm^{-2} Si implantation. Symbols represent experimental data and lines represent simulations. Experimental data from [Cowern et al., 1999c]. 119

7.8 Cross-sectional images showing the damage morphology after 40 keV, $6 \times 10^{13}\,cm^{-2}$ Si implantation, followed by annealing for 30 min at 740 °C. (a)Experimental image from Ref. [Colombeau et al., 2003]. (b) Simulation from DADOS showing only {311} defects and no dislocation loops. Scale for both (a) and (b): 200 nm × 200 nm. . . 120

7.9 Time evolution of the amount of interstitials in extended defects for the 800 °C anneal that follows a non-amorphizing 100 keV, $2 \times 10^{14}\,cm^{-2}$ Si implant. Symbols represent experimental data from Ref. [Li and Jones, 1998]. Simulation results are plotted as lines and have been divided by 3. 123

7.10 Plan-view of {311} defects and dislocation loops corresponding to the anneal of Fig. 7.9 after 10 minutes. (a) TEM image from Ref. [Li et al., 1998]. (b) Simulated plan-view. Scale for both (a) and (b): 100 nm x 100 nm. 124

7.11 Time evolution of the amount of interstitials in extended defects for the 750 °C anneal that follows a Si 20 keV, $1 \times 10^{15}\,cm^{-2}$ amorphizing implant. Symbols represent experimental data from Ref. [Robertson et al., 2000]. Simulation results are plotted as lines and have been divided by 2. 125

7.12 Comparison between experimental x-TEM [Pan and Tu, 1997] and simulation for as-implanted samples. Letters s and a/c indicate the implanted surface and the location of the as-implanted amorphous-crystalline interface. The same scale is used for both images, whereby the simulation width is 50 nm. In the simulation, white represents amorphous damage and yellow represents amorphous pockets. . . . 128

7.13 Comparison between experimental x-TEM [Pan and Tu, 1997] and simulation after 1 s, 800 °C. In the simulation, yellow represents amorphous pockets and red represents {311} defects. 128

7.14 Comparison between experimental x-TEM [Pan and Tu, 1997] and simulation after 60 s, 800 °C. 129

7.15 Comparison between experimental x-TEM [Pan and Tu, 1997] and simulation after 120 s, 900 °C. A dislocation loop is shown in the simulation. 129

8.1 Simulated damage (interstitial) concentration profile of as-implanted 8 and 20 keV Ge, followed by 500 eV B. The saturated ($\approx 1 \times 10^{22}\,cm^{-3}$) level corresponds to amorphized material. 136

8.2 Simulated plan-view of defects in bulk Si corresponding to 60 s anneal at (a) 700 °C (b) 800 °C (c) 900 °C of damage induced by 20 keV Ge preamorphization implant at a dose of 1×10^{15} cm^{-2}, followed by 500 eV B at a dose of 2×10^{15} cm^{-2}. Scale: 80 nm x 80 nm. Yellow represents APs, red represents {311} defects and green represents dislocation loops. 137

8.3 Simulated plan-view of defects in SOI corresponding to 60 s anneal at (a) 700 °C (b) 800 °C (c) 900 °C of damage induced by 20 keV Ge preamorphization implant at a dose of 1×10^{15} cm^{-2}, followed by 500 eV B at a dose of 2×10^{15} cm^{-2}. Scale: 80 nm x 80 nm. Yellow represents APs, red represents {311} defects and green represents dislocation loops. 138

8.4 B concentration profile for 20 keV Ge PAI samples after 60 s, 850 °C anneal in (a) Bulk Si (b) SOI. Experimental SIMS obtained from Ref. [Hamilton et al., 2005] 140

8.5 Sheet resistance as a function of annealing temperature, after 60 s isochronal anneal. (a) 8 keV Ge PAI (b) 20 keV Ge PAI. Experimental points from Ref. [Hamilton et al., 2005] 141

8.6 Two-dimensional view of a simulated source-drain extension formed in bulk Si and SOI (55 nm) with 20 keV 1×10^{15} cm^{-2} Ge PAI, followed by 500 eV 2×10^{15} cm^{-2} B. (a) 750 °C anneal for 5 min (b) spike anneal up to 1050 °C. (White represents B.) 144

List of symbols

α	prefactor parameter of the amorphous pockets recystallization rate
β	exponent parameter of the amorphous pockets recrystallization rate
ϕ	screening function
Φ	angle of recoil in binary collision approximation
γ	parameter of energy barrier for {311} defect to dislocation loop
λ	second neighbor distance
μ	hole mobility
ν_{recrys}	recrystallization velocity
Θ	angle of scatter in binary collision approximation
ω_o	proportionality constant
a	screening length
a_o	Bohr radius
a_u	universal screening length
C_B	carrier concentration
D_m	point defect diffusivity
D_{mo}	prefactor parameter of point defect diffusivity
E0	parameter of energy barrier for {311} defect to dislocation loop transition
E1	parameter of energy barrier for {311} defect to dislocation loop transition
E	energy barrier for {311} defect to dislocation loop transition
E_{act}	activation energy
E_c	initial kinetic energy of ion in center-of-mass coordinates
E_{ion}	energy of ion
E_m	parameter of activation energy for point defect diffusivity
E_o	initial kinetic energy of ion
E_{recrys}	activation energy of recrystallization

g	size distribution of defect population
k	Boltzmann's constant
k_e	constant in the electron energy loss calculation
K	parameter in the Oen-Robinson formula
m	number of vacancies in an amorphous pocket
M_1, M_2	ion mass
n	number of interstitials in an amorphous pocket
N	total number of possible events in the kinetic Monte Carlo algorithm
p	impact parameter in binary collision approximation
P	probability of event in the kinetic Monte Carlo algorithm
q	electronic charge
R0	prefactor parameter in the transition rate of {311} defect to dislocation loop
r	interatomic separation
r_i	rate of individual events in the kinetic Monte Carlo algorithm
r_{min}	minimum interatomic separation
R	transition rate of {311} defect to dislocation loop
R_N	cumulative rate in the kinetic Monte Carlo algorithm
R_s	sheet resistance
s	effective size of amorphous pockets
S_E	electron energy loss
T	temperature (Kelvin)
T_{atom}	energy transferred in a collision from an incident projectile to the target
T_c	amorphous-crystalline transition temperature
V	potential energy
V_0	initial velocity of projectile ion
V_C	system velocity in the center-of-mass coordinates
$V_{0,recrys}$	prefactor parameter of the recrystallization velocity

x	depth of implant
x_j	junction depth
y	number of interstitials in {311} defects
y_o	crossover size between the formation energies of {311} defects and dislocation loops
Z_1, Z_2	atomic number

Chapter 1

Introduction

The phenomenal growth of the semiconductor industry is driven by technological advances that fabricate ever smaller and faster transistors. These smaller devices deliver better performance at lower cost per function. In the competitive world of consumer electronics, the most advanced technologies are essential for both the central processing unit (CPU) and memory requirements. This is only possible with the drastic integration of complementary metal-oxide semiconductor (CMOS) transistors. Today, 65 nm technology devices are already in production, while the 45 nm technology devices would soon be in 2007. These devices are being developed and manufactured not only on 300 mm bulk silicon wafers, but also on silicon-on-insulator (SOI) wafers. The typical gate length for the 65 nm technology is below 50 nm and for the 45 nm technology, it is below 35 nm. According to the 2005 edition of the International Technology Roadmap for Semiconductors (ITRS), physical gate length of devices will scale further down to less than 10 nm in the year 2016 [Semiconductor Industry Association, 2005]. The main issue faced when fabricating such advanced technology devices is the cost of development. Due to the escalating cost of fabrication, it becomes increasingly important for foundries to use less silicon to optimize and yield their processes. The key to overcome this is to rely on predictive process simulators. This is why there is great interest in atomistic process simulation, which can incorporate the physics of the implantation and diffusion steps to accurately predict junction profiles and thus transistor performance.

1.1 Motivation

1.1.1 Challenges of Ultra-Shallow Junction Formation

The typical front-end processing for metal-oxide semiconductor field-effect transistors (MOSFETs) includes etching, oxidation, ion implantation, diffusion and thin film deposition. Among these processes, ion implantation and annealing are especially important, since the formation of ultra-shallow junctions is one of the keys to achieving sub-50 nm MOSFETs [Koyanagi, 2000].

Ion implantation is a well-established processing technique in integrated circuits (IC) fabrication for the controlled doping of silicon. It is a process in which energetic, charged atoms (or molecules) are directly introduced into a substrate. A typical CMOS process employs dozens of ion implantation steps to form, for example, retrograde wells, source/drain junctions and extensions, and *halo* implants. Retrograde well is an approach to well formation whereby the highest concentration of dopant in the well is located at a certain distance from the surface. *Halo* implants are necessary to increase the abruptness of the source-drain extension junction doping profile, decrease the junction depth and increase the punch-through voltage. In *halo* implants, dopant of the same type as the major well dopant is implanted beneath the source-drain extension junction. Figure 1.1 shows the doped regions of an NMOSFET.

However, implanting high-energy ions into a silicon substrate induces extensive damage to the crystal structure through nuclear collisions between the incoming ions or recoils (Si atoms that have been displaced by another high-energy projectile ion) and the lattice atoms. The as-implanted damage exhibits several different damage configurations ranging from isolated point defects, point defect clusters, amorphous pockets surrounded by crystalline silicon to a continuous amorphous layer. A subsequent high temperature annealing step is required to remove the damage to maintain good electrical properties. In addition, since most as-implanted

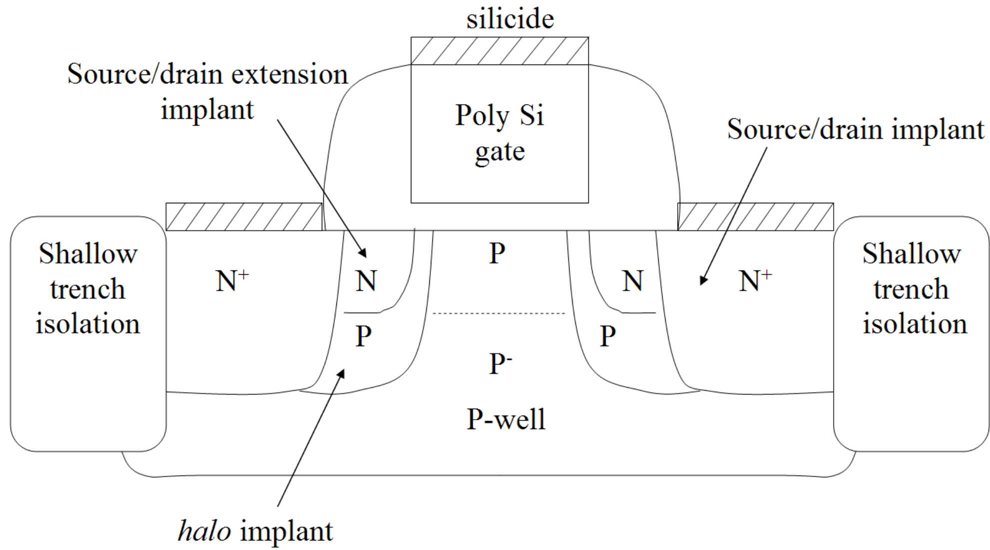

Figure 1.1: Cross-section of an NMOSFET doping regions.

dopant atoms do not occupy substitutional sites, this annealing step also serves to bring about electrical activation.

Understanding of ion implantation induced damage is crucial as it affects final junction properties, such as dopant profile and dopant activation. Defects induced by ion implantation are known to interact with dopant atoms, contributing to dopant clustering and transient enhanced diffusion (TED) of the dopant [Stolk et al., 1997]. For the case of boron, damage induced by ion implantation is known to retard boron activation to concentrations well below the equilibrium solid solubility [Solmi et al., 1991].

TED is a phenomenon observed during the post-implantation annealing step. As dopant diffusion is defect-mediated, the implanted dopants experience enhanced diffusion in the presence of defects generated by the ion implantation step. Since ion implantation generates a net excess of interstitials, TED significantly affects dopants whose diffusion mechanisms are predominantly interstitial-mediated. Boron is a classical example of interstitial-mediated TED in silicon.

Mechanisms of boron TED are such that a silicon interstitial "kicks out" the substitutional boron atom to an interstitial site where it can diffuse easily. Alternatively, silicon interstitials and boron atoms form highly mobile pairs. In both cases, silicon interstitials are required for the diffusion of boron [Stolk et al., 1997, Jain et al., 2002]. The silicon interstitials for dopant TED may come directly from the ion implantation process or during the formation and dissolution of extended defects, like the {311}s defects [Eaglesham et al., 1994] and the dislocation loops [Bonafos et al., 1997]. Detailed explanations of these defects will be provided in the following chapter. The impact of ion implantation induced damage becomes more crucial with shrinking devices, as TED dominates dopant diffusion and limits the reduction in junction depths.

The key to the formation of ultra shallow junctions is an optimum trade-off between minimizing dopant diffusion while sufficiently activating the implanted dopant and removing the damage. The complex interaction between dopants and defects is schematically shown in Fig. 1.2 [Jones and Rozgonyi, 1993]. Activation is related to the fraction of dopant atoms that are on substitutional lattice sites acting as donors or acceptors. Thus, maximum electrical activation could be attained up to the dopant solubility limit. In order to achieve dopant activation and remove damage, high annealing temperatures are required, which in turn leads to significant diffusion.

One main method of forming highly-active, ultra-shallow junctions is to implant dopants into preamorphized silicon, followed by a low temperature solid phase epitaxial regrowth (SPER) process [Jin et al., 2002, Lindsay et al., 2004]. Germanium is often employed in preamorphization implants. At sufficiently high dose, the implantation-induced damage can result in crystalline to amorphous phase transition. The amorphous silicon reduces dopant channeling, resulting in abrupt, shallow profiles. Subsequent SPER at low temperature recrystallizes the amorphous layer, allows only slight dopant diffusion and incorporates dopant atoms in the

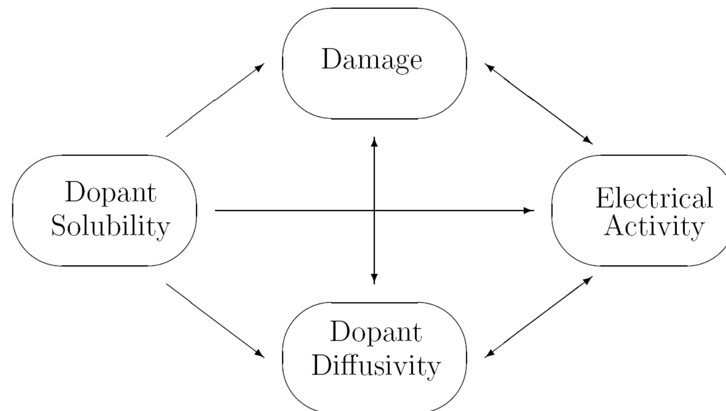

Figure 1.2: The implantation-diffusion interaction matrix.

amorphous layer into substitutional lattice sites at high metastable concentrations that are above the equilibrium solid solubility limit [Tsai and Streetman, 1979, Narayan et al., 1983]. Beyond the amorphous-crystalline interface in the heavily-damaged but still crystalline region, defects may evolve into extended defects, like {311} defects or dislocation loops depending on the annealing condition. These defects are known as the end-of-range defects.

In addition to preamorphization implants, it is important to understand amorphization, as high dose (As or BF_2) implantation used to reduce sheet resistance, is likely to form surface amorphous layers when implantation is done in a crystalline substrate. Sheet resistance is a material property that is typically used to measure the amount of dopant activation.

The presence of the end-of-range defects in devices is detrimental to the formation of ultra-shallow junctions as they affect reliability and electrical characteristics. Thus, it is vital to remove them by thermal annealing. However, as the thermal process would also lead to dopant diffusion and hence junction depth increase, it is necessary to estimate the minimum thermal budget required to achieve the complete dissolution of the end-of-range defects. The amount, location and the annealing properties of these defects are important factors in determining the ther-

mal budget requirements. Moreover, due to dopant-defect interaction, the extent of diffusion and activation of the implanted dopants are affected by these factors as well.

Therefore it is essential to develop models for ion implantation induced amorphization, which are able to accurately reproduce the amorphous-crystalline transition, as well as the depth of the amorphous layer, which determines the amount and location of the end-of-range defects.

Furthermore, with the increasing use of new silicon-related substrates like silicon-on-insulator (SOI) in the fabrication of transistors, it is essential to understand the impact of a buried oxide interface on defect evolution and dopant diffusion.

1.1.2 Modeling and Simulation of Ion Implantation Induced Damage

The physical processes, namely ion implantation and annealing, involved in junction formation are complex. Front-end process modeling for nanometer structures has been identified in the ITRS 2005 as one of the "Grand Challenges" for enhancing performance:

> "Front-end process modeling for nanometer structures is a key challenge for the prediction of device performance. [...] Most important and challenging in the area of front-end process modeling is the modeling of ultra-shallow junction formation, which starts from very low energy implant and especially focuses on the thermal annealing, diffusion and activation of dopants under implantation damage and stress. Due to the strongly reduced thermal budgets needed for shallow junction, the junction formation process is highly transient and is governed by the diffusion and reaction of dopant atoms and defects, and especially by the dynamics of clusters of dopant atoms and defects. Implantation damage, amorphization, re-crystallisation, and silicidation must be ac-

curately simulated."

Any modern junction formation process must be capable of creating good quality *pn* junctions, in which the final junction depth is controllable and reproducible. Modeling of front-end processing provides a method capable of predicting final junction properties, such as junction depth, dopant profile and dopant activation. This requires the understanding and prediction of both the amount and the location of any process-induced defects.

With ever smaller devices, it is increasingly difficult and expensive to study or characterize with experimental techniques alone. Moreover, the cost of fabrication of test lots increases with each technology generation, making process optimization by the usual trial and error method extremely expensive. On the other hand, computational capability has been steadily increasing. With suitable models based on the physical understanding of actual processes, one can simulate and quite accurately reproduce them. Therefore, accurate simulation of front-end processing is essential to IC technology development, because it can provide valuable guidance during the design phase for new devices and replace extensive optimization experiments with virtual ones.

1.2 Objectives

Understanding and having the capability of predicting the detailed nature and three-dimensional (3D) distribution of the damage induced in silicon by ion implantation is crucial to the accurate atomistic simulation of silicon front-end processing. This encompasses defect production mechanisms, evolution of the damage, as well as the physical mechanisms of damage accumulation and phase transformation.

The many and interdependent implantation parameters, like implant species, energy, dose, dose rate and wafer temperature would affect the kinetics of damage accumulation. A single accurate model should properly account for experimental observations, taking into account the dynamic annealing process that results in experimentally observed dose rate effects [Schultz et al., 1991, Goldberg et al., 1995]. According to ITRS 2005,

> "[...], modeling needs to be extended to include damage kinetics during ion implant process step and subsequent process in silicon silicon-related materials."

The objectives covered in this work can be summarized in the following points:

1. Develop an accurate model for the dynamic annealing mechanism for the ion implantation induced damage accumulation up to amorphization, by the recrystallization of defect structures, known as the amorphous pockets. Obtain model parameters from the experimental amorphous-crystalline transition temperatures for a range of implanted ions and reproduce the experimentally observed dose rate effects.

2. Demonstrate that the model can correctly simulate a range of experimental observations of damage accumulation.

3. Analyse the defect structure (amorphous pockets) in the simulation to attain theoretical understanding at an atomistic level inaccessible experimentally.

4. Model the extended defects, specifically of the transition of {311} defects to dislocation loops. Since there are two possible evolutionary pathways for {311} defects, namely dissolution and transition to dislocation loops, process models must account for both these mechanisms in order to accurately predict diffusion of dopant atoms.

5. Simulate a diversity of technologically relevant process conditions, including amorphization, defect evolution, dopant-defect interaction in both bulk silicon and SOI. Verify the simulated dopant concentration profiles and sheet resistance with the experimental ones.

1.3 Overview

This thesis can be broken down into the following chapters.

Chapter 1: Introduction highlights the main motivations and objectives of this work. A brief review is presented on the challenges facing the formation of ultra-shallow junctions in terms of ion implantation and annealing. Furthermore, the importance of front-end process modeling and simulation is addressed.

Chapter 2: Background Literature provides a review of the background scientific literature relevant in developing an ion implantation induced damage accumulation model. Firstly, an overview of the different defect types in silicon is presented. Secondly, some interesting experimental observations of the dependence of ion implantation parameters on damage accumulation are shown. Thirdly, various useful simulation techniques are briefly summarized. Finally, some damage accumulation models that have been developed are introduced.

Chapter 3: Model Description describes the simulation technique and the amorphous pockets, which are central to the damage accumulation model that is used to obtain simulation results in the following chapters. Following that, the amorphization and recrystallization models are explained.

Chapter 4: Effect of Defect Spatial Correlation provides a better understanding of the amorphous pocket model by comparing the initial damage morphology generated by ions of different masses. This chapter further addresses the importance of the spatial correlation of the interstitials and vacancies for this model.

Chapter 5: Model Validation presents simulation results of a variety of experimental observations, validating the damage accumulation model.

In **Chapter 6: Bimodal Distribution of Damage Morphology**, the model is used to analyse the composition and size distribution of amorphous pockets following different conditions of ion implantation and their implications for subsequent thermal annealing.

Chapter 7: Extended Defects Simulations shows the transformation of {311} defects into dislocation loops, with a transformation rate that is controlled by a size-dependent energy barrier. Simulated damage evolution for a series of thermal annealings are remarkably similar to experimental observations.

Chapter 8: Influence of SOI Structure on Defects shows simulations for technologically relevant process conditions, like Ge pre-amorphization implant and solid phase epitaxial regrowth, in the formation of ultra-shallow junctions. In addition, the influence of SOI structure on damage evolution and junction electrical characteristics are predicted from simulations and compared with experimental results.

Finally, **Chapter 9: Conclusion** ends the thesis and offers recommendations of possible future work that can be attempted.

Chapter 2

Background Literature

In this chapter, a review of the relevant literature in developing an ion implantation induced damage accumulation model in silicon is summarized. Firstly, as damage induced by ion implantation can exist in different configurations, an overview of the different defect types in silicon is presented. Secondly, some interesting experimental observations of the dependence of ion implantation parameters, like ion mass, dose, dose rate and temperature, on damage accumulation is shown. Thirdly, a brief summary of the various simulation techniques that can be used in simulating damage accumulation is given. Lastly, various damage accumulation models that have been developed over the years to explain different experimental observations and to account for dynamic annealing are introduced. A comprehensive review can be found in Ref. [Hobler and Otto, 2003] and [Pelaz et al., 2004].

2.1 Defects in silicon

Nuclear-stopping process of ions implanted into silicon crystal is responsible for producing displacement damage, as atoms from the crystal lattice are displaced, resulting in interstitials and vacancies (Frenkel pairs). Depending on the implant conditions, implantation cascades generate different damage configurations ranging from isolated point defects, point defect clusters, amorphous pockets surrounded by crystalline silicon, and continuous amorphous layer. Upon annealing, extended defects like {311} defects and dislocation loops can also be observed. In this section, a concise review of the different types of defects in silicon is presented.

2.1.1 Point Defects

Dopant diffusion in silicon is mediated by point defects [Fahey et al., 1989]. From fundamental thermodynamics, at any temperature $T > 0\,K$, vacancies and interstitials would exist in thermal equilibrium in an otherwise perfect silicon crystal.

A vacancy is an empty lattice site, while an interstitial is an extra atom in the lattice structure. Isolated vacancies, in their V^+ and V^- charged states, have been observed by electron paramagnetic resonance (EPR) and deep-level transient spectroscopy (DLTS) at low temperature after electron irradiation. Although interstitials have not been directly observed by EPR, their presence has been implied from interactions with impurities.

Both types of point defects can adopt different configurations and charge states depending on the Fermi level. Figure 2.1 shows some configurations of the vacancy and interstitial point defect. Figure 2.1(c) schematically shows dopant interstitialcies. In order to determine the thermodynamic and transport properties of the vacancies and self-interstitials in silicon, several experimental works [Bracht et al., 1995] and first-principles calculations [Blöchl et al., 1993] have been done. Detailed reviews on the point defects can be found in Ref. [Fahey et al., 1989, Hu, 1994, Watkins, 2000].

2.1.2 Amorphous Pockets

Single cascades in semiconductors studied in silicon by molecular dynamics (MD), results in the production of amorphous pockets, as well as isolated point defects and small purely interstitial or vacancy clusters. Amorphous pockets are disordered regions surrounded by crystalline silicon. Figure 2.2 shows MD simulations of the collision of a 5 keV silicon atom with a crystalline silicon substrate [Diaz de la Rubia and Gilmer, 1995]. The surface of the incoming ion is the (100)

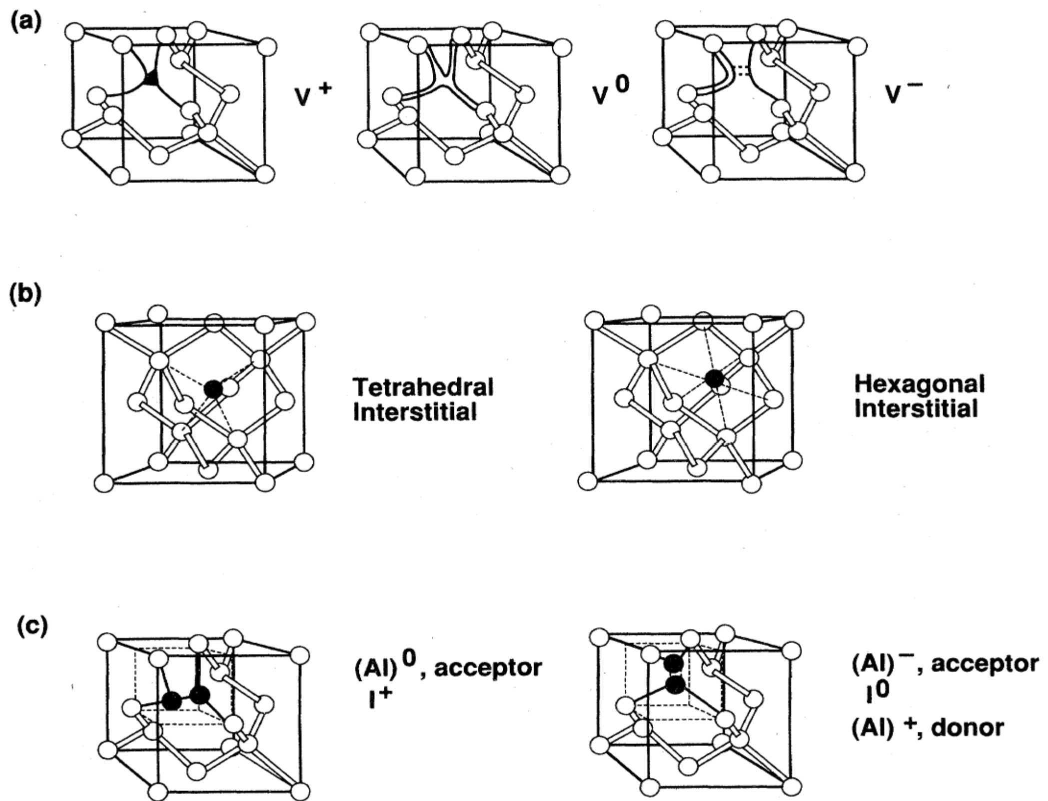

Figure 2.1: Some configurations for (a) vacancy (b) interstitial (I) (c) dopant-interstitial pair (AI) when one of the dark spheres is a dopant atom (A). From Ref. [Fahey et al., 1989].

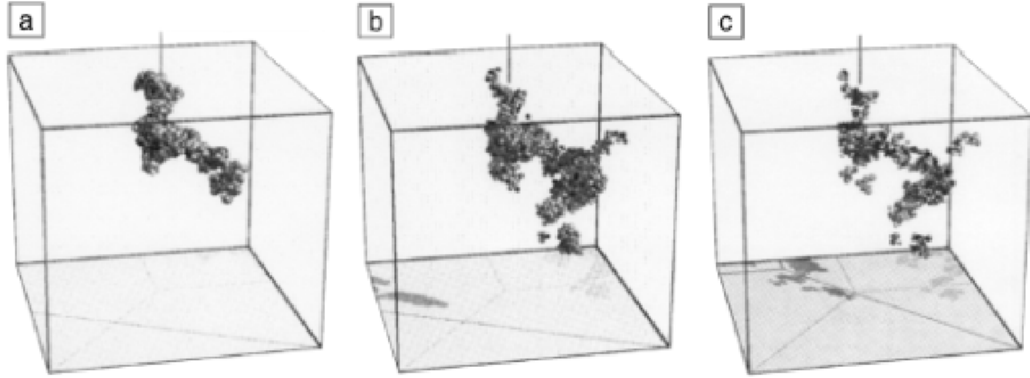

Figure 2.2: Molecular dynamics simulation of 5 keV Si ion cascades in crystalline Si target. (a) 0.1 ps (b) 2.5 ps (c) 9 ps. The surface of the incoming ion is the (100) surface plane of the silicon lattice. Perpendicular line at the top surface of the box indicates the incoming direction of the ion. The computational cell is 13.5 nm on each edge, and contains 1.6×10^5 Si atoms. Only atoms with potential energy larger than 0.2 eV are plotted. From Ref. [Law et al., 2000].

surface plane of the silicon lattice. Perpendicular line at the top surface of the box indicates the incoming direction of the ion. The computational cell is 13.5 nm on each edge, and contains 1.6×10^5 Si atoms.Only atoms of the target with more than 0.2 eV of potential energy are shown. The damage in (a) corresponds to a time of 0.1 ps after the first collision, (b) to 2.5 ps, and (c) to 9 ps. The impact initially results in local melting in the cascade core. When these liquid-like zones cool down, they form large local amorphous pockets and a few isolated, freely migrating defects. A detailed MD study of damage production in silicon by collision cascades implanted with an energy of a few keV, showed that most of the isolated point defects are interstitials and the amorphous pockets are vacancy-rich and have on average a little less atoms than perfect silicon [Nordlund et al., 1998].

MD studies also showed that these highly disordered amorphous pockets, which are surrounded by crystalline material, are highly unstable. As a result, they recrystallize very quickly at much lower temperatures than a planar amorphous-crystalline interface (≈500°C). This is in good agreement with experimental evidence [Priolo et al., 1990a, Donnelly et al., 2003]. Simulated annealing of the amor-

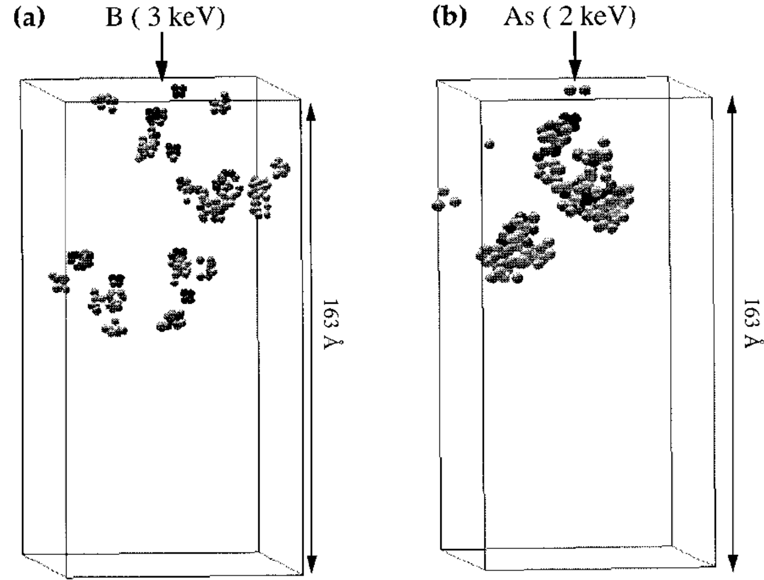

Figure 2.3: Molecular dynamics simulations showing atoms with potential energy higher than 0.2 eV for (a) 3 keV B and (b) 2 keV As implant in Si at 300 K after 10 ps. The damage energy is the same for both ions (1.3 keV). From Ref. [Caturla et al., 1996].

phous pockets at elevated temperatures indicates that the shrinkage of the amorphous pockets takes place mainly through internal reordering ("recombination"), rather than through the emission of point defects. During annealing, these amorphous regions collapse into clusters of interstitials and vacancies. Only when the amorphous pocket is left with the excess interstitials (I) or excess vacancies (V), do clustering and subsequent point defect emission begin. Therefore, recrystallization of the amorphous pockets can occur without the intervention of point defects external to them.

Caturla et al. showed using MD that when implanting B and As ions of the same damage energy into crystalline silicon, the resulting damage morphology has a strong dependence on ion mass, as shown in Fig. 2.3 [Caturla et al., 1996]. In the case of the B cascade, a number of isolated Frenkel pairs and small clusters are observed. In the case of As and other high mass ions such as In and Sb, the damage is mostly in the form of large amorphous pockets with few isolated defects,

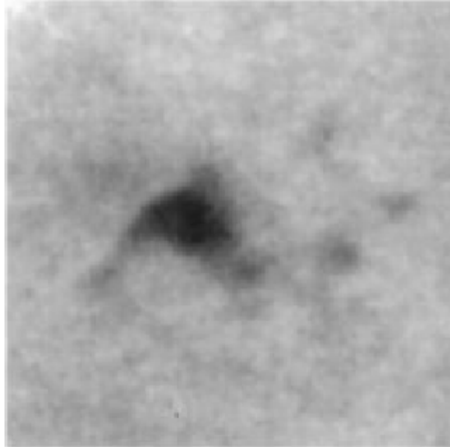

Figure 2.4: Image of amorphous zones resulting from an impact of a single 200 keV Xe ion. (Total micrograph width = 30 nm) From Ref. [Donnelly et al., 2003].

indicating that for high mass ions the damage morphology is governed by local melting in the cascade core, which upon resolidification results in local amorphous pockets. Recrystallization of the amorphous zones by annealing indicates that the recrystallization of the various amorphous pockets yields a range of activation energies, which increase with size.

Experimentally, in-situ TEM has shown individual amorphous zones in silicon resulting from impacts of 200 keV Xe at room temperature [Donnelly et al., 2003] (see Fig. 2.4). Recrystallization of these amorphous zones has been observed to occur both thermally [Donnelly et al., 2003], as well as by electron irradiation [Jenčič and Robertson, 1996]. The zones were observed to recrystallize over a wide range of temperature, from 70 °C to more than 400 °C, unlike the thermal recrystallization rate of planar amorphous-crystalline interface, which exhibits Arrhenius-type behavior with a single activation energy. Recent nanocalorimetry measurements [Karmouch et al., 2005] also suggest that "the annealing of a collection of highly disordered pockets is a good candidate to explain the continuous rate of heat release observed by nanocalorimetry."

Both theoretical and experimental studies have been done in order to estimate

the recrystallization activation energy of some amorphous pockets. An activation energy of 0.89 eV for a 1.2 nm radius amorphous pocket is obtained by MD [Marques et al., 2003], while an experimental work on the recrystallization behavior of larger, single isolated amorphous zones produced by Xe ions shows activation energies of about 1.2 eV. Although *ab initio* calculations and molecular dynamics have been used extensively for interstitial, vacancy clusters and extended defects because of the limited structural configurations and energies involved, they cannot simulate the annealing of an amorphous pocket for the temperature and time of practical interest, where an unlimited number of configurations and energies can be expected.

2.1.3 Extended Defects

The evolution of ion implantation induced damage in silicon can be very different during the subsequent annealing step depending on whether or not amorphization is reached. In cases where damage is not sufficient to amorphize the lattice, damage can evolve into extended defects, like the {311} defects, dislocation loops and voids [Holland and White, 1991], through the agglomeration of point defects. For dopant TED mediated by interstitials, the source of interstitials comes from a hierarchy of interstitial defects, from small precursor clusters with lower activation energy of dissolution, to {311} defects with intermediate activation energy of dissolution, and to large dislocation loops with high dissolution energy [Cowern et al., 1999b]. In order to model dopant TED, it is crucial to know the point defect binding energies to these extended defects. In addition, the geometry of extended defects like the {311} defects and the dislocation loops is important as the capture radius for interstitial point defects should reflect the shape of the defects [Cowern et al., 1999c, Kim et al., 2000].

With low dose silicon implants, TED is observed in the absence of visible {311} defects [Cowern et al., 1994]. The source of interstitials is likely to be from

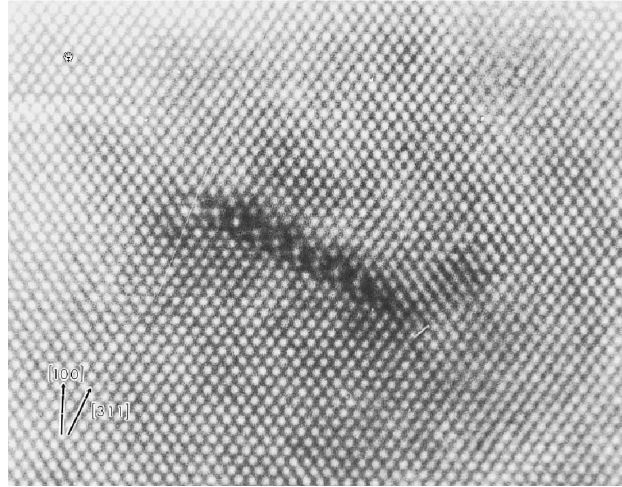

Figure 2.5: Cross-section high-resolution electron micrograph showing {311} defects. From Ref. [Eaglesham et al., 1994].

small precursor clusters that are not visible with transmission electron microscopy (TEM). These small interstitial clusters are shown to have multiple complex configurations from *ab initio* calculations [Richie et al., 2004]. Stabilities of these small interstitial clusters have also been obtained theoretically from calculations [Bongiorno et al., 2000, Chichkine et al., 2002] and experimentally from the inverse modeling of defect ripening [Cowern et al., 1999c]. It was found that the binding energies exhibit a non-monotonic behavior with cluster size.

Upon annealing, interstitial precursor clusters would undergo Ostwald ripening, with small, less stable interstitial clusters dissolving and the larger, more stable ones growing. Eventually, with higher dose silicon implants, {311} defects as shown in Fig. 2.5 are formed [Eaglesham et al., 1994]. When the {311} defects nucleate, they act as sinks for point defect interstitials, reducing the amount of TED [Cowern et al., 1994]. With longer annealing times, the {311} defects no longer acts as sinks, but as sources.

{311} defects are rod-like planar defects lying on the {311} plane, elongated in the <110> direction, with width in the <233> direction. The structure of the {311} defects has been characterized from high resolution transmission elec-

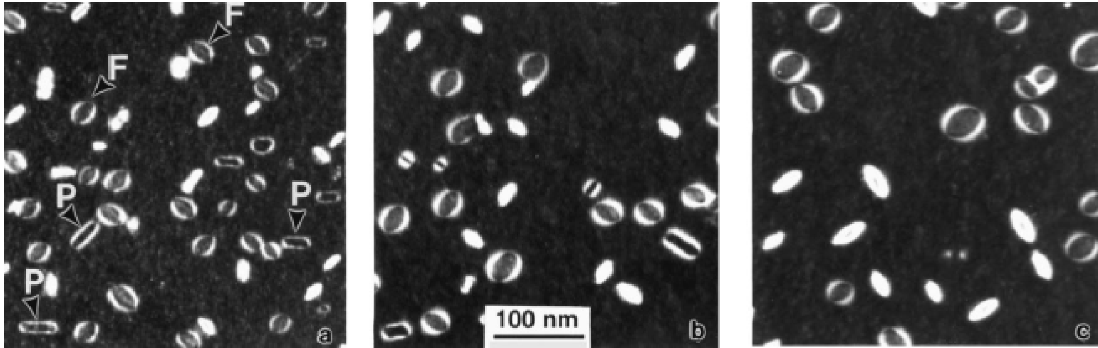

Figure 2.6: Transmission electron microscopy micrographs showing faulted and perfect dislocation loops. From Ref. [Cristiano et al., 2000].

tron microscopy (HRTEM) [Takeda, 1991]. The stability of the {311} defects are also better understood from theoretical calculations [Kohyama and Takeda, 1992, Kim et al., 1997].

If the dose is high enough and with sufficient annealing time, dislocation loops (see Fig. 2.6) may form by the unfaulting of {311} defects [Li and Jones, 1998]. TEM shows that dislocation loops can be faulted or perfect planar defects lying on the {111} planes [de Mauduit et al., 1994]. Faulted dislocation loops lie on {111} planes and have a Burgers vector **b** of $a/3 < 111 >$ perpendicular to the loop plane. There are 4 variants of this defect, which have a circular shape. The perfect dislocation loops are found to lie on {111} planes and have a Burgers vector a $(a/2) < 110 >$. They are elongated along that particular <110> direction on their habit plane, which is perpendicular to the Burgers vector. Therefore, 12 variants of this defect exist. The formation of dislocation loops lowers the interstitial supersaturation. This slows down TED as the dislocation loops grow at the expense of the remaining {311} defects. After all the {311} defects have evaporated, the dislocation loops then act as a source of interstitials driving TED [Bonafos et al., 1997, Bonafos et al., 1998].

The transformation of {311} defects into dislocation loops has been observed in silicon for both amorphizing [de Mauduit et al., 1994] and non-amorphizing im-

plants [Li and Jones, 1998]. For amorphizing implants, dislocation loops are often observed in the end-of-range region. In order to model the transformation of {311} defects to dislocation loops, it is important to have a good model for amorphization, to provide reliable information on number of interstials in the end-of-range [Castrillo et al., 2005].

The amorphization process is reviewed in the following section.

2.2 Experimental observations of ion-implantation induced damage accumulation

In this section, an overview of experimental findings on the dependence of ion-implantation parameters on damage accumulation is presented. The many and interdependent implantation parameters, like implant ion mass, dose, dose rate and wafer temperature all contribute to determine the type and the amount of damage produced [Elliman et al., 1988, Schultz et al., 1991, Goldberg et al., 1995]. The crystalline-amorphous phase transition is therefore critically dependent on the implantation parameters. In silicon, amorphization occurs under ion implantation when the free energy of the damaged crystalline phase is higher than that of the amorphous phase.

The implant dose (number of implanted ions per unit area) at which a buried, completely amorphous layer first appears is known as the threshold dose. The threshold dose required for light ions is much higher than that for heavy ions at the same temperature [Morehead et al., 1972]. This can be explained by the fact that for the same implant energy, a larger fraction of the incident energy is lost in nuclear collisions (as opposed to electronic losses) in the case of higher mass ions, thus causing more atomic displacement. Moreover, the morphology of the damage produced is different, which strongly affects the dynamic annealing and therefore the rate of damage accumulation [Caturla et al., 1996].

The threshold dose is a strong function of the implant temperature. For a constant dose rate (dose per unit time) implantation, increasing the dose is observed to bias the amorphous threshold condition towards higher temperatures [Morehead et al., 1972]. This implies that amorphization is hampered when silicon is implanted at elevated temperatures and becomes impossible above a critical temperature, which is found to increase with the increase of ion mass. Figure 2.7 shows the critical transition for Si ions from minimally defected crystalline material to a

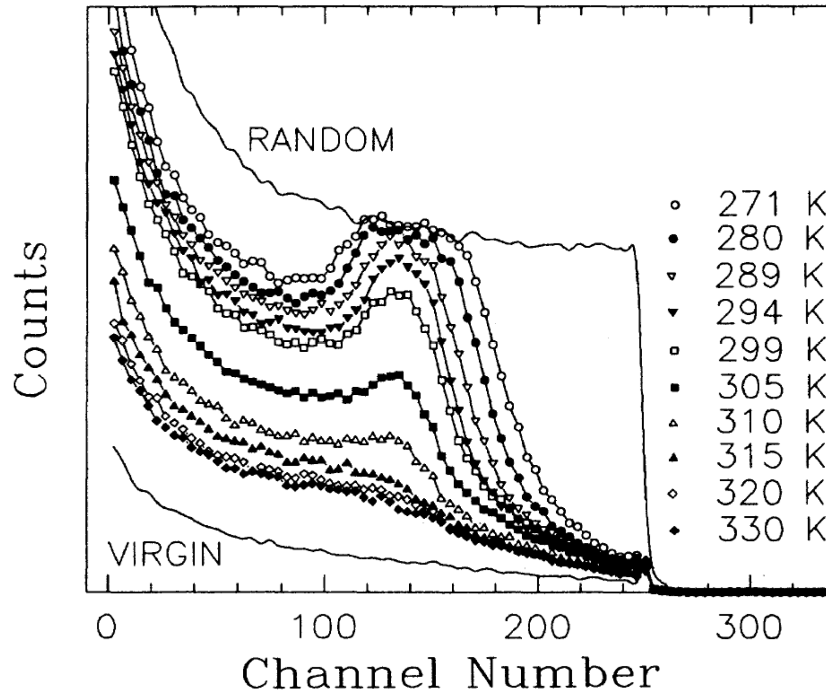

Figure 2.7: Channeling Rutherford backscattering spectra of the same silicon implant at different substrate temperatures. Ref. [Schultz et al., 1991].

continuous, buried amorphous layer around room temperature. The temperature dependence of ion implantation induced amorphization is considered to be due to the competition between damage accumulation and dynamic annealing. For low implant temperatures, most of the generated damage is retained and the damage rapidly increases with dose. At higher temperatures, damage is annealed dynamically, resulting in less damage accumulation.

Experimental evidence also shows a strong effect of different dose rates on damage accumulation. A fixed dose ion implantation of silicon at 450-550K is shown to produce either crystalline silicon with defects or amorphous silicon depending on the dose rate used [Elliman et al., 1988]. Damage increases with dose rate [Prussin and Zhang, 1996, Holland et al., 1985] and a critical dose rate exists above which an amorphous layer is formed. In addition, a pre-existing continuous amorphous silicon layer could be induced to crystallize epitaxially or grow in thickness

during ion implantation depending on the dose rate, temperature and the type of implant species [Linnros et al., 1988, Williams et al., 1985, Priolo et al., 1990b].

Comparison of Ar and Xe implantation data also illustrates the effect of dose rate on different ion species [Elliman et al., 1988]. The amorphous threshold dose rate is almost three orders of magnitude higher for Ar than for Xe, for constant dose implantations. This difference arises from the fact that Xe, being a heavier species (132 u) has four times the maximum nuclear stopping power than for Ar (40 u). However, a four fold increase in dose of Ar is insufficient to compensate for the difference in amorphous threshold dose rate. This suggests that the dynamical defect density within cascades and/or cascade size are also important parameters.

Competition between crystallization and amorphization, and thereby the nucleation of a buried amorphous layer, is controlled experimentally by interdependent factors, namely dose rate and temperature at a given implant condition. Generally, dose rate controls the production rate of defects and temperature controls the concurrent annealing rate. The combination of dose rate and substrate temperature shows that dynamic annealing and defect production can be balanced to control amorphization over a wide range of implant conditions. The critical amorphous-crystalline transition temperature increases with increase in dose rate for the same dose, thus balancing the decrease in the annealing time with the increase in temperature [Schultz et al., 1991, Goldberg et al., 1995]. However, as ion implantation proceeds, beam heating inevitably takes place [Holland et al., 1996]. Therefore, if it is not effectively avoided by thermally coupling the target wafer to a temperature-controlled holder, the dose rate effect can be reversed as the increase in dynamic annealing dominates over the actual dose rate effect. For silicon implants, the amorphous-crystalline critical transition occurs near room temperature [Schultz et al., 1991, Goldberg et al., 1995]. For this reason, beam heating effects could lead to contradictory results if experiments were done without consideration of the sensitivity of temperature (beam heating). Furthermore, in the temperature

range of the critical transition, the dynamic annealing time (determined by the dose rate) will have a significant influence on the resulting damage.

Various works have attempted to obtain the activation energy for damage anneal. Around room temperature, the activation energy was found to be 0.9 eV [Schultz et al., 1991] as opposed to the higher 1.2 eV at higher temperature (450-550 K) [Elliman et al., 1988]. The reported 0.9 eV is assumed to be an average value for various, complex defects. These results are consistent with the idea that amorphization is a result of dynamic evolution of the highly disordered regions, which are likely to have a continuous range of activation energies. At higher temperature, the low activation energy processes are very fast and the measured activation energy would reflect higher values. Furthermore, a series of apparent activation energies ranging from 0.7 to 1.7 eV were determined with ions ranging from C (12 u) to Xe (132 u) (see Fig. 2.8), by measuring the temperature at which an amorphous layer first appears as a function of the ion dose rate. At high dose rate, more damage is generated by ion implantation and in order to balance the rate of damage generation with the rate of dynamic annealing, the wafer substrate temperature at which the implantation is carried out has to be increased. For the same dose rate, heavier implant ion generates more damage, which also requires higher temperature to increase the rate of dynamic annealing to reach the crystalline-amorphous transition point. This again supports the idea of highly disordered regions having a continuous range of activation energies, as it is unlikely that these energy values corresponds to different discrete defects.

Another interesting feature of damage accumulation is the polyatomic effect. Polyatomic ions have been shown to cause more damage than the same atoms implanted separately [Davies et al., 1975, Matsuo et al., 1998]. Davies et al. reported that C_6^+ ions displaced more lattice atoms in room temperature implantation of silicon than the same atomic dose of C^+.

In addition, damage formation is affected by implanting chemically different

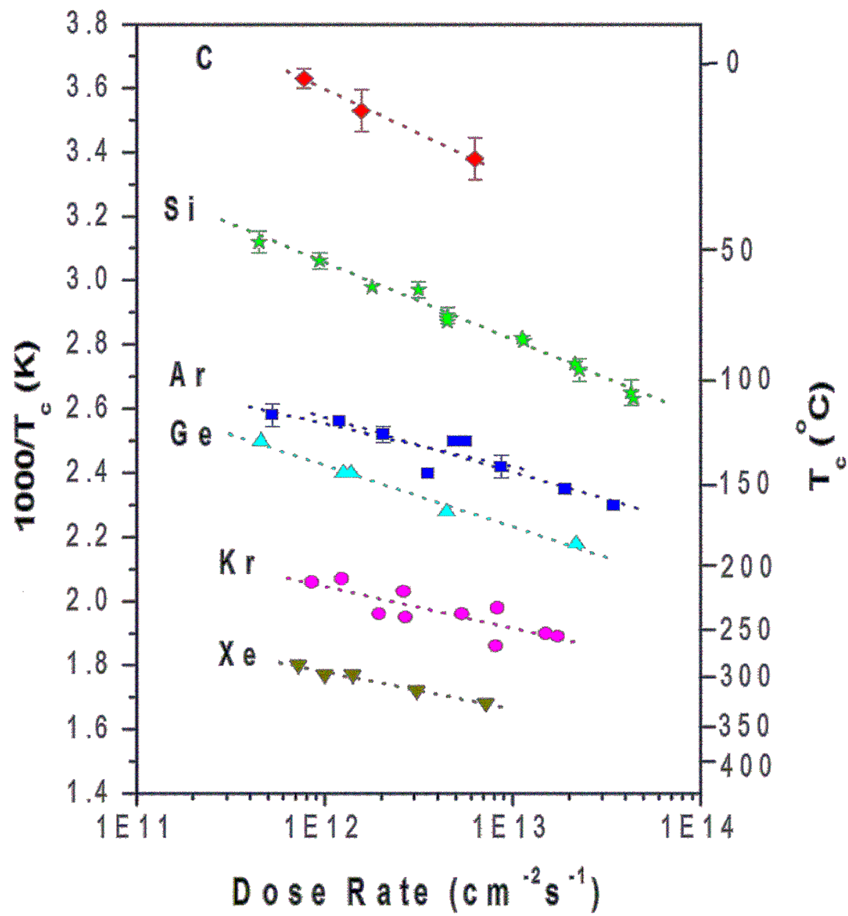

Figure 2.8: Experimental crystalline-amorphous transition temperatures for (100) Si implanted with 80 keV ions to a fluence of 1×10^{15} ions/cm^2 for Si, Ar, Ge, Kr and Xe ions. Data points for carbon are for irradiations to 2×10^{15} ions/cm^2. From Ref. [Goldberg et al., 1995].

species of similar ion masses. As the ions in comparison have similar masses, any difference in the induced damage can be attributed to ion-solid chemistry. For example, a higher dose of B compared to C is required to produce the same level of damage [Baranova et al., 1973]. In the case of Si and P, P has been observed to enhance the growth of damage induced by room temperature implantation [Motooka and Holland, 1992] . Furthermore, voids have been observed in high temperature P implanted samples, but not in Si implanted ones [Holland et al., 1996]. Similar results were obtained for Ge and As. Voids are thought to be formed from the excess vacancies produced during implantation. Their absence within the self-ion implanted Si suggests that chemical effects associated with the dopant plays an important role in their formation. Theoretical simulations [Oshiyama et al., 1995] have suggested that certain sizes of vacancy clusters in a diamond lattice would not be stable at elevated temperatures, making it difficult to "bridge" these sizes in a continuous growth. P and As may provide a stablilizing effect, enabling the formation of larger vacancy clusters.

2.3 Simulation techniques

To model the damage accumulation induced by ion implantation, taking into account the dynamic annealing effect, requires the simultaneous simulation of ion implantation and annealing. This section gives an overview of the different simulation techniques that could be used for the simulation of ion implantation induced damage.

2.3.1 Binary Collision Approximation

As an ion moves through a solid target, it transfers energy elastically by collisions with the target nuclei and loses energy inelastically by interaction with the surrounding electrons in the target material. The energy transferred to the electrons can lead to the excitation of the electrons to higher energy levels, or to the ejection of the electrons from their atomic orbitals (ionization). The energy loss by the moving ion to the target by nuclear and electronic interactions gradually slows the ion, eventually bringing it to a stop. It is practically impossible to experimentally study the displacement cascades generated along the path of an energetic ion due to their small size and very rapid dynamics. Computer simulation codes based on the binary collision approximation (BCA), such as MARLOWE [Robinson and Torrens, 1974] and TRIM [Ziegler et al., 1985] have traditionally been used to obtain the number and distribution of displaced atoms (or Frenkel pairs) along the track of the incoming ion. Depending on the code, the target material can be crystalline or amorphous. MARLOWE was developed to employ crystalline targets with all the atoms in well-defined initial positions, while TRIM was developed for amorphous targets.

BCA is considered a Monte Carlo method, which is a stochastic technique based on the use of random numbers and probability statistics. In the context of modeling ion implantation, location of the target atoms and collision parameters may

be randomly obtained. The basis of BCA is on the concept of a "displacement energy". Within this approximation, the collisions between recoils in the ion induced displacement cascade occur only between moving and stationary atoms. It calculates all collisions between ions or recoils and the silicon target atoms by assuming that the energetic atom interacts only with the closest atom in its neighborhood. A target atom is recoiled and thus permanently displaced from its lattice site, leaving a vacancy site, if the energy transferred to it in a collision exceeds a fixed value, the displacement energy. The number and spatial distribution of displaced atoms can thus be calculated by following each recoil with energy above the displacement energy. In this way, the entire collision cascade is obtained.

The basic assumption in modeling energy loss due to nuclear collision in BCA is that the ion will interact with only one target atom at a time. This simplification allows the use of the binary scattering theory from classical mechanics. Figure 2.9 shows the schematic drawing of two bodies in a center-of-mass (CM) system. The projectile (ion) has mass M_1 and initial velocity V_0. The target atom has mass M_2 and is initially at rest. The system velocity V_C is defined such that there is zero net momentum in the system. r_{min} is the minimum interatomic separation and the distance, p, is known as the impact parameter. Θ and Φ are the angles of scatter and recoil respectively.

The final angle of scatter, Θ, in terms of the CM coordinates, is given by

$$\Theta = 2\int_{r_{min}}^{\infty} \frac{pdr}{r^2\sqrt{1-\frac{V(r)}{E_c}-\frac{p^2}{r^2}}} \tag{2.1}$$

where E_c is the initial CM kinetic energy and V(r) is the potential at r, the interatomic separation. This equation is known as the general orbit equation for two-body central force scattering.

This equation can then be used to calculate the energy transferred in a collision from the incident projectile to the target, T_{atom}.

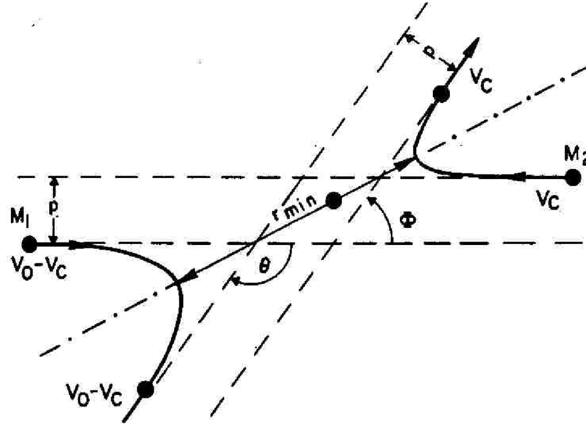

Figure 2.9: Schematic drawing of two-body scattering theory in center-of-mass (CM) coordinates.

$$T_{atom} = \frac{4E_oM_1M_2}{(M_1+M_2)^2} sin^2\frac{\Theta}{2} \tag{2.2}$$

where E_o is the initial ion kinetic energy.

The above equations show that the energy loss during a scattering event is not only a function of the initial kinetic energy and the masses of the two particles, but also the scattering angle Θ, which is in turn a function of the potential V(r).

Potentials may be considered as a Coulombic term (1/r) arising from the positive point nucleus, multiplied by a "screening" function due to the surrounding electron cloud. The screening function may be defined as the ratio of the actual atomic potential at some radius to the potential caused by an unscreened nucleus.

$$V(r) = \frac{Z_1Z_2e^2}{r}\phi(\frac{r}{a}) \tag{2.3}$$

where Z_1, Z_2 are the atomic numbers, ϕ is the screening function, r is the interatomic separation and a is the screening length.

A universal screening function obtained by fitting the screening functions of many pairs of atoms is given as

$$\phi(x) = 0.1818e^{-3.2x} + 0.5099e^{-0.9423x} + 0.2802e^{-0.4028x} + 0.02817e^{-0.2016x} \tag{2.4}$$

where x is the ratio of the interatomic separation, r and the universal screening length, a_u.

$$a_u = \frac{0.8854a_o}{Z_1^{0.23} + Z_2^{0.23}} \tag{2.5}$$

where a_o is the Bohr radius.

In addition to nuclear energy loss, electron energy loss also occurs when an ion interacts with the electrons of the target atoms. This mechanism is inelastic and does not alter the direction of the ion's trajectory, only its energy. Electron energy loss can be approximated to be proportional to the square root of the ion energy, E_{ion}:

$$S_E = k_e\sqrt{E_{ion}} \tag{2.6}$$

where k_e is a constant that depends on the ion and target atomic masses and numbers.

The classical Lindhard-Scharff formula [Lindhard and Schaff, 1961] assumes that energy loss is proportional to ion velocity and is useful for incident ions that are heavier than the target atoms.

$$k_e = \frac{1.212Z_1^{7/6}Z_2}{(Z_1^{2/3} + Z_2^{2/3})^{3/2}M_1^{1/2}} \tag{2.7}$$

For light incident ions, the semi-empirical Oen-Robinson formula may be employed [Oen and Robinson, 1976].

$$k_e = \frac{0.045K}{\pi a^2}exp(\frac{-0.3r_{min}}{a}) \tag{2.8}$$

where K is a parameter, r_{min} is the minimum distance between the particles and a is the screening length in the Moliere potential.

Although the BCA technique is very efficient, it becomes insufficiently accurate at very low energies. Firstly, BCA assumes that the potential energy of the ion at the start of the collision is negligible compared to its kinetic energy. Thus, BCA can be expected to fail when the kinetic energy of the ion becomes comparable to

the interatomic potential energy of the ion and target atom, at a distance corresponding to the nearest neighbor separation. Secondly, BCA neglects multi-body interactions, which become important when the interatomic potentials of not only the nearest target, but also more distant ones, are not negligible compared to the potential energy. Within such approximation, only collisions with energies higher than 200 eV can be accurately treated [Caturla et al., 1996].

References [Robinson and Torrens, 1974, Ziegler et al., 1985, Robinson, 1989] provide further details regarding the BCA technique.

In terms of practical applications, BCA models provide spatial distribution of the collision cascades only in terms of point defects, and therefore they are not capable of representing the type of damage (e.g. clusters or amorphous pockets) generated. Furthermore, BCA codes on their own can only treat ballistic processes during ion bombardment, but they are not capable of simulating the quenching of the collision cascades, let alone the thermally activated dynamic annealing that takes place throughout the duration of the ion implantation. Some phenomenological models for damage accumulation have been developed using the BCA technique, taking into account dose rate and temperature effects [Posselt et al., 2001].

2.3.2 Molecular Dynamics

Deterministic MD simulation technique on the other hand, provides a more precise way to study the initial development of the displacement cascade, as it treats the full dynamics of the collision process [Diaz de la Rubia and Gilmer, 1995], including the ballistic collision and the thermal spike phase. MD simulations can also provide physical insight into amorphization process at the atomic level. This technique is based on the integration of the classical equations of motion of an ensemble of atoms in a crystallite [Allen and Tildesley, 1987]. Because atom trajectories are computed from forces derived from the gradient of an interatomic potential and integrated using Newton's equations, the simulation can describe the complete phase

space available to the system. Therefore, MD can help predict the formation of realistic damage microstructures not accessible to BCA-based calculations.

MD techniques simulate the behavior of every lattice atom and use a very small constant timestep to be able to resolve the lattice vibrations well, which have a period of about 0.1 ps. Hence, although the time scale reached by this technique (nanoseconds) can be used to treat the full dynamics of the collision process, it is not appropriate for the thermally activated processes following the quenching process, whose total duration equals the implantation time. Therefore, while MD is a useful technique to provide insights into the fundamental physics of the collision process in the silicon lattice, it is so computationally intensive that it is limited not only in terms of time scale, but also in the number of atoms it can simulate. Hence, the use of MD for the simulation of device processing is prohibitive.

2.3.3 Continuum Approach

Traditionally, the processes associated with the evolution of point defects and dopants were modeled almost entirely by the continuum approach, based on coupled partial differential equations (PDE). In continuum simulation, the physics is formulated as a series of differential equations for each particle type. Typically, these equations are continuity equations, where particle gain or loss depends on recombination and diffusion fluxes. Simple first-order chemical reactions are used to describe the interaction between dopants and defects, as well as between point defects and clusters.

This technique is not limited by the size of the simulations and can typically achieve the time scale required for standard silicon IC processing conditions. At the industrial level, SUPREM [SYNOPSYS, 2005b] and FLOOPS [SYNOPSYS, 2005a] are the most commonly used programs based on this technique. However, due to the complexity of deep-submicron device processing technology, the number of different configurations of defects and dopants that need to be accounted for is rather

large and a separate balanced equation needs to be solved for each of these species. This requires a significant amount of computational resources to be able to model complex interacting phenomena. Furthermore, the continuum approach does not account for spatial correlations between defects, thus it has neither the ability to directly model discrete dopants, nor the size and/or shape dependence of defects, like the amorphous pockets.

2.3.4 Kinetic Monte Carlo

As mentioned, the Monte Carlo method is a stochastic technique that makes use of random numbers. The essence of kMC is that real time scale can be calculated with this technique, therefore it is suitable for the simulation of activated processes.

If one considers any type of defects in silicon, almost all the possible processes they can undergo are activated processes, that is, they occur only when the internal energy exceeds a certain (activation) energy barrier, E_{act}. See schematic in Fig. 2.10. Typically, the barrier can be overcome by thermal activation. In the classical limit, the probability, P, of exceeding the energy barrier follows a Boltzmann's distribution:

$$P \propto exp(-\frac{E_{act}}{kT}) \tag{2.9}$$

where k is the Boltzmann's constant and T is the temperature.

Therefore, the rate of a given process, or the probability per unit time for a given event, can be written as

$$Rate(T) = \omega_o exp(-\frac{E_{act}}{kT}) \tag{2.10}$$

where ω_o is the prefactor. In the limit where $E_{act} \rightarrow 0$ or T$\rightarrow \infty$, the probability of the event would be ω_o.

Central to kMC is an algorithm that sequentially selects the possible random events according to their respective rates. At the intial time, t=0, the rates, r_i, of all the possible events that can occur in the system are calculated. Consider a specific

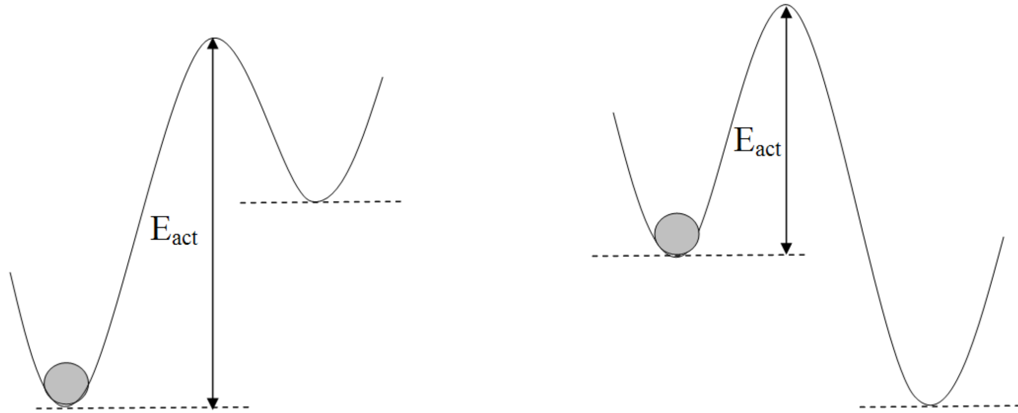

Figure 2.10: Schematic showing the energy barrier in a process that leads to a (a) higher-energy state and (b) lower-energy state.

example of a system in silicon, which consists of 3 vacancies, 2 interstitials and 1 {311} defect. For simplicity, assume that the interstitial jump rate is calculated to be $1000\,\mathrm{s}^{-1}$, the vacancy jump rate to be $100\,s^{-1}$ and the {311} emission rate to be $10\,\mathrm{s}^{-1}$.

Following that, a cumulative function R_N is obtained as the summation of the rates of all possible events.

$$R_N = \sum_{j=1}^{i} r_j \tag{2.11}$$

for i = 1 ,..., N, where N is the total number of possible events. To execute the kMC process, all events with high or low probabilities should have a chance to be selected.

To select an event, a random number is generated between 0 and R_N. Suppose that the random number generated selects an "I jump" event, as shown in Fig. 2.11, another random number is then generated to select which one of the 2 interstitials actually jumps, and the event is carried out. In this way, different events will be selected with probabilities corresponding to their rates. After the event is carried out, the system is updated as it may have been changed due to the occurence of the previous event. The simulation of an event increases the time by $1/R_N$. This

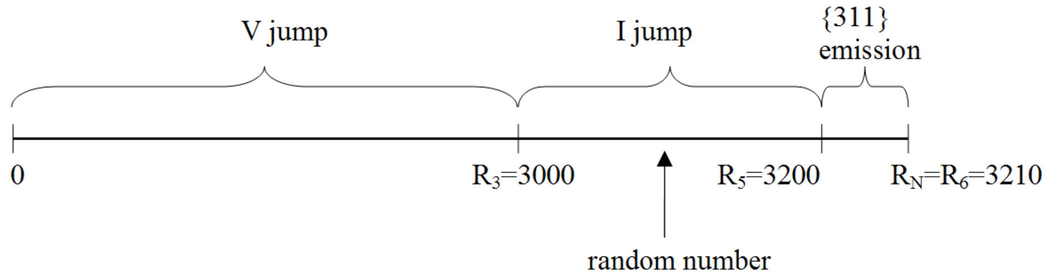

Figure 2.11: Schematic showing the kMC algorithm that selects random events according to their corresponding rates.

process is then repeated until the specified time is reached.

Since R_N calculated at each step depends on the objects present and the possible events that can occur, the time step in kMC follow the system evolution automatically. If initially for instance, the system consists of a set of very high-rate events, which after some time have reacted and disappeared from the system leaving behind the slow-rate ones, the time step will automatically increase. It is due to this feature that kMC can model systems where the initial time scale may be of the order of picoseconds and the final one may be of the order of minutes or more.

Therefore, kinetic Monte Carlo (kMC) can be a useful tool to simulate up to the macroscopic space and time scales involved in standard silicon IC processing conditions. This is especially the case with the scaling down of device dimensions coupled with the increase in computational power. Such atomistic simulations are critical as device features shrink and individual atomic positions become important to the electrical behavior.

While the MD method relies on the accuracy of the interatomic potential used, the kMC method requires a list of all defect types and all possible events together with their energetics. The parameters used in kMC simulations can be derived from *ab initio* calculations, classical MD and experimental data. In MD, all lattice

and defect atoms are simulated, while in kMC, only defect atoms are considered. Therefore, kMC can handle larger simulation sizes and longer simulation times, since the high frequency vibrational movement of the silicon lattice atoms is ignored and the simulation accounts for relevant events of much lower frequencies. As such, kMC is an event-driven technique, which simulates events at random, with probabilities according to their respective event rates. In this way, it self-adjusts the time-step as the simulation proceeds, just to be able to account for the fastest event present at the current time. Therefore, the kMC technique can handle actual device processing time and length scales, and yet include atomic level detail.

In order to simulate the full ion implantation process, including dynamic annealing, it would be necessary to couple MD or BCA that generates the collision cascades, with kMC to simulate the thermal (dynamic) annealing between the cascades. Several studies on damage evolution have been done using the kMC technique [Jaraiz et al., 1996, Bedrossian et al., 1997]. Jaraiz el al. used BCA simulations to provide the three-dimensional representation of the location of the defects induced by the implantation process as inputs to the kMC simulations, while Bedrossian et al. used MD simulations for the same purpose.

2.4 Existing models of damage accumulation

As ion implantation into crystalline silicon proceeds, damage like point defects, defect clusters or amorphous pockets, can accumulate up to a certain level until the highly-damaged crystalline silicon becomes unstable and crystalline to amorphous phase transition occurs. Over the years, numerous works have been done to investigate damage accumulation and several models have been proposed to account for the experimental observations. These models might be divided into two major categories postulating either the homogeneous or the heterogeneous amorphization mechanisms. In this section, some representative models that account for damage accumulation and the various techniques where dynamic annealing is taken into account in the earlier works will be briefly reviewed.

2.4.1 Homogeneous Amorphization Mechanism

Some experiments indicate that the damage produced in the collision cascades consists mostly of point defects and small defect clusters that suggest a homogeneous amorphization mechanism. According to the homogeneous amorphization model, ion implantation increases the defect density to a level where the damaged crystal becomes unstable and spontaneously transforms to amorphous silicon. Frenkel pairs created within different collision cascades are assumed to be sufficiently long-lived such that they can outdiffuse from the cascade volume and interact with similar defects from other cascades throughout the implanted region to form uniformly distributed stable defect structures, resulting in amorphous damage nucleation and growth.

Traditionally, amorphization was modeled in a simplistic manner. It was assumed that the lattice turned amorphous if a critical point defect density was exceeded [Christel et al., 1981, Cerva and Hobler, 1992]. The critical point defect density can be obtained from measured depths of amorphous layers. The compar-

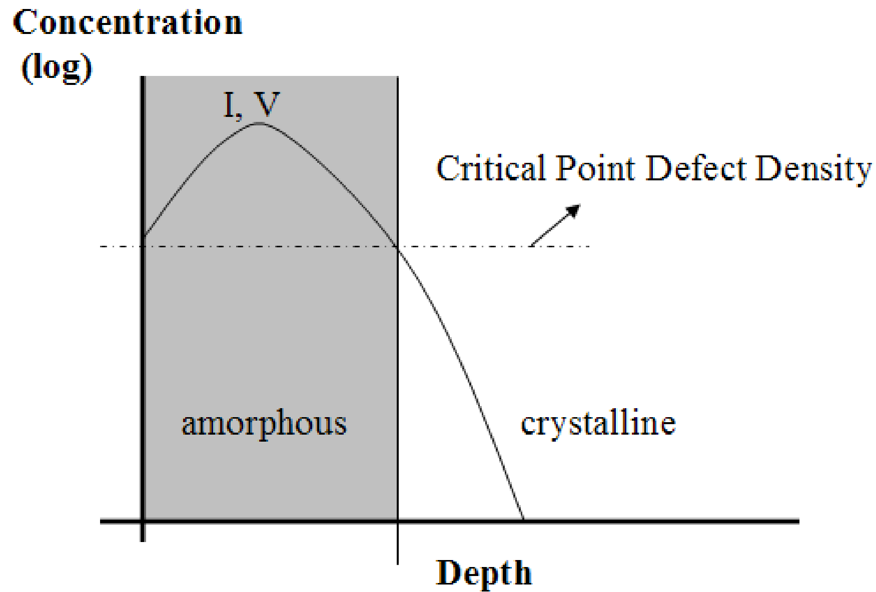

Figure 2.12: Critical point defect density determined from the position of the amorphous-crystalline interface and simulated BCA point defect profiles.

ison of the position of the amorphous-crystalline interface of an amorphous layer observed in TEM images with the damage estimated from BCA simulations, indicates that amorphization occurs when the initial defect concentration exceeds a certain threshold level. Schematic of this method is shown in Fig. 2.12. One of the main limitations of this simplistic model is the uncertainty in the critical point defect density value. Due to the shape of the defect distribution, a small change in the position of the amorphous-crystalline interface leads to a large variation in defect concentration. Hence, although this simple model allows reasonable prediction of the amorphous layer thickness, values for the threshold density used in literature range between 5 % and 50 % of the atomic density of silicon ($5 \times 10^{22}\,\mathrm{cm}^{-3}$) depending on implant parameters (see Fig. 2.13, Ref. [Hobler and Otto, 2003] and references therein). Furthermore, as mentioned, the same implant condition without taking care of the wafer temperature could lead to contradictory results.

Analogous to the critical point defect density model is the critical energy model.

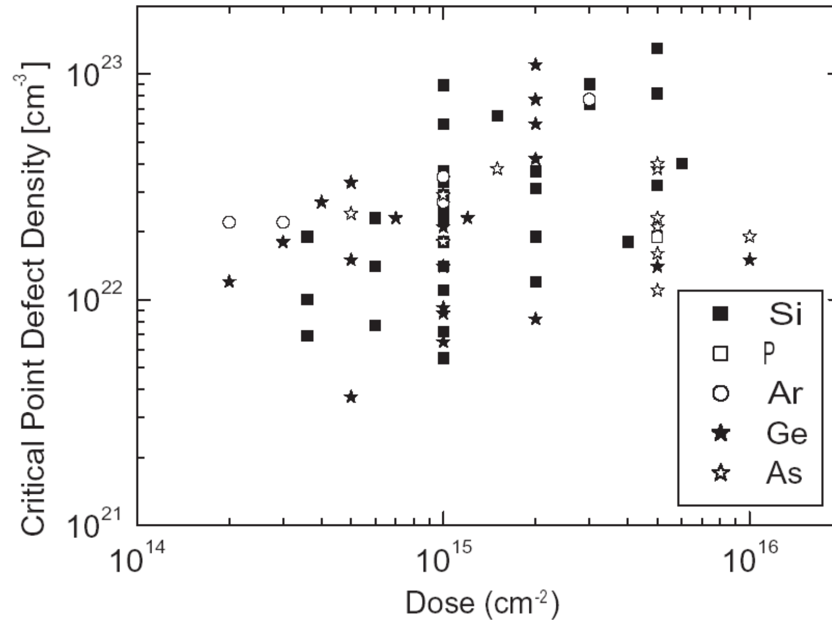

Figure 2.13: Critical point defect density (CPDD) extracted from the measured depths of amorphous layers and BCA simulations. Figure from Ref. [Hobler and Otto, 2003].

This model holds that it is the nuclear-stopping portion of the energy deposited by the implanted ions in their collisions with the lattice atoms, that leads to atomic displacements in the lattice. Therefore, when the deposited energy is high enough, the lattice energy increases above a critical value such that it becomes energetically favorable for the defective lattice to convert to the amorphous state. Amorphization can thus be modeled by a critical energy deposition per unit volume [Dennis and Hale, 1976, Vieu et al., 1989].

Holland et al. used the homogeneous damage model to explain experimental observation of the superlinear growth of damage accumulation with dose (see Fig. 2.14) [Holland et al., 1989] and the two-layered damage distribution observed along the path of a high-energy (MeV) ion (see Fig. 2.15) [Holland and White, 1991].

The initial regime where damage accumulates slowly with a sublinear dependence on dose (Fig. 2.14) and the near surface low level damage saturation by high energy (MeV) ion (Fig. 2.15) were explained by the dynamic balance between

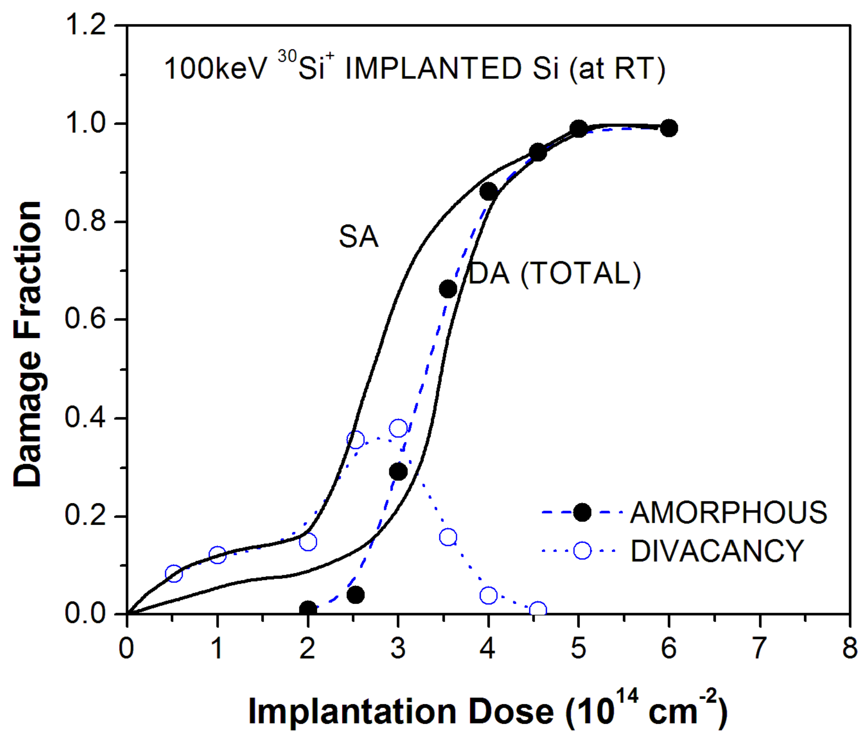

Figure 2.14: Dose dependence of damage produced by 100 keV Si^{+} ions in Si (100) single crystal at room temperature. Damage curves corresponding to both single alignment (SA) and double alignment (DA) Rutherford Backscattering Spectra (RBS) measurements, as well as the different damage components determined from the annealing results. From Ref. [Holland et al., 1989].

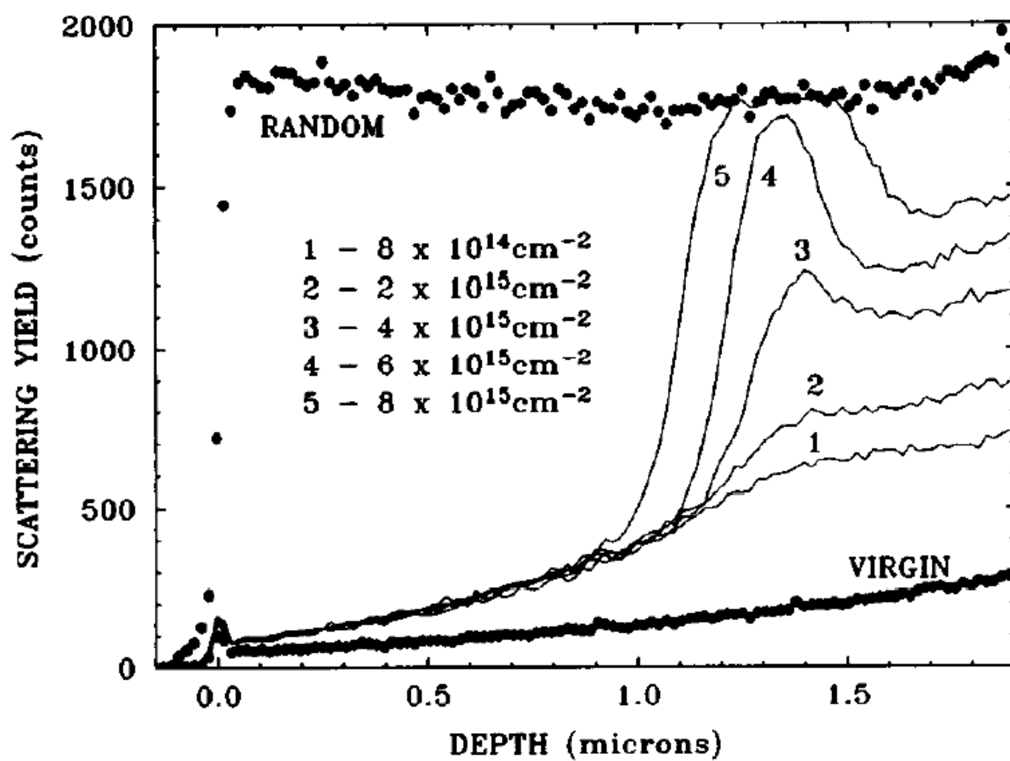

Figure 2.15: <100> aligned spectra from Si(100) samples implanted at various doses with 1.25 MeV self-ions. From Ref. [Holland and White, 1991].

the various defect reactions, in the absence of point defect sinks. Chemical rate equations were used to express the simple defect reactions, which include I-V recombination, defect clustering (to form V_2 and I_2) and cluster dissociation through point defect capture. In the two cases mentioned, the rapid unconstrained damage growth was explained by the imbalance in the reactions, due to additional atoms during implantation and the spatial separation of the Frenkel pairs. As a result, amorphous silicon nucleates where the V_2 population exceeds the critical threshold for amorphization.

2.4.2 Heterogeneous Amorphization Mechanism

On the other hand, experimental observations that indicate the presence of amorphous zones in the cascade tracks suggest a heterogeneous amorphization mechanism [Howe and Rainville, 1981]. Such mechanism assumes that locally amorphous zones are generated heterogeneously by the incident ions within the collision cascades. As the ion-implantation dose increases, these zones accumulate and overlap to form a continuous layer [Morehead and Crowder, 1970].

Gibbons [Gibbons, 1972] derived the number of overlapping cascades required for the production of a certain area of amorphous zones. Light ions produce smaller cascades and require a larger number of overlaps, while heavy ions require a lower number of overlaps, with Sn requiring no overlap at all, as amorphization can result from ion impact directly [Wang et al., 1985].

Some authors propose using both the homogeneous and heterogeneous models simultaneously [Dennis and Hale, 1978]. The homogeneous model is more consistent with light implant ions, which produce fairly well-distributed point defects, while the heterogeneous model is more consistent with heavy ions, which produce amorphous zones directly.

2.4.3 Dynamic Annealing

The two types of models reviewed earlier do not account for dynamic annealing that takes place during ion implantation, as the rate of damage generation is not a relevant parameter. Some earlier works have attempted to model the effect of defect recombination and self-annealing. Using a modified BCA code, MARLOWE [Robinson and Torrens, 1974], Klein et al. [Klein et al., 1991] and Jaraiz et al. [Jaraiz et al., 1993] account for the partial recombination of I and V by annihilating them if they are located within a specified capture radius of one another. As the fraction of damage which is dynamically annealed at implant temperature can strongly affect the impurity profile in channeling implants, Klein et al. made use of implanted boron profile to determine the I-V recombination distance. On the other hand, Jaraiz et al. determined the recombination distance by directly fitting the calculated damage profile to experimentally measured ones obtained from channeling Rutherford Backscattering Spectrometry (RBS).

Hernandez-Mangas et al. [Hernandez-Mangas et al., 2005] using the BCA technique as well, developed a statistical damage buildup model based on a modified Kinchin-Pease model [Hernandez-Mangas et al., 2002] that takes into account dose rate and temperature effects, accounting for amorphous-crystalline transition temperatures. In this model, the net increase in point defects as the projectile travels along its trajectory is given as a function of the defect survival ratio, which depends on temperature and dose rate. Making use of the concept that the activation energy of recombination for a given defect is dependent on its surrounding defects [Marques et al., 2003, Pelaz et al., 2003], the defect density in this model is related to the number of IV pairs surrounding a given IV pair, to account for the thermal dependence of the model.

Based on theoretical calculations and experimental observations, Pelaz et al. [Pelaz et al., 2003] implemented an atomistic amorphization and recrystallization

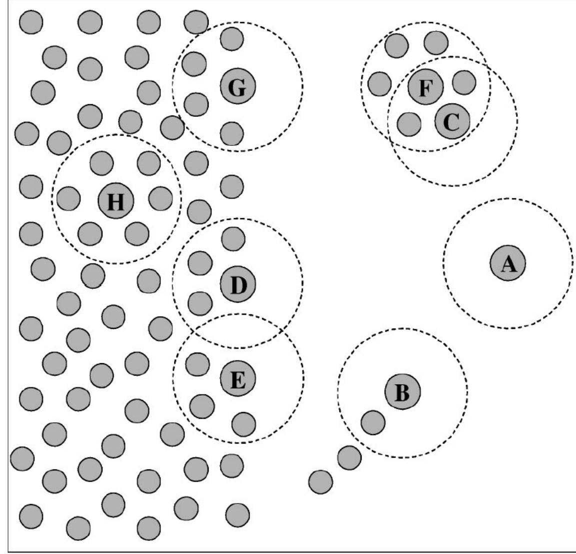

Figure 2.16: Scheme of damage topology. Each gray circle represents an IV pair and the dashed lines their interaction radius. Isolated IV pairs (A) annihilate first as they do not have any IV neighbor. The amorphous pockets start recombining by the outer IV pairs (B and C) as the inner ones (F or H) have more IV neighbors. When an IV pair in a planar structure recombines, the whole layer regrows as the surrounding defects (D or E) have less IV neighbors than the other defects in the layer (G). From Ref. [Pelaz et al., 2003].

model in a non-lattice kinetic Monte Carlo (kMC) simulator [Jaraiz et al., 1998] that reproduces the amorphous-crystalline transition temperatures for Si and Ge. In the model, silicon I and V generated in each implantation cascade interact to form the metastable bond defect or IV pair, instead of recombining instantaneously. Each IV pair is characterized locally by the number of neighboring IV pairs. An activation energy of 0.43 eV [Marques et al., 2001] was assigned to isolated IV pairs. Activation energy of 2.4 eV [Csepregi et al., 1978], the recrystallization energy of a planar crystal-amorphous interface, is used to characterize the recrystallization rate of IV pairs with about half of the total coordination number. IV pairs embedded in an amorphous matrix have an activation energy of 5 eV [Masaki et al., 1993]. Intermediate coordination number has interpolated energies.

In Fig. 2.16, each gray circle represents an IV pair and the dashed lines their

interaction radius. Isolated IV pairs (A) annihilate first as they do not have any IV neighbor. The amorphous pockets start recombining by the outer IV pairs (B and C) as the inner ones (F or H) have more IV neighbors. When an IV pair in a planar structure recombines, the whole layer regrows as the surrounding defects (D or E) have less IV neighbors than the other defects in the layer (G). The transition temperatures for Si and Ge obtained from this model agrees well with experiments.

2.5 Conclusion

Current front-end process models based on various simulation techniques are limited in modeling ion implantation induced damage accumulation. Traditionally, models for damage accumulation can be divided into either the homogeneous or the heterogeneous amorphization mechanisms. Under the homogeneous model, amorphization was considered to be the result of the accumulation of simple defects. This is more consistent with light implant ions, which produce fairly well-distributed point defects. Under the heterogeneous model, it is the overlap of locally amorphous regions that result in amorphization. This, on the other hand, is more consistent with heavy ions, which produce amorphous zones directly.

In addition to modeling amorphization, an additional challenge is to properly account for dynamic annealing. Although some phenomenological [Posselt et al., 2001] and statistical [Hernandez-Mangas et al., 2002] models have been used to account for the dose rate and temperature effects, physical modeling is limited. An atomistic kMC model based on the metastable bond defect, known as the IV pair, has been used to account for dynamic annealing [Pelaz et al., 2003].

In this thesis, a damage accumulation model that unifies both homogeneous and heterogeneous descriptions of amorphization will be described. Hence it is able to account for crystalline to amorphous phase transition for both light and heavy ions. Central to this model are defect structures known as the amorphous pockets, which have been extensively studied theoretically [Caturla et al., 1996] and observed experimentally [Jenčič and Robertson, 1996, Donnelly et al., 2003].

The model that is presented in this thesis is able to accurately simulate a range of interesting experimental observations. Moreover, it is computationally efficient in time and length scale, and can be used at the industrial level for technology computer-aided design (TCAD) in device-sized process simulations.

Chapter 3

Model Description

In this chapter, the model implemented for damage accumulation to simulate the damage evolution from point defects to continuous amorphous layer, taking into account dynamic annealing during the implant process, is described. Firstly, a brief summary is given of the simulation technique. Secondly, damage structures known as the amorphous pockets, which are central to this model, will be illustrated. Following that, the amorphization and recrystallization model will be explained. Lastly, the model parameters will be presented.

3.1 Simulation Technique

In order to achieve the aim of modeling damage accumulation taking into account dynamic annealing, it is necessary to couple a damage formation (ion implantation) simulation technique to an annealing one.

For annealing, atomistic kMC technique is able to model spatial correlations between defects, unlike the continuum technique. This is essential as it accounts for the ion mass effect on damage accumulation. For ion implantation, simulation techniques include BCA and MD. MD is computationally intensive and thereby limited in terms of time scale and in the number of atoms it can simulate. Even if the expected increase in process speed is taken into account, the MD/kMC coupled approach does not seem realistic in the foreseeable future for use in technology computer-aided design (TCAD) [Hobler and Otto, 2003]. Therefore, the most viable option is to use the BCA/kMC coupled simulation technique.

The software that is used in this work is known as DADOS [Jaraiz et al., 2001], which uses a BCA/kMC coupled technique. It incorporates an implant function that uses MARLOWE [Robinson and Torrens, 1974, Arias et al., 1995] to generate the coordinates of the interstitials and the vacancies for each cascade.

DADOS is a non-lattice, atomistic kMC simulator, which simulates only the defect atoms and is capable of modeling the spatial distributions of the defects. It is non-lattice as the processes and dimensions to be simulated are insensitive to using a lattice. Moreover, the computer requirements would be prohibitive for practical situations. Lattice kMC is needed for instance, to simulate grain boundary diffusion in polycrystalline materials [Rubio et al., 2003]. DADOS is capable of handling complex interacting phenomena typical in device processing [Jaraiz et al., 2001, Martin-Bragado, 2005]. For example, it can simulate diffusion of point defects and mobile dopants [Pelaz et al., 1997], Fermi level effects [Martin-Bragado et al., 2005a, Martin-Bragado et al., 2005b], clustering and dissolution of like point defects [Cowern et al., 1999c, Martin-Bragado et al., 2003], clustering of point defects with dopants [Pelaz et al., 1997, Pinacho et al., 2002, Pinacho et al., 2005], recombination, dissolution of clusters, recombination and generation of point defects at surfaces, interface trapping [Rubio et al., 2005] and recrystallization of amorphous regions.

Simulations in DADOS are carried out in three-dimensional space, where x is the depth of the silicon wafer and yz is the implantation area. The total simulation volume is divided into a maximum of 2^{19} boxes, whereby each axis is divided into 2^m sections, so that $m_x + m_y + m_z \leq 19$.

The smallest possible dimension of each box is 0.768 nm, which is also twice the second neighbor distance. For instance, if the x, y and z axes of the total simulation cell is required to be 1000 nm × 15 nm × 15 nm, the x axis would be divided by 2^{10} into 1024 boxes, while the y and z axes would be divided by 2^4 into 16 boxes, so that each small box, known as a BitBox, would be 0.977 nm ×

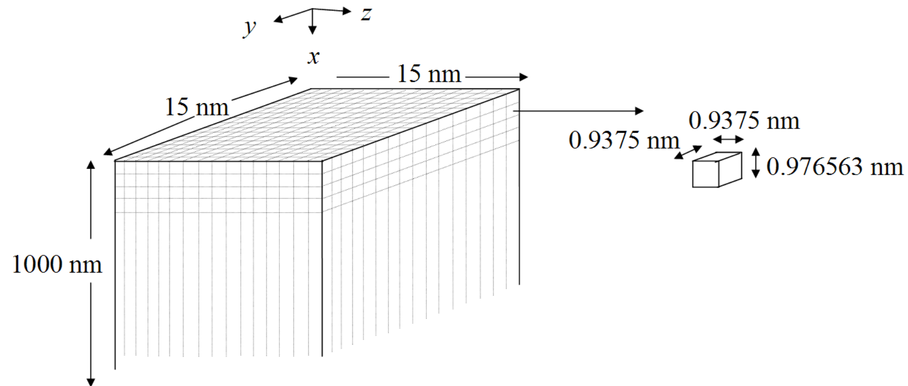

Figure 3.1: Schematic showing the division of three-dimensional space in DADOS into small BitBoxes.

0.938 nm × 0.938 nm. The schematic showing the division of three-dimensional space in DADOS into small BitBoxes is shown in Fig. 3.1. The concentration of particles in each BitBox can then be calculated from the number of particles bounded within, divided by the volume of the BitBox.

In this model, the ion implantation induced Frenkel pairs (displacement cascades) are generated by the BCA code, MARLOWE [Robinson and Torrens, 1974]. The coordinates of this damage are then fed into DADOS (kMC) simulator, which simulates defect reactions, such as diffusion, clustering, recombination for the amount of time determined by the dose rate. This accounts for the dynamic annealing during the implantation process. The damage generated by the subsequent ions is then accumulated over the previous damage with near-neighbor interaction being taken into account. The cycle is repeated for each cascade, until all of the ions are implanted for a given dose.

Point defect diffusion is simulated by point defect jumps over a fixed distance, λ based on the diffusivity. λ is set to the second neighbor distance, 0.384 nm. The diffusivity is calculated according to the diffusivity prefactor, D_{mo} and migration energy, E_m, as shown in Table 3.1. DADOS modifies the particle coordinates only

in orthogonal directions, randomly allowing jumps in six different directions (±x, ±y, ±z).

$$D_m = D_{mo} \exp \frac{-E_{\mathrm{m}}}{kT}. \tag{3.1}$$

Table 3.1: Parameter values for interstitials and vacancies diffusion.

Parameter	Value
D_{mo}(I)	$5 \times 10^{-2}\,\mathrm{cm^2 s^{-1}}$
E_m(I)	$0.8\,\mathrm{eV}$
D_{mo}(V)	$1 \times 10^{-3}\,\mathrm{cm^2 s^{-1}}$
E_m(V)	$0.4\,\mathrm{eV}$

In addition, a thin native oxide layer is assumed in the simulations. The silicon-silicon oxide interface is modeled as a perfect sink for point defects [Lim et al., 1995, Cowern et al., 1999a]. Therefore, all point defects within the capture distance (second neighbor distance, 0.384 nm) will be trapped at the surface.

3.2 Amorphous pockets

3.2.1 Structure

The damage model is based on the damage structures known as amorphous pockets (AP, [Caturla et al., 1996]). Instead of undergoing immediate recrystallization, interstitials (I) and vacancies (V) are assumed to form a distinct, disordered region (AP), preventing their diffusion, when they are within a capture distance (second neighbor distance, 0.384 nm) of each other. An AP is, therefore, a three-dimensional, irregularly-shaped agglomerate of I's and V's surrounded by crystalline silicon, Fig. 3.2. The I and V terms are used as a means of referring (for an I_nV_m AP) to a disordered region of a size roughly equal to n+m with a net excess or deficit of atoms n-m. These damage structures are in direct correspondence to the APs studied by molecular dynamics (MD) [Caturla et al., 1996, Nordlund et al., 1998], produced from single cascades in Si. Note that an amorphous pocket is not an amorphous region, which will be defined later. When damage generated by subsequent ions accumulates over the previous damage, APs are merged taking into account near-neighbor interaction.

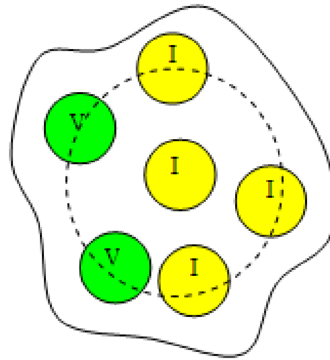

Figure 3.2: Amorphous pockets are irregularly-shaped agglomerates of interstitials and vacancies, formed when the point defects are within an interaction radius of each other. Dashed line represents the interaction radius.

3.2.2 Rate of Amorphous Pocket Recrystallization

Recrystallization of the APs by annealing in MD studies indicates that larger pockets have greater stability against recrystallization, as evidenced by their larger effective activation energies. In this work, the AP recrystallization rate (shrinkage rate) is characterized by the effective size of the AP, s. In this model, an AP of size s is assumed to shrink by recombining an I-V pair at a rate given by

$$Rate = \alpha s^{\beta} \exp \frac{-E_{\mathrm{act}}(s)}{kT}. \quad (3.2)$$

The effective size of the AP, s, can be defined as the number of IV pairs, or s=min(I,V). α and β are parameters of the amorphous pockets recystallization rate. k is the Boltzmann constant and T is the temperature.

A key challenge in modeling is that of experimental validation. This challenge is especially difficult because for most processes, there are many physical effects that can interact with each other. The different effects must be appropriately separated by well-selected experiments, in order to develop predictive models and not simply fit particular experimental data.

Table 3.2: Parameter values of amorphous pocket defect recrystallization.

Parameter	Value
α	$3 \times 10^{-4}\,\mathrm{cm^2 s^{-1}}$
β	1.0

Experimental data from Ref. [Goldberg et al., 1995] was used to determine the model parameters in this work. The experimental data corresponds to the amorphous-crystalline transition temperatures, as a function of dose rate, for (100) Si implanted with 80 keV ions to a dose of $1 \times 10^{15}\,\mathrm{cm^{-2}}$ for Si, Ar, Ge, Kr and Xe, and $2 \times 10^{15}\,\mathrm{cm^{-2}}$ for C (see Fig. 2.8). In the experiments, the amorphous-crystalline transition temperature is the temperature at which an amorphous layer

first appeared. Both in the experiment and in the simulations, the transition temperatures were determined as the maximum temperature that resulted in a buried continuous amorphous layer. The single set of parameters used is $\alpha = 3 \times 10^{-4}\,\mathrm{cm}^2\mathrm{s}^{-1}$, $\beta = 1.0$ and recrystallization activation energy as a function of size, as shown in Fig. 3.3. The maximum recrystallization activation energy is taken to be 2.7 eV, which is equal to that of a planar amorphous-crystalline interface of a fully amorphized region [Jackson, 1988]. Tabulated in Table 3.3 are the characteristic experimental activation energies for each ion extracted from Ref. [Goldberg et al., 1995].

The activation energy for recrystallization is assumed to be a function of s alone, irrespective of the internal spatial configuration (the *apparent* activation energy in Ref. [Caturla et al., 1996]). The APs can shrink (dynamic annealing) by recombining I and V if the temperature is high enough, or grow by incorporating extra I's or V's as implantation proceeds. Figure 3.4 shows APs formed in the simulation, resulting from an implanted cascade. Cascades shown are analogous to the cascades produced by the more detailed MD simulation shown in Fig. 2.3. Detailed analysis of APs size histogram would be discussed in the next chapter.

3.2.3 Amorphous Pockets and Clusters

Pure interstitials (I_nV_0) and vacancy clusters (I_0V_m) are considered to be subsets of the APs, with their own characteristic emission rates [Cowern et al., 1999c, Bongiorno et al., 1998]. Once an AP with a net excess of I's or V's has completely recrystallized, the remaining I's or V's become pure clusters. Similarly, during subsequent implant, pure clusters can transform back into an I_nV_m AP and have a chance of recrystallizing if a defect of an opposite type is within its capture radius. This allows for a self-consistent treatment of pure clusters and APs (I_nV_m). Schematic is shown in Fig. 3.5.

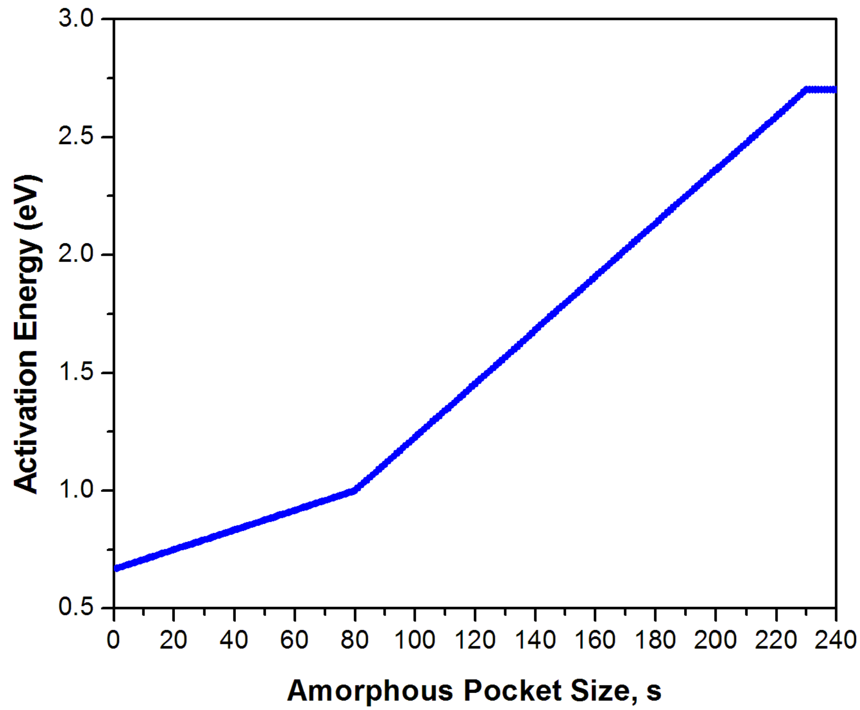

Figure 3.3: Activation energy of recrystallization as a function of size of the amorphous pockets.

Table 3.3: Experimental activation energies for 80 keV implantation of silicon with various ions. From Ref. [Goldberg et al., 1995].

Ion Species	Ion Mass (u)	Activation Energy (eV) ±0.15
C	12	0.75
Si	28	0.79
Ar	40	0.99
Ge	74	1.11
Kr	84	1.26
Xe	132	1.69

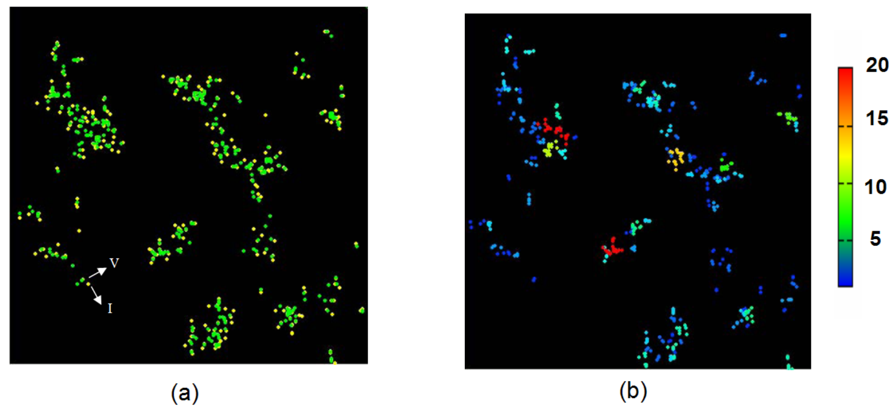

Figure 3.4: Amorphous pockets formed in simulation. (a) In terms of I (yellow) and V(green) (b) In terms of the number of IV pairs.

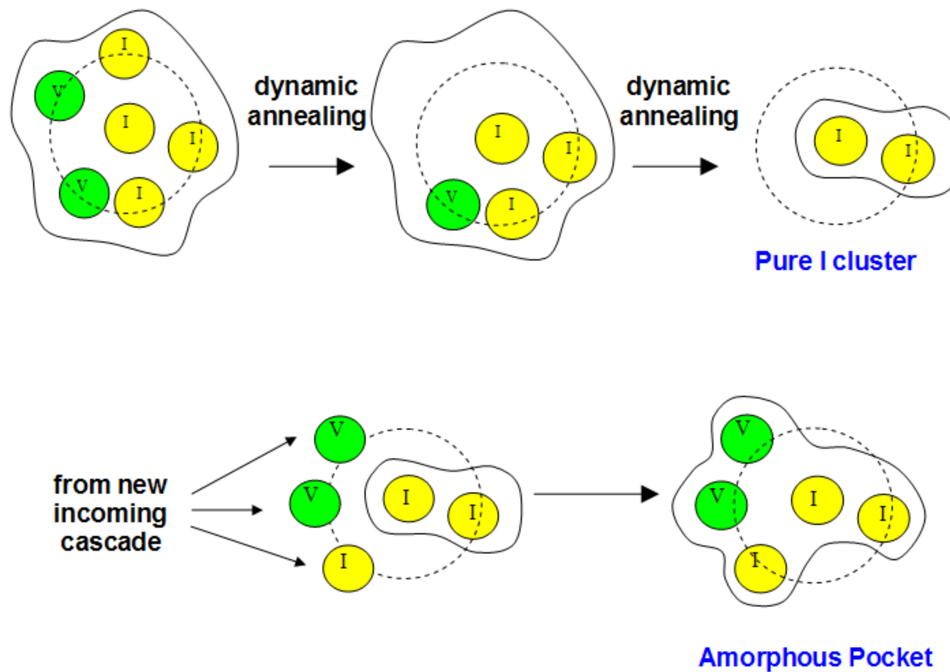

Figure 3.5: Schematic showing the consistent treatment of APs and clusters. Once an AP is completely recrystallized, remaining I or V behave as pure clusters (point defect capture/emission). Pure cluster can transform back into AP by capturing defect of the opposite type within its capture radius.

3.3 Amorphization

Amorphization is a massive form of lattice disorder. When ions are implanted into crystalline silicon above a certain critical dose depending on the implant condition, crystalline to amorphous phase transition spontaneously occurs. At this critical dose, a buried amorphous zone is first formed in the vicinity of the projected range of the implanted ions. The width of the amorphous zone subsequently increases with increasing dose.

As mentioned, literature values of amorphization threshold vary widely (see Fig. 2.13). One of the main tasks in modeling amorphization is to establish the amorphization threshold. In this model, the accumulation of APs plus point defects is assumed to give rise to locally, fully amorphized regions where the defect concentration (I+V) reaches the amorphization threshold. Due to dynamic annealing, the critical minimum dose for amorphization is a strong function of implant temperature. For a given ion, the critical amorphization dose increases with implant temperature. Hence, the amorphization threshold used in the model has to be determined from low temperature (100 K) implantation experiments [Morehead et al., 1972], whereby dynamic annealing can be assumed to be negligible.

Based on experiments, the critical amorphization dose required to produce a continuous amorphous layer for 200 keV B, P and 300 keV Sb implanted at 100 K and a dose rate of $1.25 \times 10^{12}\,\mathrm{cm^{-2}s^{-1}}$ is $1 \times 10^{15}\,\mathrm{cm^{-2}}$, $2 \times 10^{14}\,\mathrm{cm^{-2}}$ and $3 \times 10^{13}\,\mathrm{cm^{-2}}$ respectively. The critical dose for amorphization for all 3 ions can be accurately simulated using an amorphization threshold of $1.5 \times 10^{22}\,\mathrm{cm^{-3}}$.

Due to the division of the total simulation volume into BitBoxes, each Bitbox is rendered amorphous when its damage concentration reaches the amorphization threshold. If one considers a BitBox that is $0.977\,\mathrm{nm} \times 0.938\,\mathrm{nm} \times 0.938\,\mathrm{nm}$, then it would be rendered amorphous if it contains 12 particles.

Figure 3.6 shows simulation results with BitBoxes of the above-mentioned dimensions. Figure 3.6(a) shows a continuous, buried amorphous layer due to 200 keV B implanted at 100 K and a dose rate of $1.25 \times 10^{12}\,\mathrm{cm}^{-2}\mathrm{s}^{-1}$, up to the critical dose of $1 \times 10^{15}\,\mathrm{cm}^{-2}$, while Fig. 3.6(b) shows highly-damaged but still non-amorphized silicon substrate resulting from implantation up to half the critical dose. Notice that the same amorphization threshold is able to reproduce the critical amorphization doses for implant ions of different masses, from light B to heavy Sb ions.

As a test of the influence of a different BitBox size, Figure 3.7 shows simulation results for the same implant condition as in Fig. 3.6, with BitBoxes that are $0.977\,\mathrm{nm} \times 1.875\,\mathrm{nm} \times 1.875\,\mathrm{nm}$ in dimension. This would require 51 particles for a BitBox to be rendered amorphous.

Details on damage smoothing will be described later.

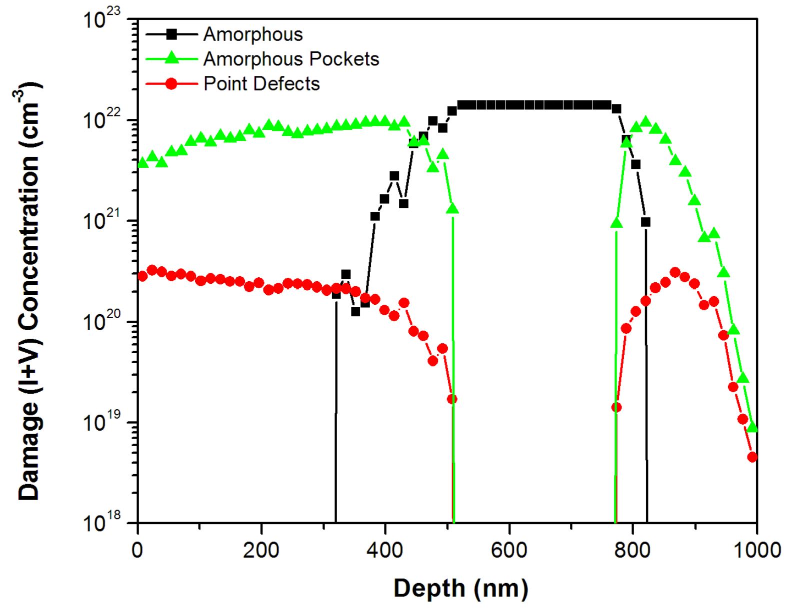

(a)

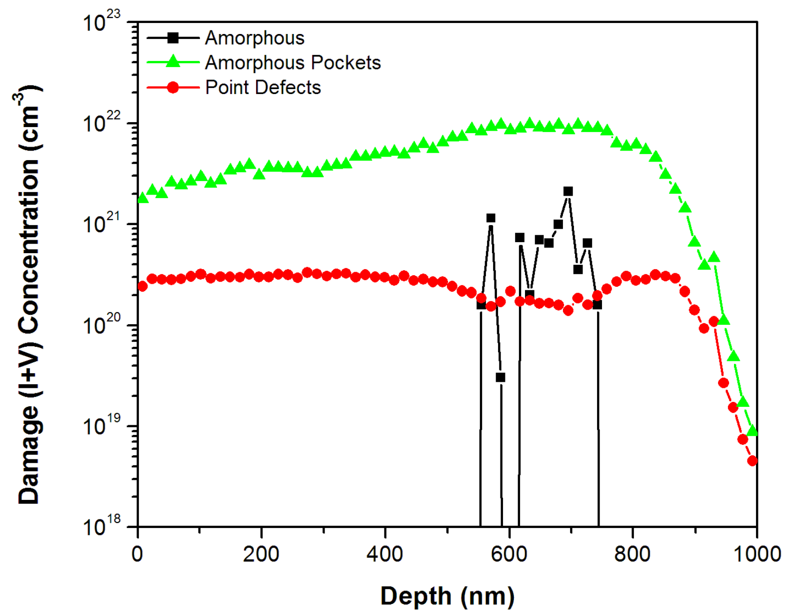

(b)

Figure 3.6: Simulated damage (total I+V) profiles for 200 keV B implant at 100 K and a dose rate of $1.25 \times 10^{12}\,\text{cm}^{-2}\text{s}^{-1}$. (a) Up to the critical dose of $1 \times 10^{15}\,\text{cm}^{-2}$. (b) Up to a dose of $5 \times 10^{14}\,\text{cm}^{-2}$. Dimension of BitBox: 0.977 nm $\times$ 0.938 nm $\times$ 0.938 nm.

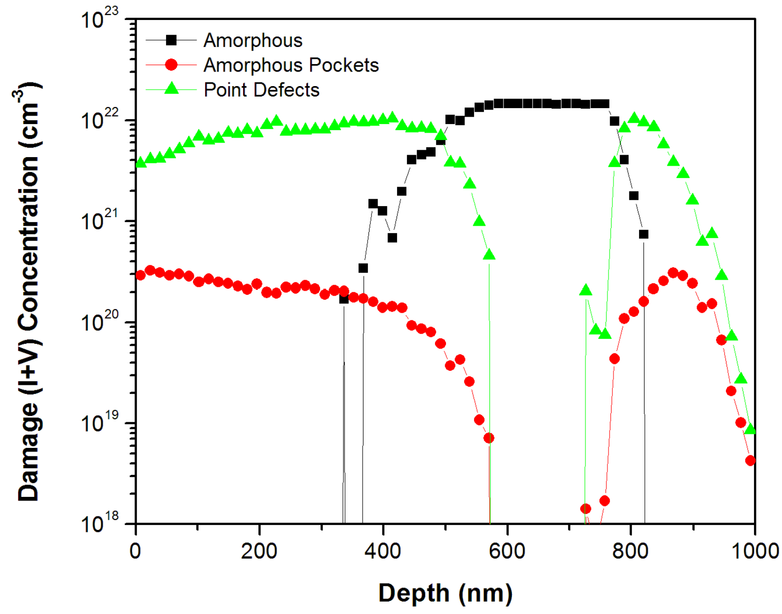

(a)

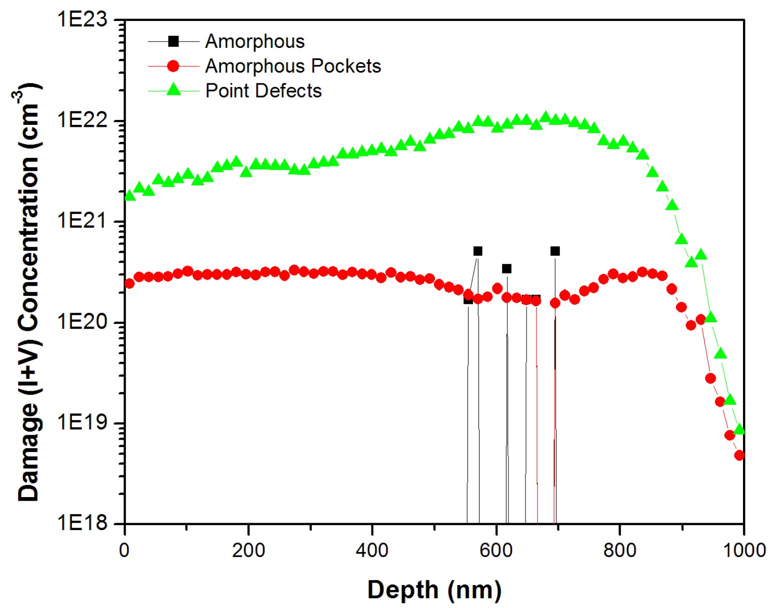

(b)

Figure 3.7: Simulated damage (total I+V) profiles for 200 keV B implant at 100 K and a dose rate of $1.25 \times 10^{12}\,\mathrm{cm}^{-2}\mathrm{s}^{-1}$. (a) Up to the critical dose of $1 \times 10^{15}\,\mathrm{cm}^{-2}$. (b) Up to a dose of $5 \times 10^{14}\,\mathrm{cm}^{-2}$. Dimension of BitBox: 0.977 nm × 1.875 nm × 1.875 nm.

3.4 Recrystallization

In cases where the implant dose is sufficient to amorphize the silicon lattice, the amorphous layer reorder at a much lower temperature (≈500 °C) than that required for the annealing of damaged crystalline regions. Annealing at temperatures above 500 °C induces a phase transition from amorphous into crystalline phase [Csepregi et al., 1975]. Under typical processing conditions, amorphous silicon layers on crystalline substrates recrystallize epitaxially by means of a planar motion of the amorphous-crystalline interface, which sweeps quickly across the amorphized region, leaving behind an almost perfect silicon lattice with impurity atoms but with essentially no interstitial or vacancy defects. This process is commonly known as the solid-phase epitaxial regrowth (SPER).

Thermal recrystallization of amorphous regions in contact with crystalline regions follows an Arrhenius law within a temperature range of 450 to 1360 °C [Roorda and Sinke, 1989]. At a given temperature, the amorphous-crystalline interface advances into the amorphous region at a certain recrystallization speed, v. The recrystallization velocity is calculated as

$$\nu_{recrys} = V_{0,recrys} \exp \frac{-E_{\mathrm{recrys}}}{kT}. \quad (3.3)$$

Table 3.4: Parameter values for the recrystallization of an amorphous-crystalline plane.

Parameter	Value
$V_{0,recrys}$	1.7×10^{8} cm/s
E_{recrys}	2.7 eV

Figure 3.8 and 3.9 shows a transistor source and gate time evolution during a 600 °C anneal following an amorphizing implant (Fig. 3.8) and a non-amorphizing implant (Fig. 3.9). The amorphizing implant in Fig. 3.8 is a typical Ge preamorphization implant at 20 keV and 1×10^{15} cm^{-2}. Simulation was done at room

temperature and at a dose rate of $1\times10^{13}\,\mathrm{cm^{-2}s^{-1}}$. During annealing, recrystallization takes place from the amorphous-crystalline interface. Excess defects contained within the amorphous layer are swept along with the amorphous-crystalline interface towards the surface, which acts as a sink for the defects, leaving the regrown layer free of defects. In the case of a buried amorphous layer, excess defects contained within the buried amorphous layer are swept along by the two simultaneously advancing amorphous-crystalline interfaces. In the absence of a sink, the excess defects are deposited as a plane of defects where the two interfaces meet. Hence, a buried amorphous layer is usually undesirable for practical applications. In any case, defects beyond the amorphous layer would evolve into more complex defect structures, like {311} defects and dislocation loops at higher annealing temperatures, forming a band of defects beyond the amorphous layer.

Figure 3.9 represents a non-amorphizing Ge implant at 20 keV and $5\times10^{13}\,\mathrm{cm^{-2}}$, also simulated at room temperature and at a dose rate of $1\times10^{13}\,\mathrm{cm^{-2}s^{-1}}$. Annealing at 600 °C is not enough to anneal the damaged crystalline regions. At the end of the anneal, defects are distributed throughout the implanted region, unlike the band of defects resulting from recrystallization of an amorphous layer.

An interesting result of the kinetics of SPER is the strong dependence on the impurity content. Some dopants, such as B, P and As, enhance the regrowth rate [Csepregi et al., 1977, Hamilton et al., 2005]. Other impurities, such as O, F and noble gases, retard the regrowth rate [Kennedy et al., 1977, Wittmer et al., 1978, Tsai and Streetman, 1979].

The recrystallization process also affects the impurity concentration. From the time evolution of As and In doping profiles during and after SPER, significant profile distribution towards the surface were found to occur due to the sweep of the dopants by the regrowing interface [Venezia et al., 2003]. Furthermore, detailed studies of dopant activation level revealed an “electrical” solid solubility limit, which was much lower than the total dopant concentration detected by SIMS

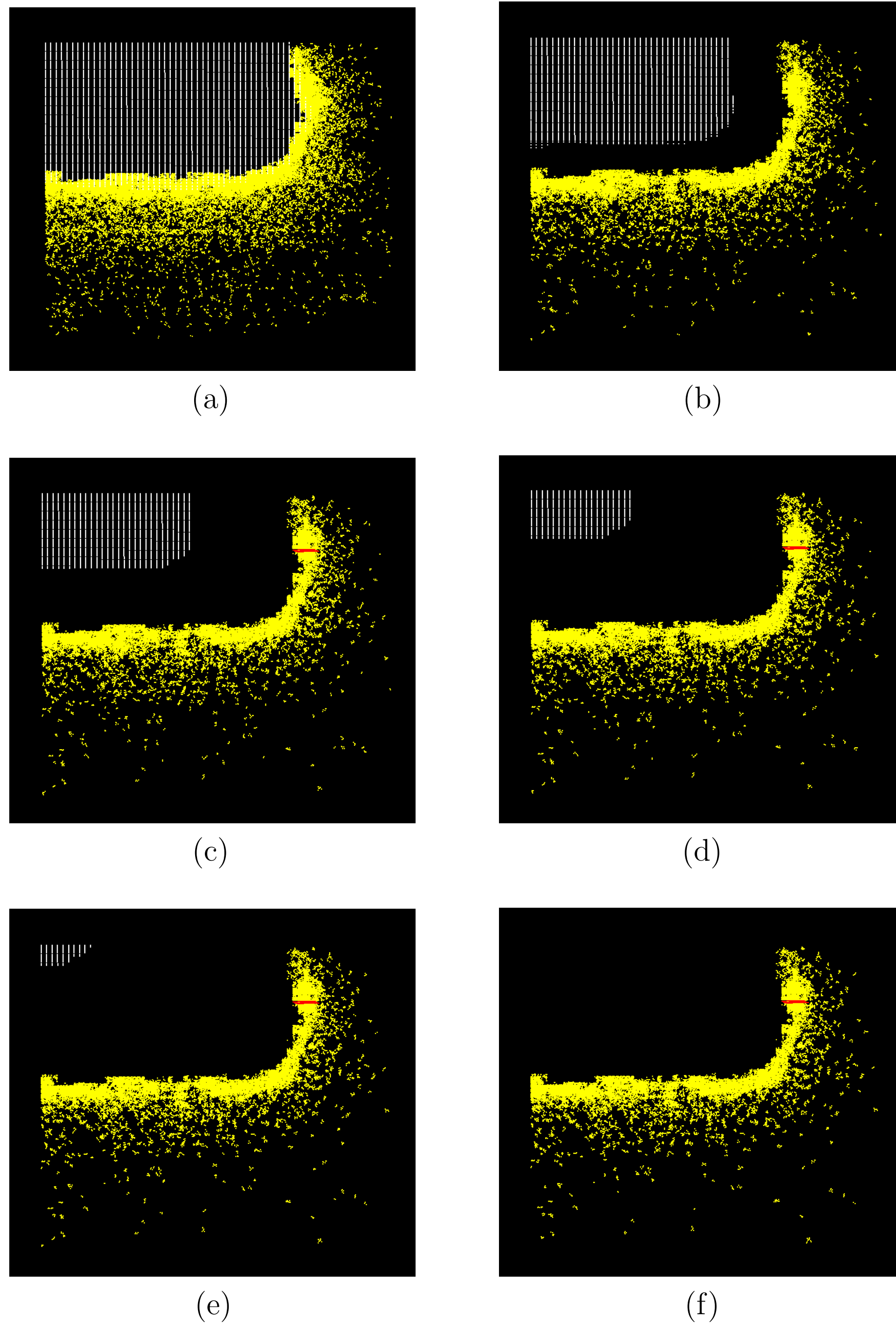

Figure 3.8: Source and gate time evolution of a transistor during a 600 °C anneal, following a typical Ge pre-amorphization implant at 20 keV, 1×10^{15} cm^{-2} (RT and a dose rate of 1×10^{13} cm^{-2}s^{-1}). Snapshots show annealing at (a) t=0 s, (b) t=20 s, (c) t=40 s, (d) t=60 s, (e) t=80 s and (f) t=100 s. White represents amorphous damage, yellow represents amorphous pockets and red represents {311} defects.

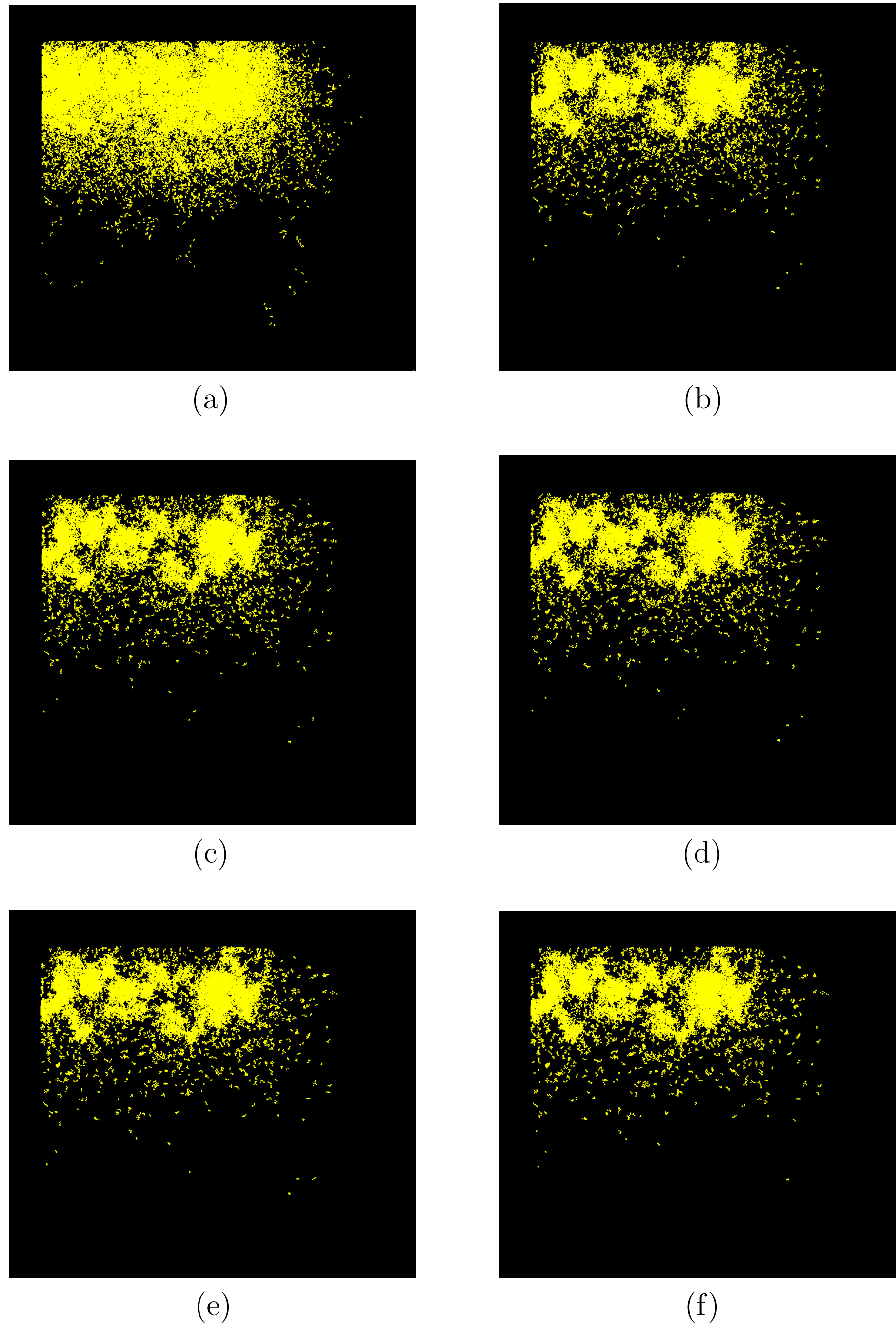

Figure 3.9: Source and gate time evolution of a transistor during a 600 °C anneal, following a non-amorphizing Ge implant at 20 keV, 5×10^{13} cm^{-2} (RT and a dose rate of 1×10^{13} cm^{-2}s^{-1}). Snapshots show annealing at (a) t=0 s, (b) t=20 s, (c) t=40 s, (d) t=60 s, (e) t=80 s and (f) t=100 s. Yellow represents amorphous pockets.

[Cristiano et al., 2004]. To simulate this, dopants are deposited as active up to a maximum concentration, while the rest are deposited as impurity clusters.

3.4.1 Damage Smoothing

In the simulations, it is necessary to avoid the presence of small non-amorphized regions in what ought to be a continuous amorphous layer. If small non-amorphized regions were present, recrystallization would start from the amorphous-crystalline interface during the subsequent annealing, leading to excess defects being deposited in the amorphous layer, as in the case of a buried amorphous layer.

However, due to the artificial discretization of space into BitBoxes in the simulator, the probability of one small discrete BitBox not containing sufficient interstitials or vacancies to reach the amorphization threshold concentration, is significant.

Therefore, there is an additional "LatticeCollapse" parameter that tries to avoid this. When a non-amorphous region of size less than or equal to this parameter is completely surrounded by amorphous material, then this non-amorphous region would be converted into amorphous as well.

Tests done have shown that a "LatticeCollapse" of $40\,\mathrm{nm}^3$ is sufficient in the simulations. Figures 3.6 and 3.7 were obtained with this value. Figure 3.10 shows simulation results of the same condition, whereby there is no damage smoothing ("LatticeCollapse" $= 0\,\mathrm{nm}^3$). In Fig. 3.10, where there ought to be a buried amorphous layer, a few BitBoxes have clearly not reached the amorphization threshold concentration due to the random nature of the collision cascades. Therefore a complete amorphous layer is not formed, even though the amount of defects in the amorphous region is almost an order of magnitude in concentration above that of the other defects.

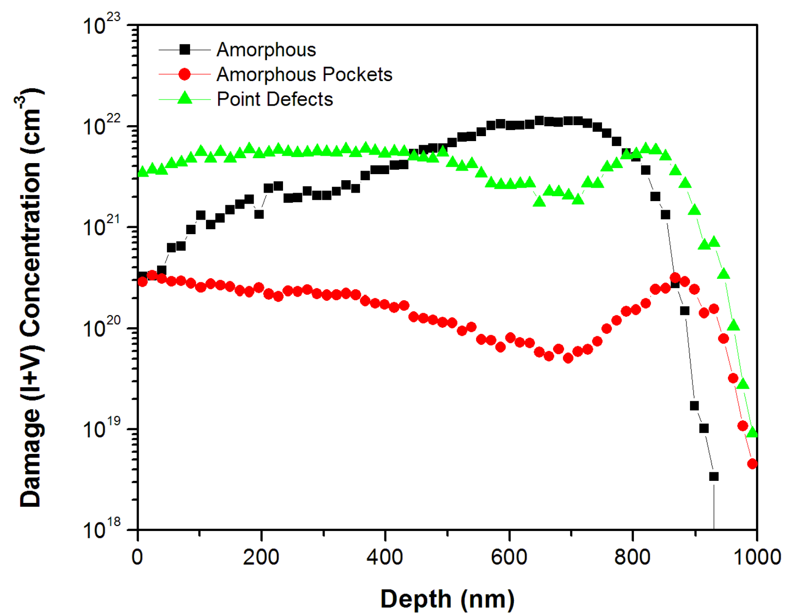

Figure 3.10: Simulated damage (total I+V) profiles for 200 keV B implant at 100 K and a dose rate of $1.25 \times 10^{12}\,\mathrm{cm}^{-2}\mathrm{s}^{-1}$ without damage smoothing, up to the critical dose of $1 \times 10^{15}\,\mathrm{cm}^{-2}$. Dimension of BitBox: $0.977\,\mathrm{nm} \times 0.938\,\mathrm{nm} \times 0.938\,\mathrm{nm}$.

Chapter 4

Effect of Defect Spatial Correlation

Before presenting simulation results of a variety of experimental observations, this chapter first provides a better understanding of the amorphous pocket (AP) model by comparing the initial damage morphology generated by ions of different masses, showing that different AP size distributions are produced with different ion masses. This chapter then addresses the importance of the spatial correlation of interstitials (I) and vacancies (V) in modeling damage accumulation and amorphization, by comparing simulations whereby the initial coordinates of I and V are generated by BCA or randomly generated from the concentration distribution of an input damage profile. In order to compare the initial damage morphology, implantations were simulated at low temperature to avoid dynamic annealing. For the same damage level, simulations by BCA resulted in ion mass dependent APs' sizes, with lighter implant ions generating smaller APs' sizes, implying more dilute damage compared with heavier ions. However, ion mass dependent APs' size effect was lost by loading the same damage profile and randomly positioning the I's and V's. Consequently, the damage morphology, as well as the annealing behavior obtained by reading I, V damage profiles is substantially different from those obtained using the much more realistic cascades generated by BCA.

4.1 Introduction

In process simulators, implant damage distribution in terms of interstitials (I) and vacancies (V) is commonly generated by means of an analytical approximation or a binary collision approximation (BCA) code. It has been shown using an atomistic non-lattice kMC simulator [Jaraiz et al., 2001], that the spatial correlation of the (I,V) Frenkel pairs is not critical for modeling transient enhanced diffusion (TED) in cases without impurity-point defect clusters [Martin-Bragado et al., 2004]. Whether the initial coordinates of the particles are provided by a BCA simulator or randomly generated following the concentration distribution of an input profile, TED simulation results are similar. This chapter looks at whether the same is true for damage accumulation and amorphization. Can one also simply use damage profiles to predict amorphization taking into account temperature and dose rate effects or is it necessary to use the 3D coordinates of I's and V's provided by BCA?

4.2 Model

In process simulations, ion-implant induced Frenkel pairs can be obtained directly from BCA, preserving the I, V spatial correlation, or they can be randomly generated from separate I and V input concentration profiles. These input profiles may be obtained from analytical approximations or from previously saved binary collision simulations. Since the concentration profiles are translated into discrete atoms whose particle coordinates in the atomistic simulator are genarated by a random number generator, all I, V spatial correlation is lost. Although the internal spatial configuration of the APs is not important in this model, it is useful to test if the spatial correlation of I, V within a cascade is critical in modeling damage accumulation. Implant simulations were done using damage generated directly by BCA or by loading I, V concentration profiles from the same BCA simulations as

inputs. The implant simulations were performed at low temperature (100 K) to avoid dynamic annealing, in order to compare their initial damage morphology. In addition, in this chapter, the amorphization mechanism has been disabled, so that the APs damage morphology can be analysed without them being converted into amorphous damage, thereby losing information on their size distribution.

4.3 Results

Figure 4.1 shows the AP histograms resulting from BCA implants of C and Xe at different damage concentrations. Implantation parameters were varied so as to achieve a relatively constant damage concentration across the simulated depth. See Table 4.1 for details on the actual simulation conditions. As heavier implant ions generate more damage for the same implant energy, a smaller dose of Xe compared to C is required to achieve the same level of damage.

The same level of damage is attained by APs of various different sizes depending on the nature of the implant ion. The concentration of APs is obtained from the sum over all nI and mV. C (12 u) being a lighter implant ion, generates APs of smaller sizes compared to Xe (132 u). At all damage levels, the AP size distribution obtained from the heavier implant ion is broader. The shapes of the AP histograms for both implant ions are similar at low damage concentrations. The concentration of APs increases proportionally with increasing damage concentration, indicating isolated collision cascades. For a damage concentration of $1 \times 10^{21}\,\mathrm{cm}^{-3}$ (see Fig. 4.2 for Xe), the AP histogram has higher proportion of larger-sized APs, implying the overlapping of APs.

The difference in size distribution of the APs generated by C and Xe BCA implants at the same damage concentration of $1 \times 10^{20}\,\mathrm{cm}^{-3}$ can be more clearly seen from the 2D color maps (2D histograms) shown in Fig. 4.3. There is a small but distinct net balance towards the V axis, indicating a deficit of atoms in the

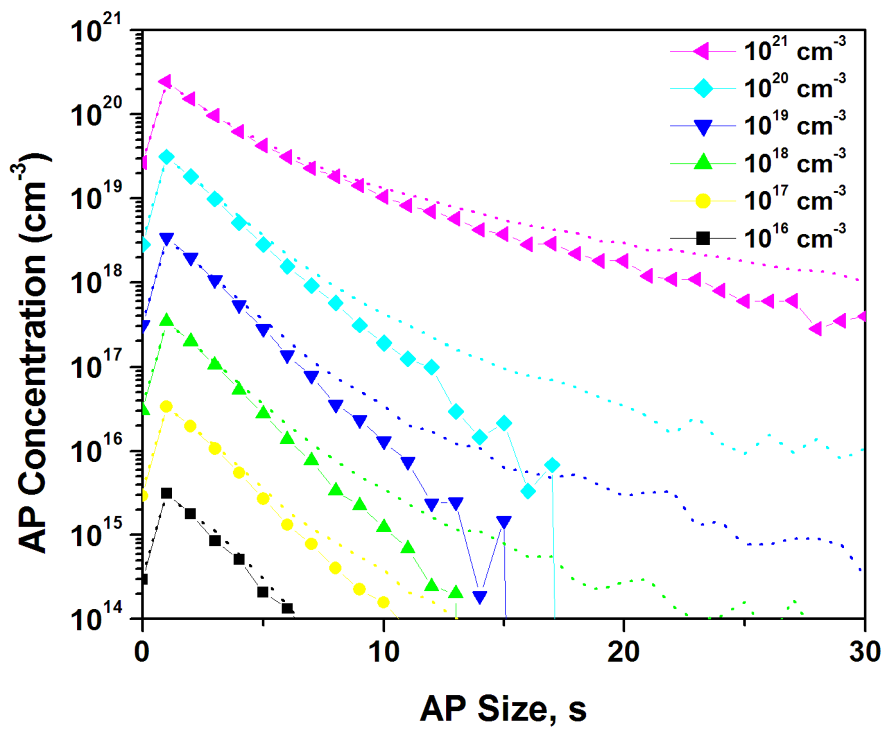

Figure 4.1: AP histograms obtained from C (lines with symbols) and Xe (dotted lines) implants using BCA at different damage concentrations. Implantations were simulated with conditions specified in Table 4.1.

Table 4.1: Details on implantation parameters used in the simulations to attain the same level of damage induced by C (10 keV) and Xe (80 keV). Dose rate and temperature were kept constant at 5×10^{12} cm^{-2}s^{-1} and 100 K respectively.

Damage Concentration (cm^{-3})	Carbon	
	Simulation Size (nm^3)	Dose (cm^{-2})
10^{21}	50×210×210	2×10^{13}
10^{20}	50×650×650	2×10^{12}
10^{19}	50×2000×2000	2×10^{11}
10^{18}	50×3150×3150	2×10^{10}
10^{17}	50×5000×5000	2×10^{9}
10^{16}	50×5000×5000	2×10^{8}

Damage Concentration (cm^{-3})	Xenon	
	Simulation Size (nm^3)	Dose (cm^{-2})
10^{21}	50×450×450	2.2×10^{12}
10^{20}	50×1200×1200	2.2×10^{11}
10^{19}	50×3150×3150	2.2×10^{10}
10^{18}	50×5000×5000	2.3×10^{9}
10^{17}	50×7000×7000	2.2×10^{8}
10^{16}	50×7000×7000	2.2×10^{7}

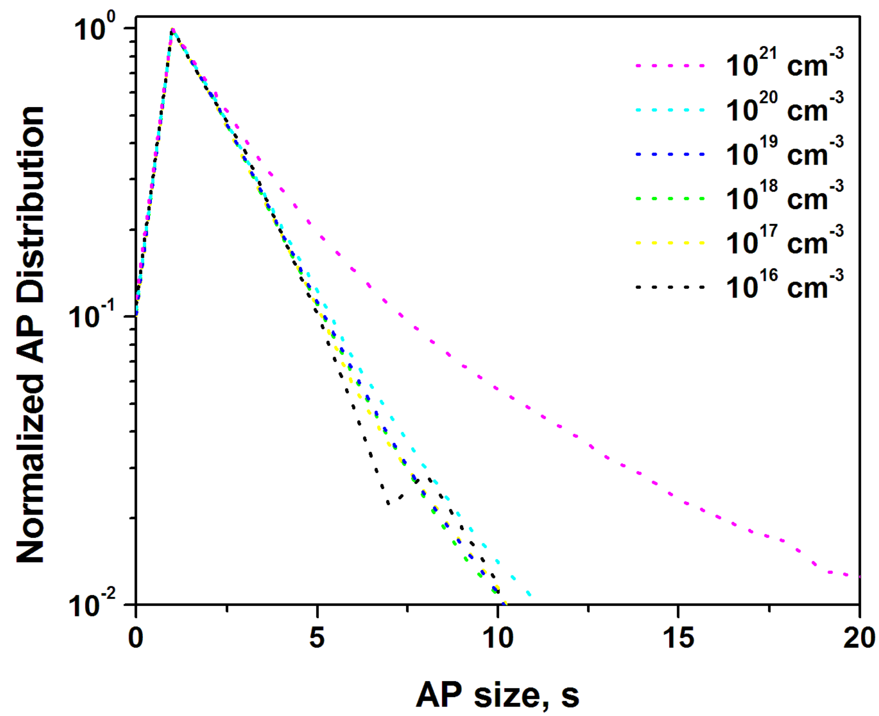

Figure 4.2: Normalized AP distribution obtained from Xe implants using BCA at different damage concentrations. Implantations were simulated with conditions specified in Table 4.1.

APs, in agreement with MD study [Nordlund et al., 1998], despite the fact that a binary collision program has been used for the development of the collisional phase of the cascades in this case. Not shown in the color map is the presence of a higher amount of isolated interstitial point defects compared to vacancy point defects, also in agreement with Ref. [Nordlund et al., 1998].

The dependence of the size of APs with ion mass allows for the modeling of dynamic annealing, which accounts for ion mass effects. MD simulations have shown that larger APs are more stable as evidenced by their higher apparent activation energy for recrystallization [Caturla et al., 1996]. Taking activation energy for recrystallization to be size-dependent, whereby the activation energy increases with size of APs, a higher implant temperature will be required to dynamically anneal larger defects. As APs generated by heavier implant ions are extended towards larger sizes, this enables the modeling of the amorphous-crystalline transition temperature, which increases with ion mass [Goldberg et al., 1995].

Instead of using BCA implant, the I's and V's can be generated by loading a damage concentration profile. Without using the BCA code to directly generate the implant cascades, the defect particle coordinates were obtained from the concentration profile randomly, thereby losing all the I, V spatial correlation.

Figure 4.4 shows the AP histograms resulting directly from BCA implants of H, C and Xe and by reading damage profiles of C and Xe from the same BCA simulations. In the simulaton for H, a simulation size of $50\,\mathrm{nm}\times100\,\mathrm{nm}\times100\,\mathrm{nm}$ was used. H was implanted at 8 keV up to a dose of $3\times10^{14}\,\mathrm{cm}^{-2}$, at 100 K and a dose rate of $5\times10^{12}\,\mathrm{cm}^{-2}\mathrm{s}^{-1}$. In all cases, the total damage concentration is about $1\times10^{20}\,\mathrm{cm}^{-3}$. Using BCA implants, the AP size dependence on implant ion mass is clearly evident. By reading damage profiles, the ion mass effect on APs is lost and the concentration of APs is much lower compared to those obtained from BCA (the damage missing in the histograms is in the form of isolated I's and V's). Furthermore, they are concentrated at very small sizes, even smaller than those

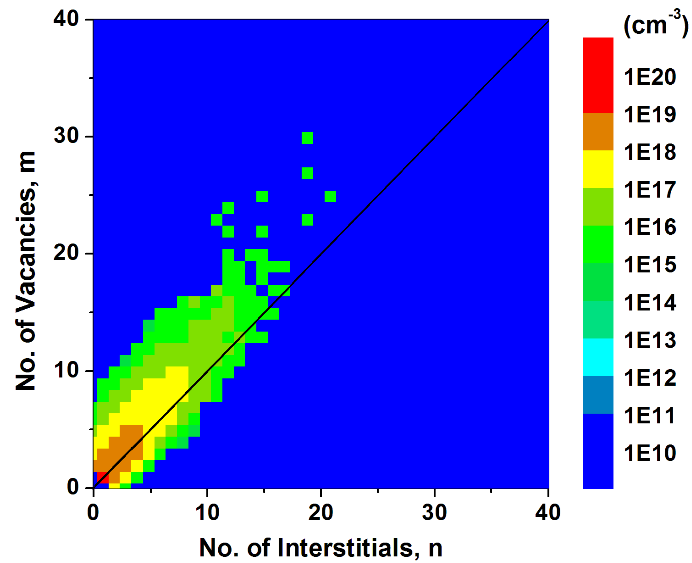

(a)

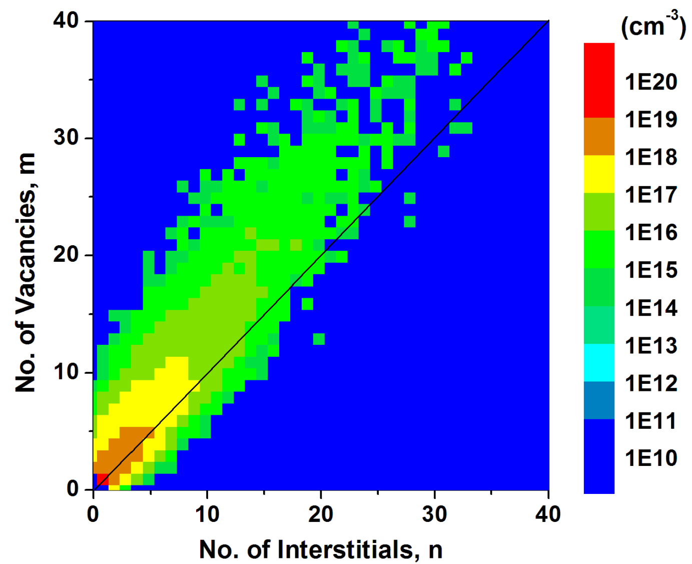

(b)

Figure 4.3: 2D color maps showing the AP size distribution at a constant damage of $1 \times 10^{20}\,\mathrm{cm}^{-3}$ generated by BCA implants of (a) C and (b) Xe.

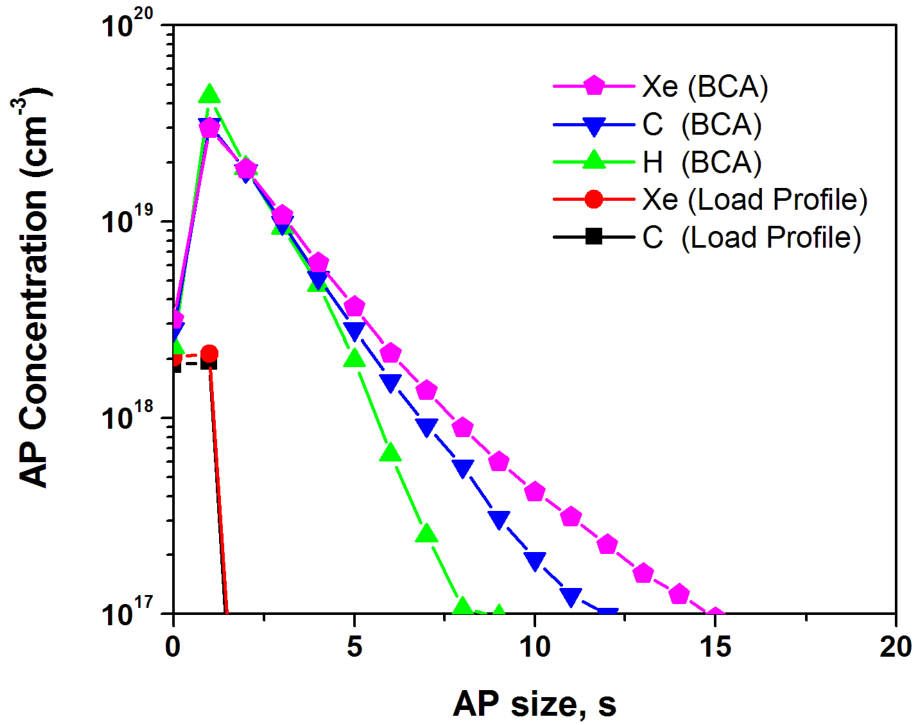

Figure 4.4: AP histograms at a constant damage concentration of $1 \times 10^{20}\,\text{cm}^{-3}$, of BCA H, C and Xe implants and by loading damage profiles of C and Xe.

APs generated by a BCA implant of a very light implant ion, like H. As the I, V coordinates are randomly generated by reading damage profiles, the I, V defects are more likely to be point defects instead of being close enough to form APs.

4.4 Conclusion

In summary, I, V spatial correlation (the three-dimensional cascade structure) is important in order to take into account ion mass effects. Even though AP recrystallization rate is only size dependent and does not take into account internal spatial configuration of the AP, the I, V spatial correlation is important in order to form the initial APs with a size distribution dependent on ion mass. For the same damage level, simulations by BCA, which preserves the I, V spatial correlation, resulted in AP sizes with ion mass dependence, with lighter implant ions generating more dilute damage. This ion mass dependent APs' size effect was lost by reading the same damage profile and randomly positioning the I's and V's. Therefore, in order to model damage accumulation taking into account the ion mass effect, it is essential to keep the spatial correlation of the I's and V's in the collision cascades as generated by BCA (or by MD).

Chapter 5

Model Validation

In the earlier chapter, it has been shown that different AP size distributions can be produced by different ion masses with direct BCA implantation. Although it is more efficient to read damage profiles either from analytical approximation or from previously saved BCA simulations, the loss of I, V spatial correlation results in the loss of APs' size distribution dependence on ion mass. Therefore, the rest of the simulations shown in this thesis have been done by direct BCA implantation. In this chapter, this physically-based damage accumulation model is shown to be able to simulate a diverse range of interesting experimental observations. The model can reproduce the amorphous-crystalline transition temperature in Si for a range of ions from C to Xe, the amorphous layer thickness in a range of amorphizing implants, the superlinear increase in damage accumulation with dose, and the two-layered damage distribution observed along the path of a high-energy ion. In addition, this model is able to distinguish between dynamic annealing and post-cryogenic implantation annealing, showing that dynamic annealing is more effective in removing damage than post-cryogenic implantation annealing at the same temperature.

5.1 Amorphous-Crystalline Transition Temperatures

As mentioned in Chapter 3, experimental data from Ref. [Goldberg et al., 1995] was used to determine the model parameters in this work. The experimental data corresponds to the amorphous-crystalline transition temperatures, as a function of dose rate, for (100) Si implanted with 80 keV ions to a dose of $1 \times 10^{15}\,\mathrm{cm}^{-2}$ for Si, Ar, Ge, Kr and Xe, and $2 \times 10^{15}\,\mathrm{cm}^{-2}$ for C. In the experiments, the amorphous-crystalline transition temperature was the temperature at which an amorphous layer first appeared. Likewise, in the simulations, the transition temperature was determined as the maximum temperature that resulted in a buried continuous amorphous layer. Figure 5.1 shows the best fit lines obtained from the simulations of each ion. The model was able to very accurately reproduce all the experimental data for different ion masses, dose rates and implant temperatures. In the case of noble gas implant simulations, the amorphization threshold was found to be lower than expected, and this is interpreted in terms of the lattice weakening effect of these non-bonding atoms, as will be discussed below.

Although it was possible to fit any single species with different activation energy functions by varying the appropriate prefactor, the constraints imposed by the wide range of ion masses resulting from the use of multiple species used in the calibration left practically no room for arbitrary assignments. Namely, with other activation energy assignments, there was insufficient temperature discrimination at either the high or low ion mass ends. The characteristic experimental activation energies for each ion, extracted from Ref. [Goldberg et al., 1995], are indicated in Table 3.3.

The amorphous-crystalline transition can be understood as the critical balance between damage generation and dynamic annealing. For Si [Goldberg et al., 1995, Schultz et al., 1991], this critical amorphous-crystalline transition temperature is close to room temperature. Therefore, in this temperature range, the annealing time as determined by the dose rate, will have a significant influence on the damage,

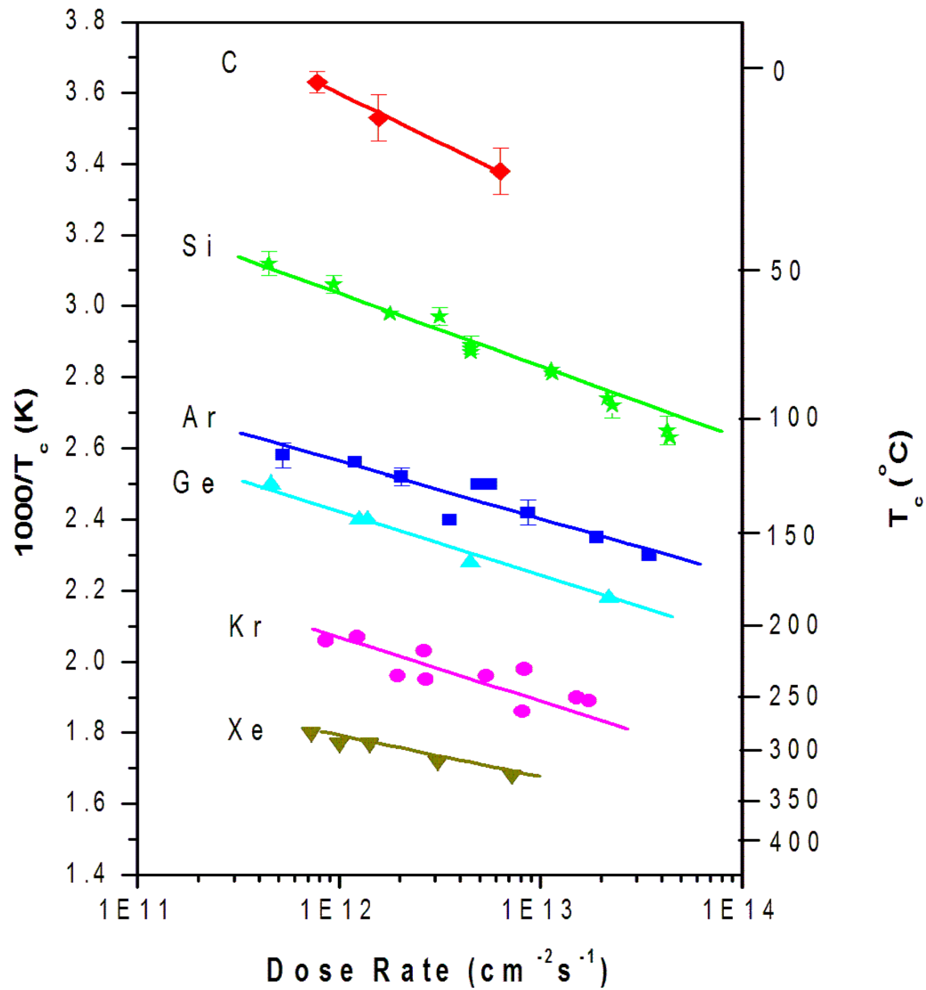

Figure 5.1: Simulation (lines) compared to experimental data (symbols) from Ref. [Goldberg et al., 1995] for amorphous-crystalline transition temperatures as a function of dose rate, for (100) silicon implanted with 80 keV ions to a dose of $1 \times 10^{15}\,\mathrm{cm}^{-2}$ for Si, Ar, Ge, Kr and Xe, and $2 \times 10^{15}\,\mathrm{cm}^{-2}$ for C.

which could range from minimally defected to fully amorphized. As dose rate increases, the time between the arrival of cascades decreases, reducing dynamic annealing, thereby resulting in increased damage accumulation. The nucleation of a buried, continuous amorphous layer and ultimately its thickness, depends on the dose rate and substrate temperature, especially under conditions where dynamic defect annealing is significant.

Likewise, for heavy ions, the critical amorphous-crystalline transition temperature is much higher than the room temperature implantation condition usually used. Therefore, it has been commonly observed that for heavy ions, substrate temperature and dose rate do not affect the kinetics of amorphization much, at least for ordinary room temperature implantations.

5.2 Noble Gas Effect

A peculiar behavior was observed for the noble gas implants. Although Ar has an ion mass between those of Si and Ge, its simulated transition temperature using the same activation energy function (shown in Fig. 3.3), was lower than the experimental value. This means that Ar amorphizes Si more easily than expected based on ion mass effect alone. This conjecture was clearly confirmed (see Fig. 5.2), when the experimental activation energies from Ref. [Goldberg et al., 1995] was plotted as a function of ion mass. This additional effect is attributed to the non-bonding character of noble gas atoms, compared to the group-IV elements. The presence of these non-bonding atoms weakens the silicon lattice locally and, in consequence, the lattice collapses to the amorphous state before the regular amorphization threshold is reached. This silicon lattice weakening effect by noble gas atoms has been verified by MD studies on silicon sputtering yield with Ar ions [Marques et al., 1997].

Assuming a linear dependence with non-bonding atom concentration, a certain "already amorphized" volume (V_{am} =1.5 nm^3) is assigned to each implanted noble gas ion, so that they can effectively lower the amount of cascade-generated damage necessary to reach the amorphization threshold. As a first approximation, the same volume V_{am} was assumed for Ar, Kr and Xe. Although the number of implanted noble gas ions, as well as V_{am} is the same in all cases (same dose), both the experimental data (see Fig. 5.2) and the simulations suggest that this chemical (non-bonding atoms) effect becomes negligible for heavy noble gas ions. This can be understood by the fact that the transition temperature (and the corresponding activation energy) is such that the excess damage is annealed out. For a light noble gas ion like Ar, V_{am} is comparable to this excess damage per cascade, but it is negligible compared to the excess damage of a heavy ion cascade. Therefore, there is almost no difference in the temperature and activation energy needed to

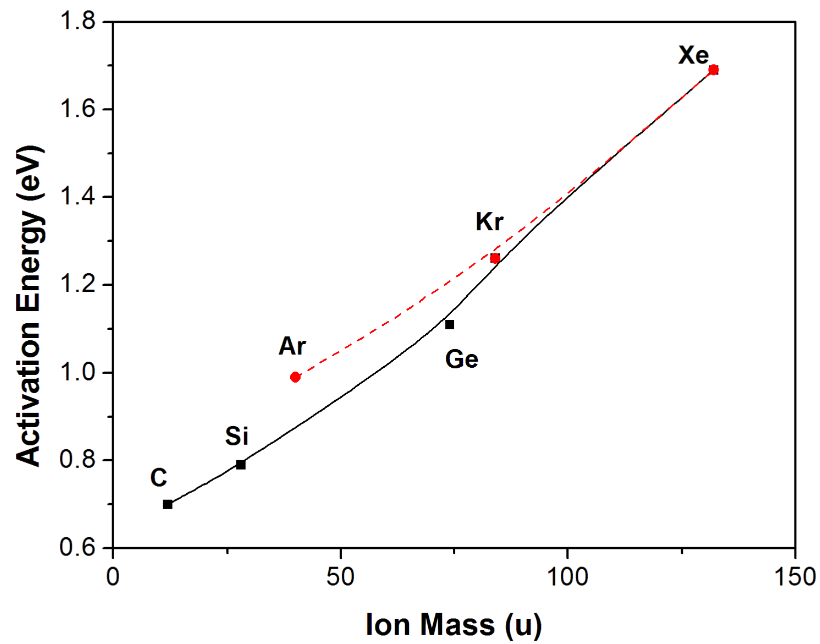

Figure 5.2: Activation energy of recrystallization as a function of ion mass from experimental data [Goldberg et al., 1995]. (Lines drawn to guide the eyes.)

anneal out the excess damage for a heavy ion whether it is a noble gas (non-bonding atom) or not.

5.3 Amorphous Layer Thickness

Figure 5.3 shows a sequence of simulations illustrating the development of the amorphous layer in Si with increasing dose of Si implanted at 300 keV, 300 K and a dose rate of $1.5 \times 10^{12}\,\text{cm}^{-2}\text{s}^{-1}$, following the experimental conditions in Ref. [Maszara and Rozgonyi, 1986].

The simulations are comparable with experimental cross-sectional transmission electron microscopy (TEM) micrographs in Ref. [Maszara and Rozgonyi, 1986]. Initially, at a dose of $1 \times 10^{15}\,\text{cm}^{-2}$, a buried amorphous layer is formed. The amorphous layer increases in thickness with increasing dose, reaching the surface at a dose of $5 \times 10^{15}\,\text{cm}^{-2}$.

In addition, the morphology of the amorphous-crystalline interface is also well-represented in the simulations. Due to damage straggling and dynamic annealing, a transition zone containing both amorphous and crystalline material exists, instead of an absolutely planar interface. Experimentally, the width of the transition zone has been observed to decrease with increasing amorphous layer thickness [Maszara and Rozgonyi, 1986]. This is also reproduced by the simulations.

In Section 5.1, the effect of dose rate on damage accumulation can be seen, as the amorphous-crystalline transition temperature is a function of dose rate. Under certain implant conditions, variation in dose rate has also demonstrated a strong effect on the amorphous layer thickness. From Ref. [Robertson et al., 1997], when the dose rate was increased by an order of magnitude, the amorphous layer thickness resulting from Si implant at 20 °C, also increased by 10 %. This difference in amorphous layer thickness was then shown to result in different end-of-range defect (dislocation loops) densities after subsequent annealing.

The same trend on amorphous layer thickness as a result of dose rate is also apparent from simulations. Figure 5.4 shows the amorphous layer thickness as a function of dose rate. The amorphous layer thicknesses were the result of 80 keV

Si implants at room temperature up to a dose of $1 \times 10^{15}\,\mathrm{cm}^{-2}$.

As mentioned, the critical amorphous-crystalline temperature for Si is close to room temperature. Therefore, for room temperature implants, the dose rate will have significant impact on damage accumulation and thereby the amorphous layer thickness. In this case, the time between the arrival of cascades was varied over 2 orders of magnitude. By decreasing the amount of dynamic annealing through increasing the dose rate, less APs are recrystallized, resulting in more damage accumulation and thicker amorphous layer.

In all the simulations shown in this work, a constant amorphization threshold of $1.5 \times 10^{22}\,\mathrm{cm}^{-2}$ was used. The amorphization threshold has been previously reported to decrease with increasing dose rate [Haynes and Holland, 1991] (or to increase with increasing substrate temperature [Laanab et al., 1993]). However, in this model, the change in amorphous layer thickness is a direct result of the AP recrystallization rates.

5.3.1 Ge Preamorphization Implants

From a practical, technological point of view, accurate prediction of the depth of the amorphous layer is important, especially for Ge pre-amorphization implant (PAI). This is because the formation of *p*-type ultra-shallow junction is often preceded by a Ge PAI step. This limits channeling of the subsequent low-energy B, so that the as-implanted B profile is shallower and more abrupt. The main drawback of this approach is the presence of residual defects in the end-of-range region, just beyond the original amorphous-crystalline interface [Lindsay et al., 2003]. As the number of the interstitials stored in the end-of-range after recrystallization critically depends on the position of the amorphous-crystalline interface [Avci et al., 2001], accurate simulation of the amorphous layer thickness is crucial as it impacts damage evolution during the subsequent annealing step, with significant consequences on dopant diffusion and activation.

Figure 5.5 shows the amorphous layer thickness as a function of implant energy for Ge PAI. Ge was implanted up to a dose of $1 \times 10^{15}\,\mathrm{cm}^{-2}$ in all cases, for a range of energy from 2 to 30 keV. Since temperature and dose rate were not specified from the various references [Pawlak et al., 2002, Cristiano et al., 2004, Lindsay et al., 2004, Hamilton et al., 2005], room temperature and a dose rate of $1 \times 10^{13}\,\mathrm{cm}^{-2}\mathrm{s}^{-1}$ were used in all the simulations. When specified, the experimental characterization methods by Rutherford Backscattering Spectromety (RBS) or cross-sectional Transmission Electron Microscopy (x-TEM) are indicated in Fig. 5.5. As the amorphous-crystalline transition temperature for 80 keV, $1 \times 10^{15}\,\mathrm{cm}^{-2}$ Ge implant is much higher than room temperature [Goldberg et al., 1995], it can be deduced that damage accumulation and amorphization for Ge implantation for the simulated conditions are not very sensitive to dose rate and temperature effects. A test was done for 20 keV Ge implant simulation. By varying the dose rate over an order of magnitude ($10^{12}\,\mathrm{cm}^{-2}\mathrm{s}^{-1}$-$10^{14}\,\mathrm{cm}^{-2}\mathrm{s}^{-1}$), the change in amorphous layer thickness is approximately ± 3 nm, or less than 10 %. However, this small difference can account for the discrepancies between experimental and simulated amorphous layer thicknesses.

Figure 5.6 shows the amorphous layer thickness resulting from Ge PAI as a function of dose. 150 keV Ge was implanted to doses ranging from $1 \times 10^{15}\,\mathrm{cm}^{-2}$ to $8 \times 10^{15}\,\mathrm{cm}^{-2}$. As temperature and dose rate were not specified in the experimental procedure [Colombeau et al., 2001], room temperature and a dose rate of $1 \times 10^{13}\,\mathrm{cm}^{-2}\mathrm{s}^{-1}$ were again assumed for the simulations. The discrepancy between 3-11 % between the simulated and experimental amorphous layer thickness may be attributed to the unspecified conditions of temperature and dose rate. However, it should also be noted that this discrepancy increases with increase in dose. This could either be due to the increased beam heating effect in the experiment, which led to increased dynamic annealing, or due to the fact that the calibration of model parameters was based on experiments, whereby the dose was $1 \times 10^{15}\,\mathrm{cm}^{-2}$.

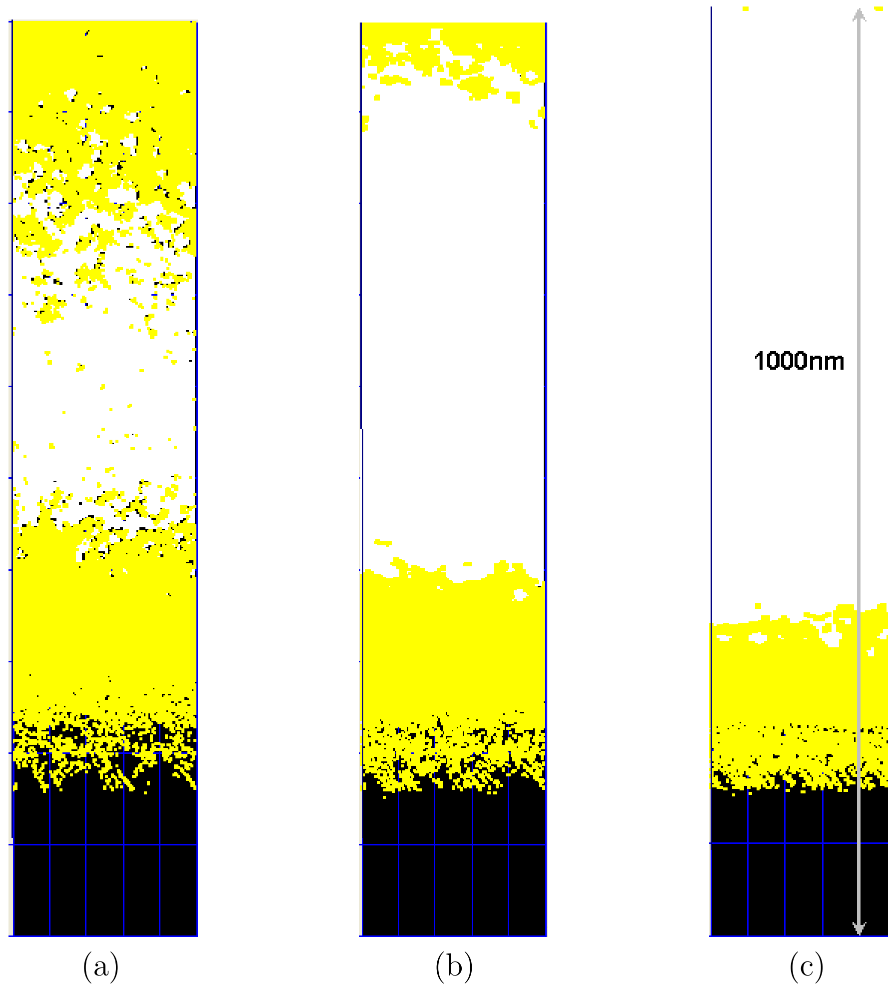

Figure 5.3: Sequence of simulations showing the development of the amorphous layer in silicon with increasing dose of 300 keV Si (a) $1 \times 10^{15}\,\mathrm{cm}^{-2}$, (b) $2 \times 10^{15}\,\mathrm{cm}^{-2}$, (c) $5 \times 10^{15}\,\mathrm{cm}^{-2}$, implanted at 300 K with a dose rate of $1.5 \times 10^{12}\,\mathrm{cm}^{-2}\mathrm{s}^{-1}$. White represents amorphous regions and yellow represents amorphous pockets.

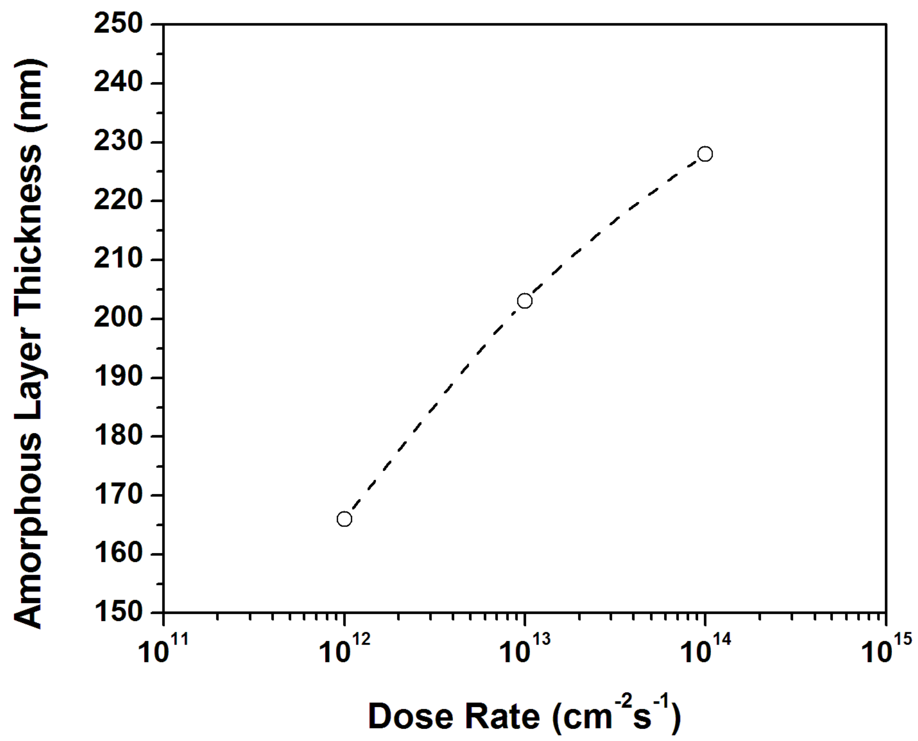

Figure 5.4: Simulated amorphous layer thickness as a function of dose rate for 80 keV, $1 \times 10^{15}\,cm^{-2}$ Si implant at room temperature.

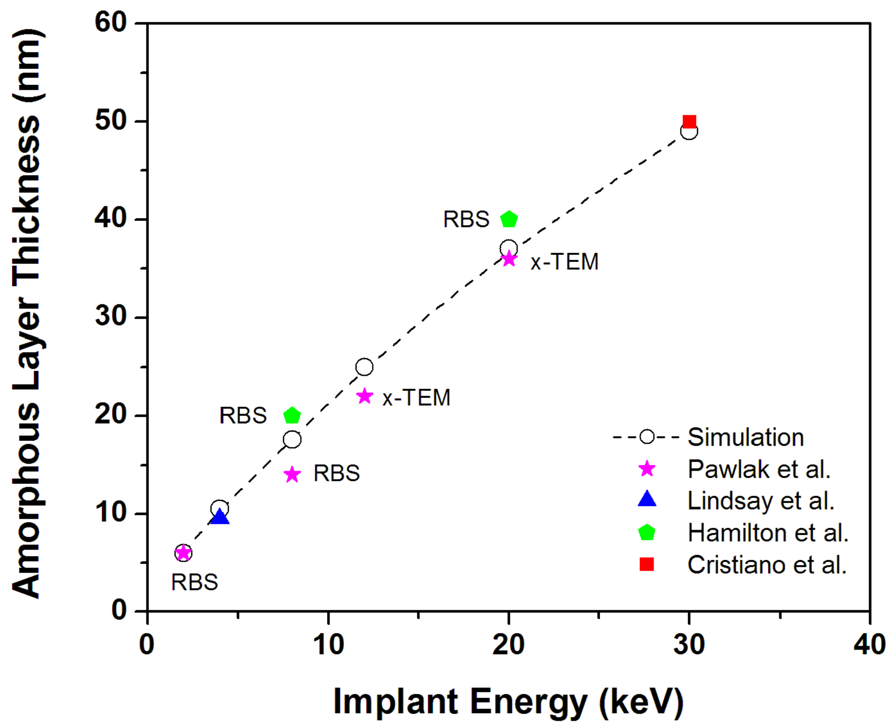

Figure 5.5: Amorphous layer thickness as a function of implant energy for Ge PAI at a dose of $1 \times 10^{15}\,\mathrm{cm}^{-2}$. Simulations were done at room temperature and at a dose rate of $1 \times 10^{13}\,\mathrm{cm}^{-2}\mathrm{s}^{-1}$. Filled symbols represent experimental data [Pawlak et al., 2002, Cristiano et al., 2004, Lindsay et al., 2004, Hamilton et al., 2005], open symbols are from simulations. Experimental characterization methods are indicated when specified.

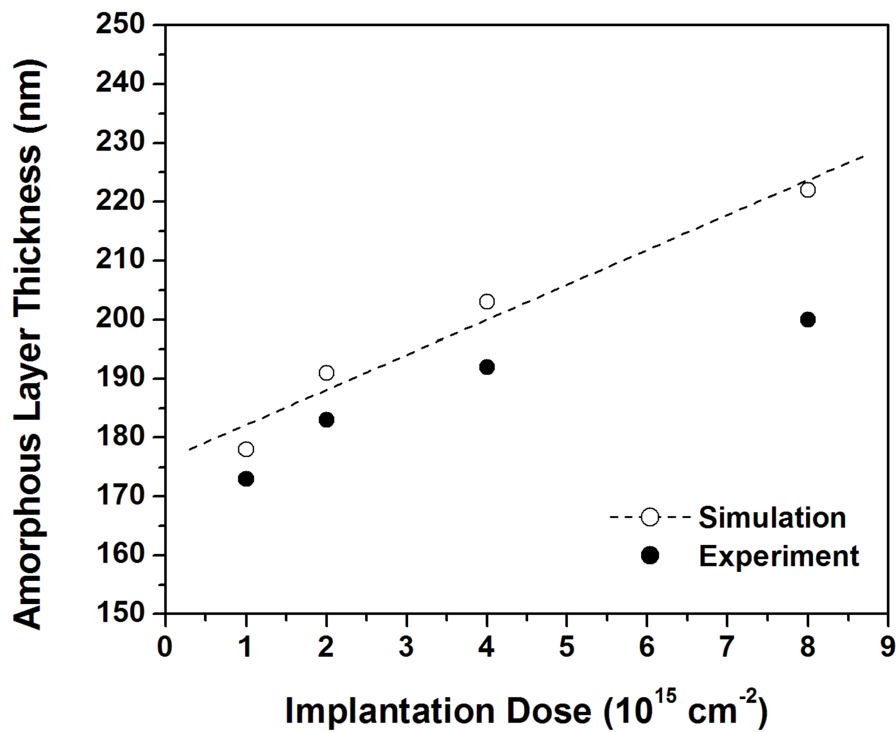

Figure 5.6: Amorphous layer thickness as a function of dose for 150 keV Ge PAI. Simulations were done at room temperature and at a dose rate of $1 \times 10^{13}\,\mathrm{cm}^{-2}\mathrm{s}^{-1}$. Filled symbols represent experimental data measured by TEM [Colombeau et al., 2001], open symbols are from simulations.

5.4 Dose Effect

Figure 5.7 shows the experimental [Holland et al., 1989] and simulated results for damage accumulation as a function of dose for 100 keV Si implant at room temperature. A dose rate of $5 \times 10^{12}\,\mathrm{cm^{-2}s^{-1}}$ was used in the simulations, consistent with the experimental procedure, which states that less than $1.2 \times 10^{13}\,\mathrm{cm^{-2}s^{-1}}$ was used. Initially, damage from low dose implantation increases slowly with dose, until a critical dose ($2 \times 10^{14}\,\mathrm{cm^{-2}}$) is reached. This is because the damage (amorphous pockets) generated is relatively dilute and not stable enough, and therefore it is easily recrystallized by dynamic annealing. Subsequently, damage increases sharply within a narrow dose range as the amorphous pockets become more stable, such that the rate of dynamic annealing is less than the rate of damage generation, resulting in effective damage accumulation. Finally, damage saturates as amorphization is reached, and further implantation only widens the amorphous layer.

An interesting feature that can be observed from Fig. 5.7 is the nature of the defect structures. Two different types of defect structures can be distinguished from simulations. They are, namely, the amorphous pockets and amorphous regions, which show different dose dependence. Initially, the dominant damage is the amorphous pocket. As the amorphous pockets increase in concentration, localized amorphous regions nucleate at a certain point (dose $\approx 2 \times 10^{14}\,\mathrm{cm^{-2}}$). After the nucleation of localized amorphized regions, the amorphous damage becomes increasingly more dominant at the expense of the amorphous pockets. From Fig. 5.7, it can be seen that the proportion of the defect types from simulation is remarkably consistent with experimental observations by Holland et al. [Holland et al., 1989], whereby the amorphous pockets in this model are analogous to the defects identified as divacancies in theirs. According to the authors, the divacancy-type defects are considered to be defect types that anneal around 250 °C.

Another experimental observation that can be reproduced by this model is

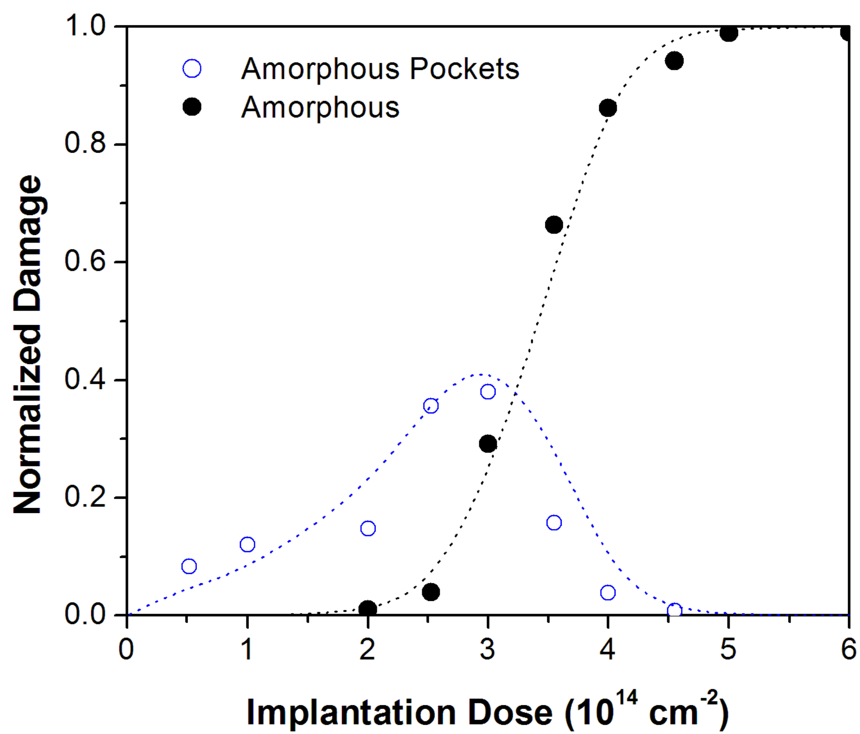

Figure 5.7: Dose dependence of damage produced by 100 keV Si ions at room temperature and a dose rate of 5×10^{12} cm^2. Symbols show different damage components determined from the experimental annealing results, dotted lines are results obtained from simulations. Experimental data from Ref. [Holland et al., 1989]. See also Fig. 2.14.

the damage distribution with increasing dose. Under certain implant conditions, two distinct damage layers may be observed in silicon samples by Rutherford Backscattering Spectrometry [Holland et al., 1988, Holland and White, 1991] (see Fig. 2.15). For example, for the damage accumulation in silicon induced by high energy (1.25 MeV) Si implant at room temperature, damage increases with dose up to amorphization near the end-of-range, while in the near surface region, damage saturates at a low level [Holland and White, 1991].

Holland *et al.* suggested that the near surface low level damage saturation could be explained by a homogeneous nucleation and growth damage accumulation model, whereby a dynamic balance exists between the various defect reactions considered relevant at room temperature. The various simple defect reactions include I-V recombination, defect clustering forming I_2 and V_2, and cluster recombination through point defect capture. The high damage region near the end-of-range was attributed to the imbalance in interstitials and vacancies due to additional atoms during implantation and the spatial separation of Frenkel pairs created during ion impact. As a result, amorphous Si nucleates, further upsetting the balance between the simple defect reactions, eventually leading to amorphization.

Figure 5.8 shows the simulated damage profile resulting from a high energy (1 MeV) Si implantation at room temperature at various doses. Based on this damage accumulation model, the two distinct damage layers were clearly reproduced. At a depth of around 1 μm, damage increases with dose until amorphization occurs at a dose of $1 \times 10^{15}\,\mathrm{cm}^{-2}$. At this depth, damage accumulates slowly up to a dose of $4 \times 10^{14}\,\mathrm{cm}^{-2}$. Beyond $4 \times 10^{14}\,\mathrm{cm}^{-2}$, there is a sudden growth of damage accumulation up to amorphization. This is in contrast with the near surface region, where damage accumulation increases slowly with dose up to $6 \times 10^{14}\,\mathrm{cm}^{-2}$ and subsequently saturates at a level regardless of the increase in implantation dose. Once a buried amorphous layer is nucleated, subsequent implantation would cause it to expand and extend towards the near surface region.

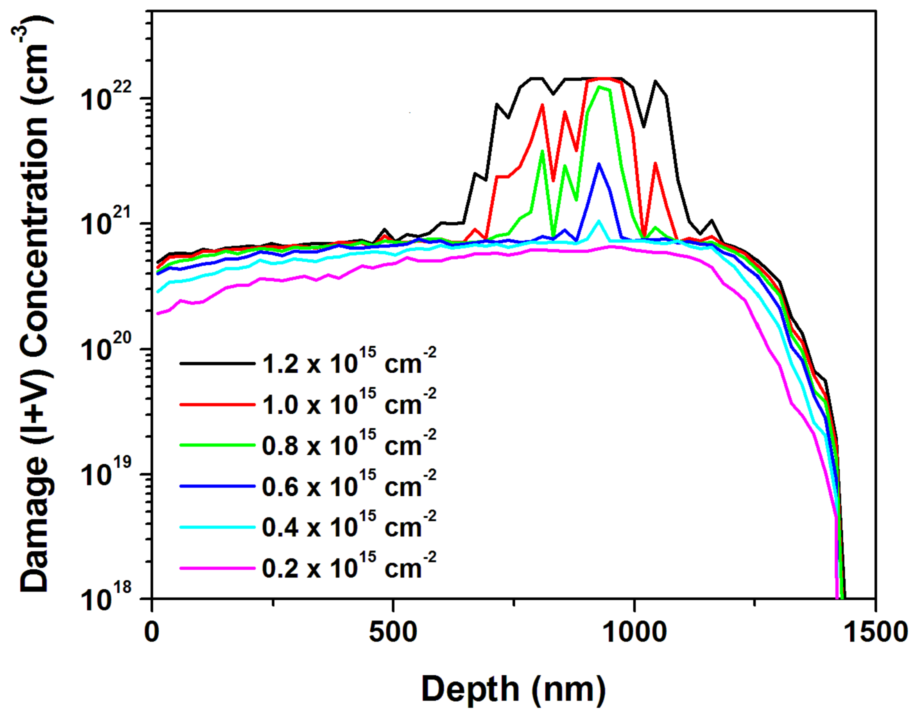

Figure 5.8: Simulated damage profile resulting from 1 MeV Si implantation at room temperature at various doses.

5.5 Temperature dependence

As mentioned, temperature has a significant effect on damage accumulation, such that the critical dose of amorphization is a strong function of the implant temperature. Besides the temperature dependence on implantation damage, another temperature effect that had been studied was the difference between dynamic annealing during the implantation and the post-implant annealing of cryogenic temperature implantation. Westmoreland *et al.* [Westmoreland et al., 1969] had shown that the anneal behavior of the damage created in Si by 200 keV B ions is a strong function of implant temperature. More specifically, it was found that dynamic annealing during implantation was more effective than annealing at the same temperature following a cryogenic temperature implantation.

Figure 5.9 shows the simulated normalized damage as a function of temperature for 80 keV C implantation at a dose rate of $5 \times 10^{12}\,\mathrm{cm^{-2}s^{-1}}$. For implantation with dynamic annealing, implantations were carried out at various temperatures up to a dose of $1 \times 10^{15}\,\mathrm{cm^{-2}}$ (that is, 200 s at implant temperature). Post-annealing of cryogenic temperature implantations were simulated by implanting at -150 °C and subsequently annealing at various temperatures for 10 minutes after each implantation. All data have been scaled to unity at 0 °C.

For a dose of $1 \times 10^{15}\,\mathrm{cm^{-2}}$, 0 °C is the amorphous-crystalline phase transition temperature of C implanted at 80 keV and $5 \times 10^{12}\,\mathrm{cm^{-2}s^{-1}}$, whereby a buried continuous amorphous layer is formed. Implantations at higher temperatures result in damaged Si, but not enough to cause a transition into the amorphous phase. Fig. 5.9 shows that the total normalized damage as a result of dynamic annealing is a strong function of temperature between 0 °C and room temperature. Damage decreases with increase in temperature due to the higher rate of dynamic annealing.

As for the cryogenic implants, implantation at -150 °C was performed up to a lower dose of $2 \times 10^{14}\,\mathrm{cm^{-2}}$ to prevent transition into amorphous phase. As a

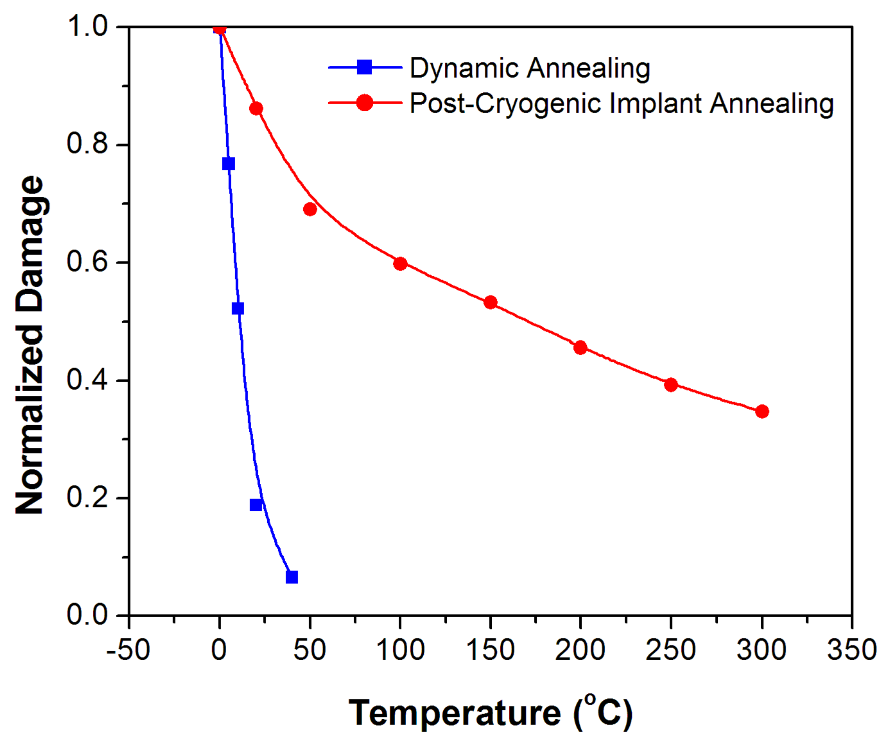

Figure 5.9: Simulated normalized damage as a function of temperature for 80 keV C implantations. Post-cryogenic implantation annealing represents 10 minutes annealing after cryogenic temperature implantation.

continuous amorphous layer of Si will recrystallize epitaxially at around 550 °C, it would be inappropriate to subject an amorphous layer to subsequent anneals at different temperatures. It can be seen from Fig. 5.9 that the damage resulting from cryogenic implantation is more stable, such that subsequent annealing removes a smaller proportion of the damage than dynamic annealing at the same temperature.

The difference between dynamic annealing and post-implantation annealing of cryogenic implantation is apparent in this model. Figure 5.10 shows the 2D color map of the amorphous pockets composition under different implantation and annealing conditions. Figure 5.10(a) shows that implantation at cryogenic temperature allows amorphous pockets to grow to large sizes. Subsequent annealing at 20 °C is only able to anneal the smaller amorphous pockets (with lower activation energy of recrystallization), while the larger amorphous pockets remain stable (see Fig. 5.10(b)). In comparison, when implantation is carried out at 20 °C, dynamic annealing of the amorphous pockets takes place between successive cascades. As a result, amorphous pockets are not allowed to grow to large sizes; instead, a growing population of small, pure I and V clusters result as the implantation proceeds. Based on this model, cryogenic temperature implantation allows amorphous pockets to grow to large sizes. Therefore, the damage will be more stable against an anneal at a given temperature than the damage generated by the same implantation at the same given temperature, in which the amorphous pockets are not allowed to grow as big (and thereby, as stable) due to dynamic annealing.

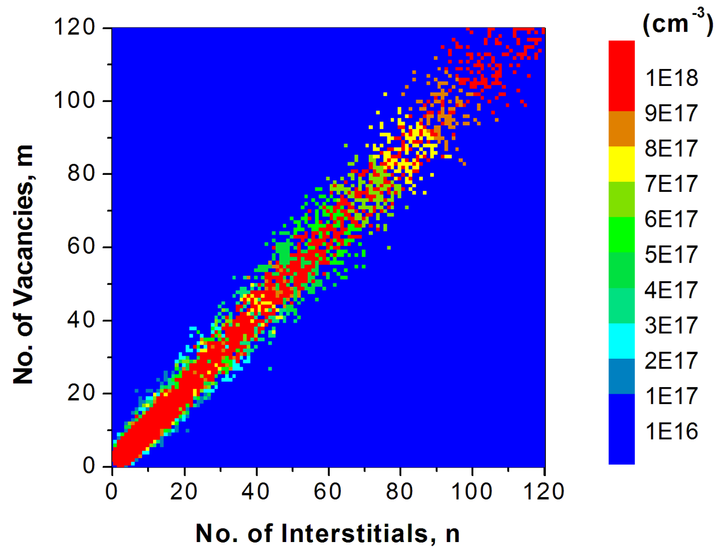

(a)

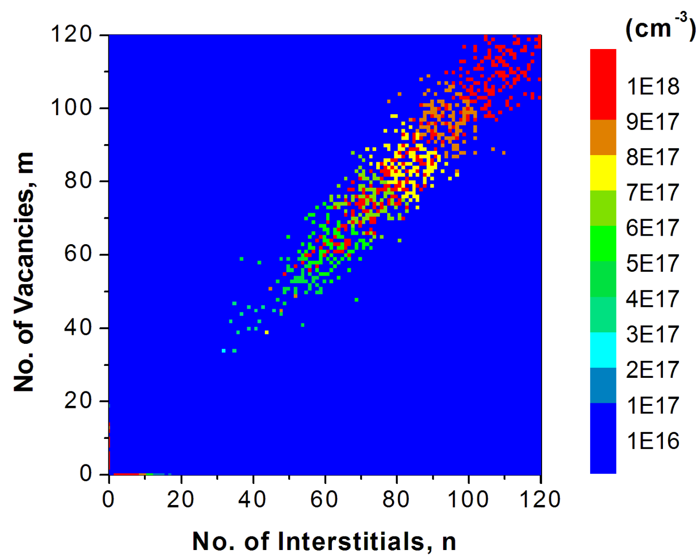

(b)

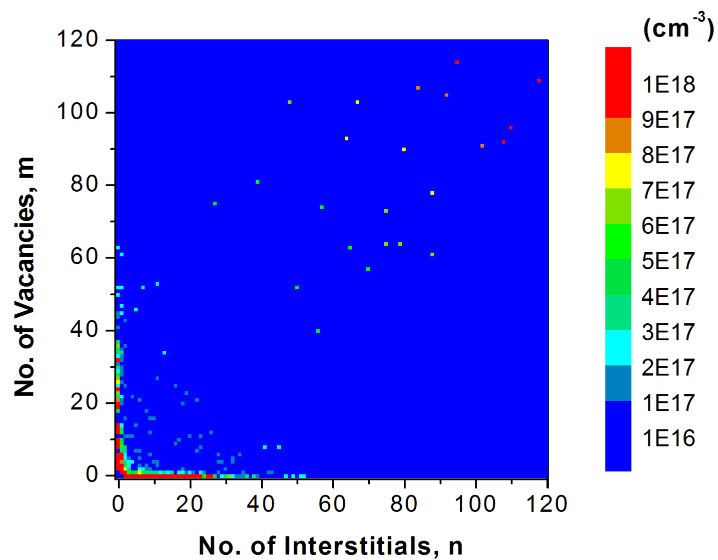

(c)

Figure 5.10: 2D histograms of APs composition at (a) cryogenic (-150 °C) C implantation to a dose of $2 \times 10^{14}\,\mathrm{cm}^{-2}$, (b) post-cryogenic implantation annealing at 20 °C, (c) 20 °C C implantation to a dose of $1 \times 10^{15}\,\mathrm{cm}^{-2}$ (dynamic annealing).

5.6 Conclusion

In summary, the damage accumulation model has been able to reproduce the ion-mass dependent silicon amorphous-crystalline transition temperature for a wide range of ions, from C to Xe, as a function of dose rate. In the case of the noble gas implant simulations, the amorphization threshold was found to be lower than expected.

Thickness of the amorphous layers are well-simulated in a range of amorphizing conditions. In terms of the dose effect, the proportion of amorphous pockets and amorphous damage has been reproduced as a function of dose. In addition, the two-layered damage distribution along the path of a high-energy ion can be simulated, as is consistent with experimental observations.

Lastly, this model is able to show that dynamic annealing is more effective at removing damage than post-cryogenic implantation annealing at the same temperature, as amorphous pockets are allowed to grow to larger (thus more stable) sizes during cryogenic implantation than is allowed by dynamic annealing.

Chapter 6

Bimodal Distribution of Damage Morphology

In Chapter 5, the damage accumulation model described in this work was validated against many experimental observations. Simulation results either showed the expected trends or rightly reproduced experimental data with different implantation parameters. In this chapter, this model was used to study the composition and size distribution of APs during different conditions of ion implantations. Due to their small size, the exact nature of the APs is not accessible experimentally. The simulations shown here can provide an analysis of the APs to gain a better understanding of this defect type. One can then postulate the implications of different ion implantation conditions on subsequent thermal annealing. Depending strongly on the dose rate, ion mass and implant temperature, the APs can evolve to a defect population where the agglomerates have a similar number of I and V (n≈m), or to a defect population with pure I (m≈0) or V (n≈0) clusters, or a mixture of both. This behavior corresponds to a bimodal (APs/clusters) distribution of damage. As the APs have different thermal stability compared to the I and V clusters, the same damage concentration obtained through different implant conditions have a different damage morphologies and, consequently, exhibit a different resistance to subsequent thermal treatments.

6.1 Introduction

Extensive experimental and theoretical studies have been done on damage induced by ion implantation. A complex and wide diversity of damage types have been revealed by various studies. The thermal stability of these different defect types has been studied extensively both theoretically and experimentally, and found to be very different. Pure I [Cowern et al., 1999c] and V [Bongiorno et al., 1998] clusters are more thermally stable than APs or amorphous regions, with higher activation energy for cluster emission than the activation energy for AP recrystallization [Marques et al., 2003, Donnelly et al., 2003, Jackson, 1988].

Using the damage model described earlier as an analysis tool, it reveals a bimodal (APs/pure clusters) distribution of damage. Therefore it can be used to predict not only the damage level but also its morphology obtained from different implant conditions. As the different damage types have different thermal annealing behavior, this has implications of practical relevance for silicon processing.

6.2 Model

As before, the model used has been described in detail in Chapter 3. In this model, pure interstitials (I_nV_0) and vacancy clusters (I_0V_m) are subsets of the APs. Pure interstitial clusters [Cowern et al., 1999c] and pure vacancy clusters [Bongiorno et al., 1998] have their own characteristic emission rates.

Figure 6.1 shows 2D histograms of APs of varying compositions (I_nV_m) for an 80 keV, $2 \times 10^{15}\,\mathrm{cm}^{-2}$ C implant at the amorphous-crystalline transition temperature (20 °C at a dose rate of $5 \times 10^{12}\,\mathrm{cm}^{-2}\mathrm{s}^{-1}$). The color represents the total concentration of I's and V's (sum over nI and mV) in APs of a given composition (I, V axes).

Initially, the carbon-induced cascades result in small APs that are unstable at

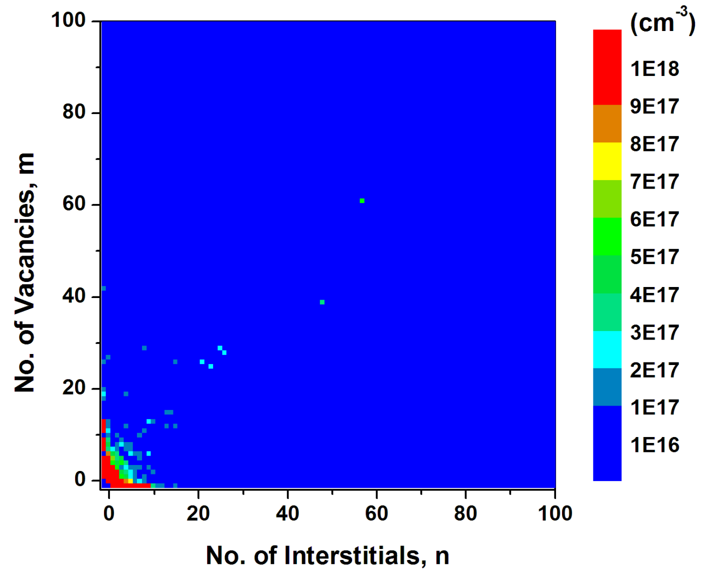

(a)

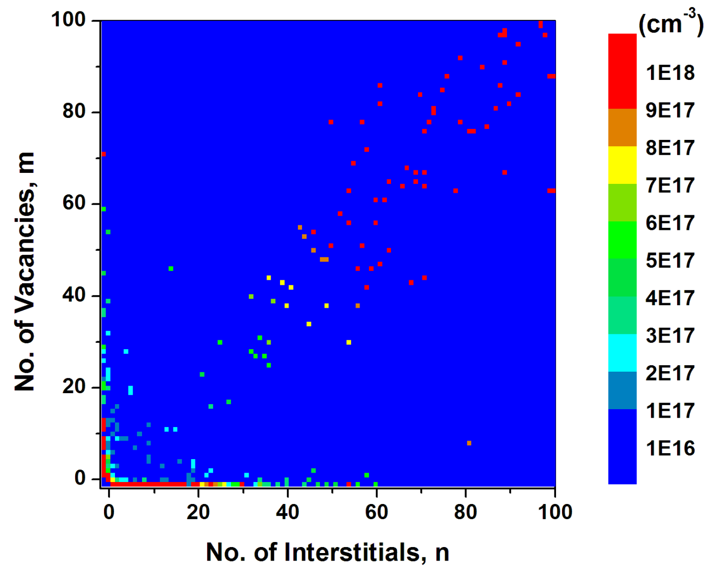

(b)

Figure 6.1: 2D histogram of AP composition of an amorphizing 80 keV Carbon implant at (a) 10% and (b) 80% of the total dose of $2 \times 10^{15}\,\mathrm{cm}^{-2}$. Simulations were done at 20 °C and at a dose rate of $5 \times 10^{12}\,\mathrm{cm}^{-2}\mathrm{s}^{-1}$.

the given temperature; therefore, they recrystallize, with the net excess of I and V in the APs behaving as small, pure I and V clusters (pixels adjacent to the axes). As a result, the initial damage morphology consists mainly of small clusters, with few APs accumulating to larger sizes (see Fig. 6.1(a)). As implantation proceeds, overlapping cascades resulting in larger APs, which are stable at the given temperature, can be observed from Fig. 6.1(b).

To attain the amorphous-crystalline transition with a heavier ion, the same amount of damage has to be accumulated. However, since heavier ion generates more damage and it is extended to larger APs sizes, damage (consisting of small APs) has to be removed up to larger sizes, which also results in more pure I or V clusters. This implies that different implantation conditions can lead to different substrate damage morphology. This model therefore presents a useful analysis tool that could give an insight to the damage morphology resulting from different implant conditions, and the consequences in the face of subsequent thermal treatments.

6.3 Results

A constant damage concentration of $1 \times 10^{21}\,\mathrm{cm}^{-3}$ was obtained from 80 keV Si implant at a constant dose rate of $5 \times 10^{12}\,\mathrm{cm}^{-2}\mathrm{s}^{-1}$ using different combinations of dose and temperature. The different damage morphology after each implant is shown in Fig. 6.2. Damage morphology in terms of APs with a well-balanced distribution of I, V can be obtained with a low temperature implant, where dynamic annealing can be assumed to be negligible. At some intermediate temperature, a bimodal distribution with a mixture of pure clusters and APs is obtained. At high implant temperature, damage accumulates as pure I or V clusters only (pixels adjacent to the axis).

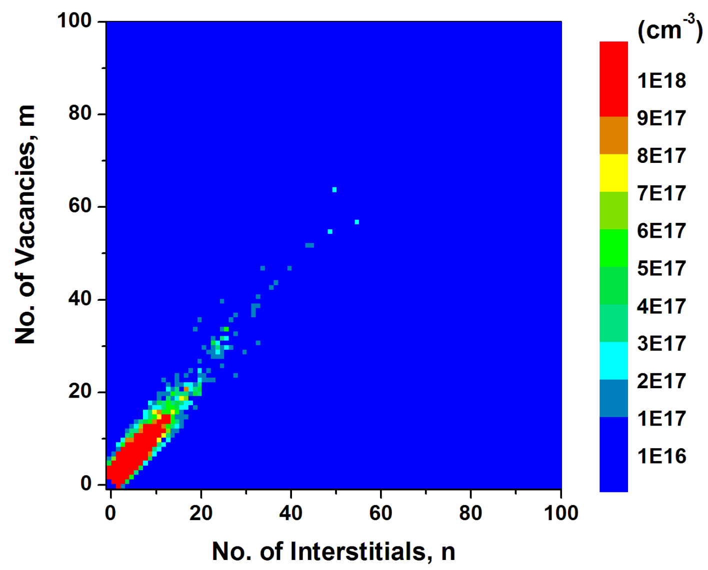

(a)

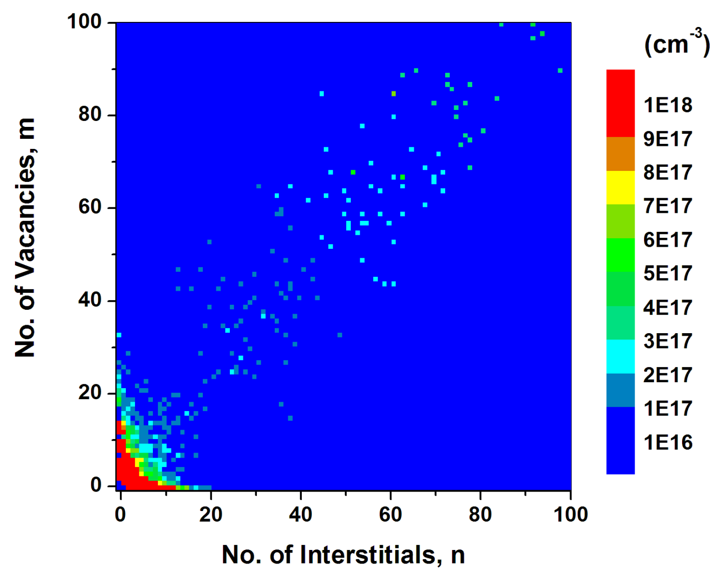

(b)

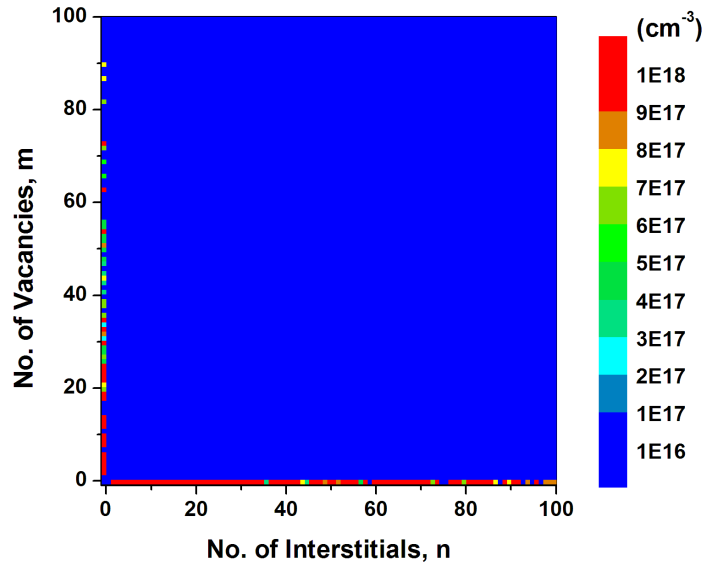

(c)

Figure 6.2: 2D histograms of AP composition showing damage composition at a constant damage level of $1 \times 10^{21}\,\mathrm{cm}^{-3}$, resulting from 80 keV Si implant at a dose rate of $5 \times 10^{12}\,\mathrm{cm}^{-2}\mathrm{s}^{-1}$. (a) Implant temperature of -100 °C and dose of $1 \times 10^{13}\,\mathrm{cm}^{-2}$ (b) Implant at room temperature and a dose of $1 \times 10^{14}\,\mathrm{cm}^{-2}$ (c) Implant temperature of 200 °C and dose of $1 \times 10^{15}\,\mathrm{cm}^{-2}$.

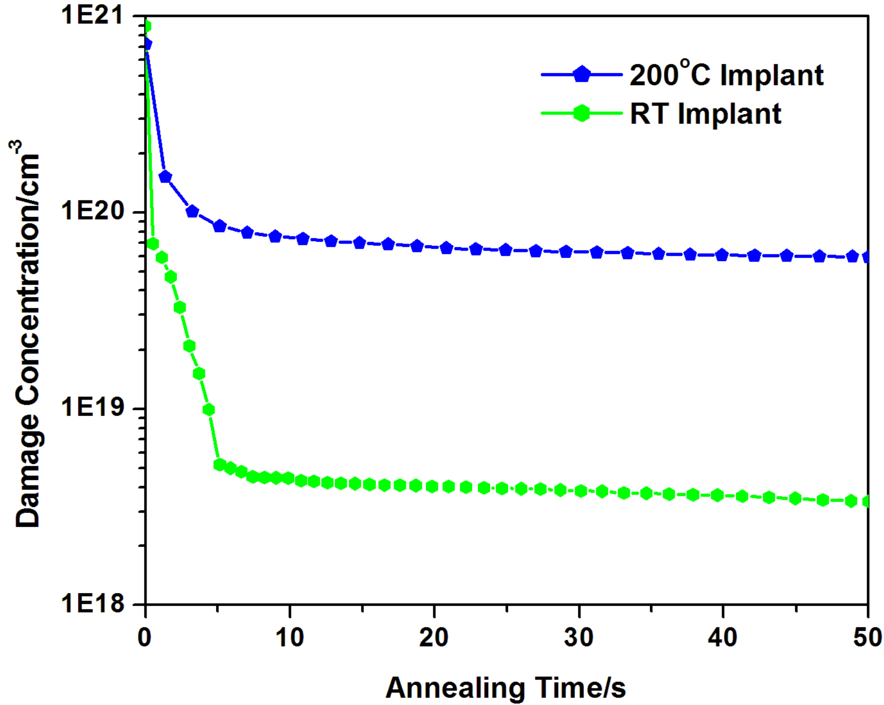

Figure 6.3: Annealing behavior of damage induced by room temperature implant and by 200 °C implant at 800 °C.

The different initial damage morphologies at the same damage concentration were then used as a starting point for subsequent annealing at 800 °C. Figure 6.3 shows the different annealing behavior. The damage induced by room temperature implantation anneals out very quickly compared to the more stable damage induced by the 200 °C implant. During the annealing of the damage induced by the room temperature implant, the sharp initial drop in damage corresponds to the recrystallization of APs. In the next few seconds, the more gradual decrease in damage is the result of emission of I, V clusters, which then undergo recombination or annihilation at the surface. In the case of annealing of the damage induced by the 200 °C implant, the initial slower drop in damage is due to slower I, V point defect emission from the more stable I, V clusters. In both cases, the damage subsequently remains constant due to the more stable {311} defects.

6.4 Conclusions

It is shown that at the same damage level, different implant conditions can lead to different damage morphology, consisting of APs, pure clusters or a mixture of both. Since APs and clusters have different thermal stability, with clusters being more stable and hence more difficult to anneal, the same amount of damage with different morphology, consequently leads to different annealing behavior with interesting practical implications. As the presence of defects is detrimental to device performance, and a minimum thermal budget is required for their complete dissolution, the same amount of damage resulting from different implant conditions would require different thermal budgets.

Chapter 7

Extended Defects Simulations

In addition to having a good damage accumulation model that includes damage kinetics during the implant process, for practical purposes, it is essential to be able to simulate the extended defects evolution as well. This is because extended defects are often formed during the thermal annealing process involved in ultra-shallow junction formation. In this chapter, a model is presented for the transformation of $\{311\}$ defects into dislocation loops, with a transformation rate that is controlled by a size-dependent energy barrier. The model has been included in DADOS, which includes a description of the size distribution of $\{311\}$ defects (required for a size-based model) and of amorphization and recrystallization (needed to provide reliable information on the number of interstitials in the end-of-range region). The model correctly predicts the formation of dislocation loops during the annealing that follows ion implantation, for both amorphizing and non-amorphizing conditions, and provides a realistic description of the damage morphology.

7.1 Introduction

Under certain conditions, particularly for high-dose implants, {311} defects can evolve into dislocation loops [Li and Jones, 1998, Claverie et al., 2000]. This has been observed for both amorphizing [Robertson et al., 2000, Cristiano et al., 2004] and non-amorphizing implants [Li and Jones, 1998]. As dislocation loops are more stable than {311} defects, their transformation entails a strong decrease of the interstitial supersaturation, drastically slowing down TED [Bonafos et al., 1997]. Therefore, for an accurate simulation of the dopant profiles after incomplete anneals, it is crucial to be able to predict whether or not, and when dislocation loops will appear. Moreover, the presence of extended defects in devices would be detrimental for both the reliability and the electrical characteristics and, consequently, it is necessary to estimate the minimum thermal budget to achieve their complete dissolution. This minimum budget depends on whether stable dislocation loops are formed or not. For all these reasons, the accurate modeling of the transformation of {311} defects into dislocation loops can play a key role in current silicon process simulation.

At present, there are good models in literature for describing the behavior of {311} defects in low-dose implants, in which no dislocation loops are produced [Gencer and Dunham, 1997, Hobler and Rafferty, 1999, Claverie et al., 2002]. Some models simulate the growth and ripening of dislocation loops [Lampin et al., 1999] without considering the {311} defects. Concerning the key point of the transformation of {311} defects into dislocation loops, it has been treated in two different ways: one assuming a transformation rate that does not depend on defect size [Avci et al., 2004] and another considering a fixed threshold size for a {311} defect to unfault into dislocation loop [Gencer and Dunham, 2002]. The first one has proved to be able to describe the nucleation and evolution of dislocation loop in amorphizing implants [Avci et al., 2004] but, as no size-dependence is considered,

it would incorrectly predict dislocation loop formation for low-dose implants, in contradiction with experiments [Eaglesham et al., 1994, Cherkashin et al., 2004]. In contrast, the second one can be used for both low and high doses, elucidating whether or not dislocation loops nucleate and correctly describing the overall evolution of the {311} and dislocation loop populations [Gencer and Dunham, 2002]. However, as far as the defect morphology is concerned, transmission electron microscopy (TEM) images show some {311} defects much larger than the critical size used in the model which have not unfaulted yet [Takeda, 1991, Li and Jones, 1998, Li et al., 1998, Calvo et al., 2004, Cherkashin et al., 2004] and suggest that the transformation is not instantaneous, in contrast with the assumptions of that model.

In this chapter, the model uses simultaneously the concepts of size dependence and transformation rate and can, thus, account for the stochastic nature of the {311} defects to dislocation loops transition.

7.2 Model

It is a common experimental observation that {311} defects can reach sizes for which the dislocation loop configuration is energetically more favorable. Indeed, the crossover size (see Fig. 7.1) between the formation energies of {311} defects and dislocation loops can be estimated to be about 300 interstitials [Calvo et al., 2004] (less than 20 nm in length [Eaglesham et al., 1994, Hobler and Rafferty, 1999]), whereas much larger {311} defect sizes, with lengths above 100 nm and containing several thousands of interstitials, can be observed by TEM [Li and Jones, 1998, Li et al., 1998, Calvo et al., 2004, Cherkashin et al., 2004]. This suggests the presence of an energy barrier for the transformation of these metastable {311} defects into dislocation loops. This energy barrier would be larger for small {311} defect sizes since no transformation into dislocation loops is observed for populations of small {311} defects [Eaglesham et al., 1994]. The idea of a thermally activated transformation is also supported by the fact that, for similar sizes, the transformation is more difficult (less frequent) at lower temperatures [Calvo et al., 2004]. From a microscopic point of view, the energy barrier for the transformation reflects the difficulty of rearranging a large extended defect.

In this model, instead of using a fixed threshold size, the transformation rate of metastable {311} defects to dislocation loops would depend on an energy barrier as a function of size. The energy barrier as a function of {311} defect size, represented in Fig. 7.2 [Castrillo et al., 2005], is one of the key points for the development of this model.

The shape of the energy barrier is such that it is high for small interstitials, decreasing gradually to become more stable with an asymptote at $E0$. Mathematically, this energy barrier as a function of the number of interstitials in {311} defects, is in the form of

$$E(y) = E0 + E1\left(\frac{y}{y_o} - 1\right)^{-\gamma} \quad (7.1)$$

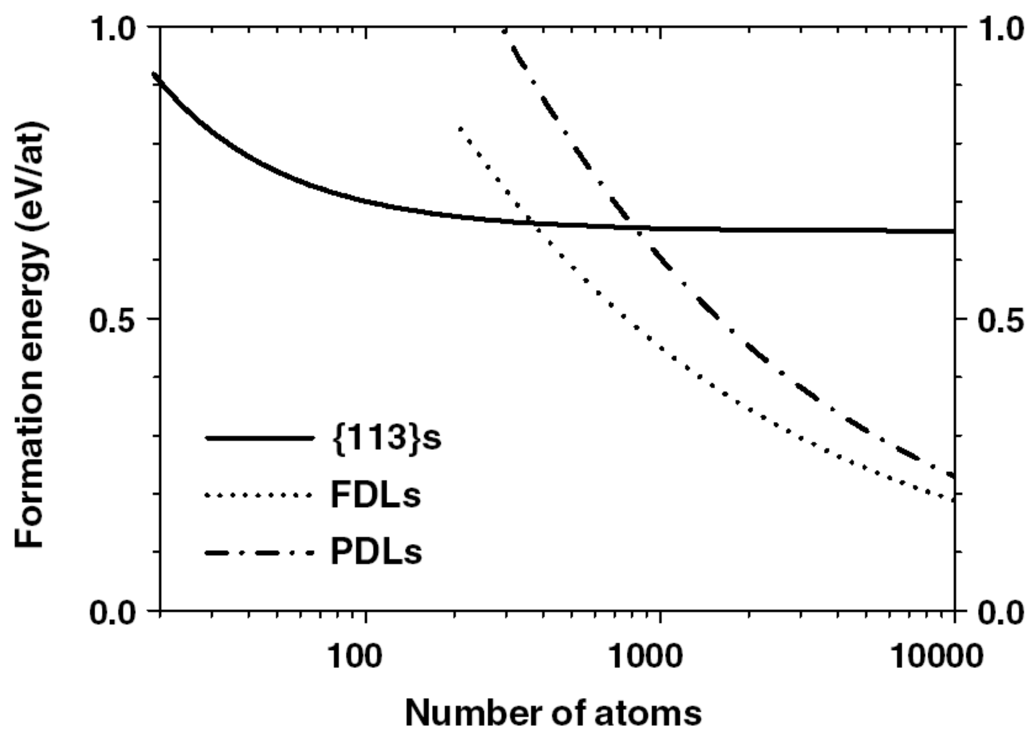

Figure 7.1: Formation energies of the different extrinsic defects as a function of their size from Ref. [Calvo et al., 2004]. FDL: Faulted dislocation loops. PDL: Perfect dislocation loops.

where y is the number of interstitials in {311} defects and y_o is the crossover size between the formation energies of {311} defects and dislocation loops.

Parameter values are shown in Table 7.1 and they are extracted from reference [Li and Jones, 1998] for non-amorphizing condition and are extracted from reference [Robertson et al., 2000] for amorphizing condition. Results will be shown in the following section.

Table 7.1: Parameter values for the transition of {311} defects to dislocation loops.

Parameter	Value
$E0$	3 eV
$E1$	3 eV
γ	2

The transition rate is given by

$$R(y) = R0 \exp \frac{-E(y)}{kT}. \tag{7.2}$$

where *R0*, the prefactor, is the rate in the limit where $E(y) \rightarrow 0$ or T$\rightarrow \infty$. k is the Boltzmann constant and T is the temperature.

This gives a size-dependent transformation rate at 800 °C as shown in Fig. 7.3, where a rate prefactor of $3 \times 10^{11}\,\mathrm{s}^{-1}$ has been used.

In order to illustrate the global effect of size dependence, assume for example, two different populations of {311} defects with size distributions like those of Fig. 7.4, both following log-normal distributions [Pan and Tu, 1997], one with smaller defects (with a mean size of 300 interstitials and a mean length of about 18 nm) and the other with larger defects (with 2500 interstitials and about 75 nm length on average). The products of the rate and the size distributions are shown in Fig. 7.5. The areas under the curves correspond to the total transformation rates, which would be much faster for the case of the larger size population.

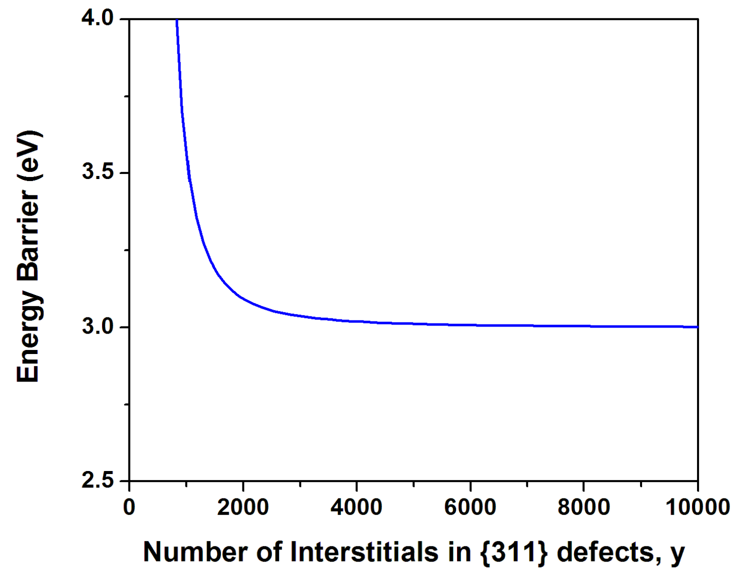

Figure 7.2: Energy barrier for the transformation from {311} defects to dislocation loops as a function of the size (number of interstitials, y) of the {311} defects.

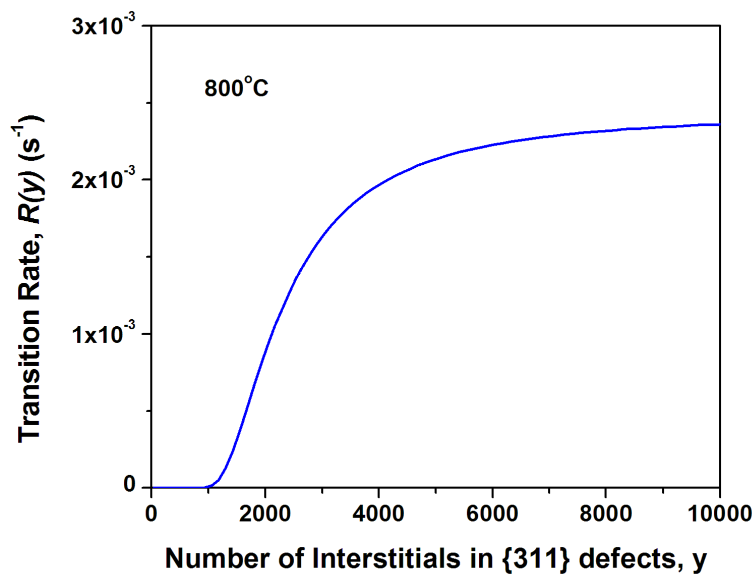

Figure 7.3: The resulting transition rate, $R(y)$, at 800 °C.

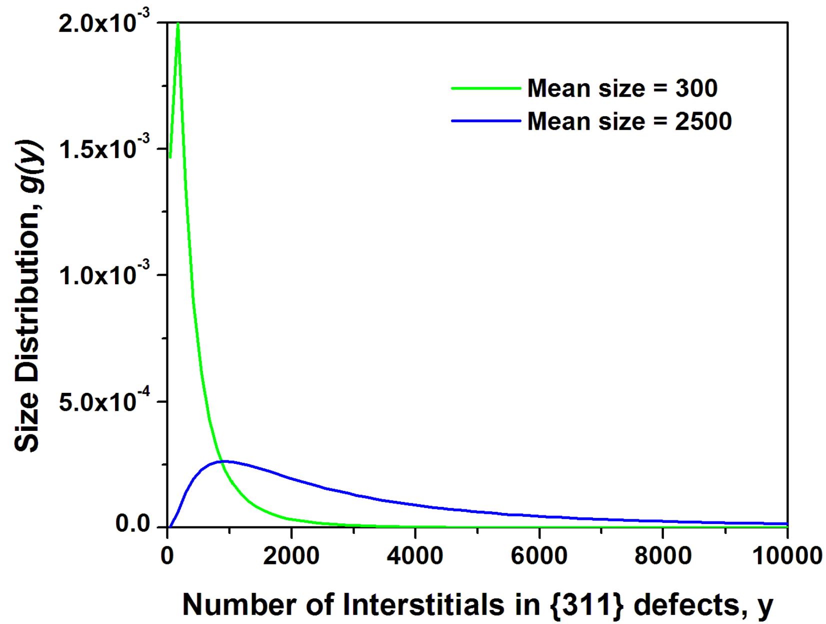

Figure 7.4: Examples of size distribution, $g(y)$ of two different defect populations, with mean size of 300 and mean size of 2500.

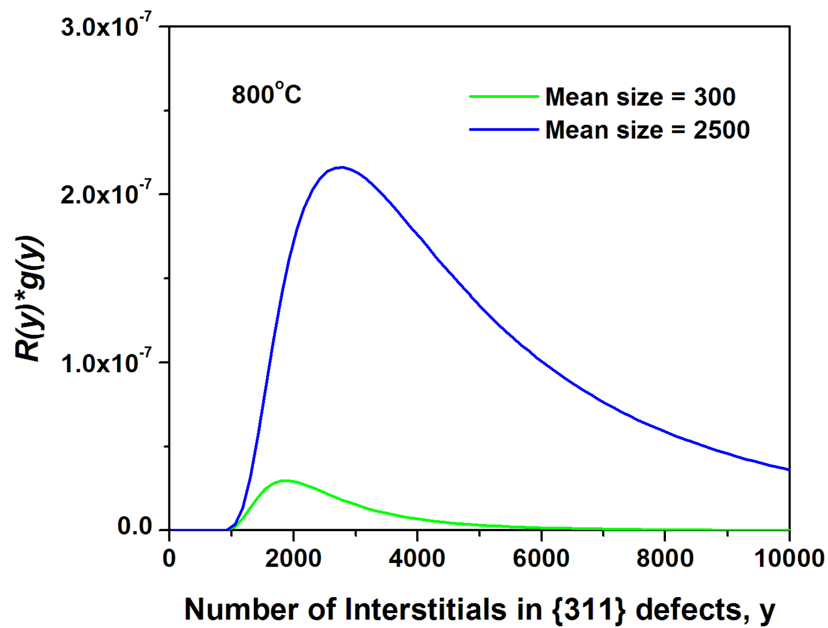

Figure 7.5: Transformation rate as a function of the size of the {311} defects, $R(y) \times g(y)$ at 800 °C.

Extended defects have been implemented according to realistic geometries, giving a direct assessment of the capture volume for diffusing defects. {311} defects have been arranged in any of the 12 equivalent orientations, with the areal density derived from high resolution microscopy (5 interstitials/nm^2) [Takeda, 1991] and with lateral width increasing with length [Hobler and Rafferty, 1999]. In particular, the relationship $W = \sqrt{0.5\,nm \times L}$ was used [Hobler and Rafferty, 1999]. Dislocation loops have been implemented assuming that they are of the faulted type, which is known to be the dominant variety of dislocation loops for diameters less than 80 nm [Cristiano et al., 2000]. Consequently, dislocation loops have been arranged with disk shape in any {111} orientation, with areal density of 15.7 interstitials/nm^2 [Cristiano et al., 2000]. The energetics of dislocation loops have been taken from elastic and dislocation theory [Cristiano et al., 2000] and their emission prefactor has been adjusted to fit the experimental interstitial supersaturation [Bonafos et al., 1997].

7.3 Results

7.3.1 {311} defects

Before showing simulation results of the transformation of {311} defects into dislocation loops, it is essential to first show the correct behavior of the {311} defects. Tests on the simulation of the {311} defects are commonly determined by good fits of their dissolution [Eaglesham et al., 1994, Hobler and Rafferty, 1999] and of the supersaturation they cause [Cowern et al., 1999c] (see Ref. [Jaraiz, 2004]).

The dissolution of the {311} defects was initially observed by Eaglesham et al. [Eaglesham et al., 1994]. In the experiment, Si samples were implanted with 40 keV, $5\times10^{13}\,\mathrm{cm}^{-2}$ Si and subsequently annealed at various temperatures (670 °C, 705 °C, 738 °C and 815 °C) [Stolk et al., 1997]. Figure 7.6 shows the comparison between simulation and the experimental results. As can be seen, the interstitial dissolution from {311} defects depends strongly on temperature.

As a second test, the Si supersaturation was extracted by Cowern et al., based on the transient enhanced diffusion of B marker layers in Si-implanted samples [Cowern et al., 1999c]. In the experiment, B marker layers were implanted with 40 keV, $2\times10^{13}\,\mathrm{cm}^{-2}$ Si and subsequently annealed at 600 °C, 700 °C, 800 °C. Figure 7.7 shows the simulated and experimental interstitial supersaturation as a function of annealing temperature and time.

In agreement with experiments, no transformation of {311} defects into dislocation loops was observed when simulating the low dose implantations of Ref. [Eaglesham et al., 1994, Colombeau et al., 2003, Cherkashin et al., 2004]. Figure 7.8 shows the cross-sectional TEM image [Colombeau et al., 2003], as well as the simulated configuration after 40 keV, $6\times10^{13}\,\mathrm{cm}^{-2}$ Si implantation, followed by annealing for 30 min at 740 °C.

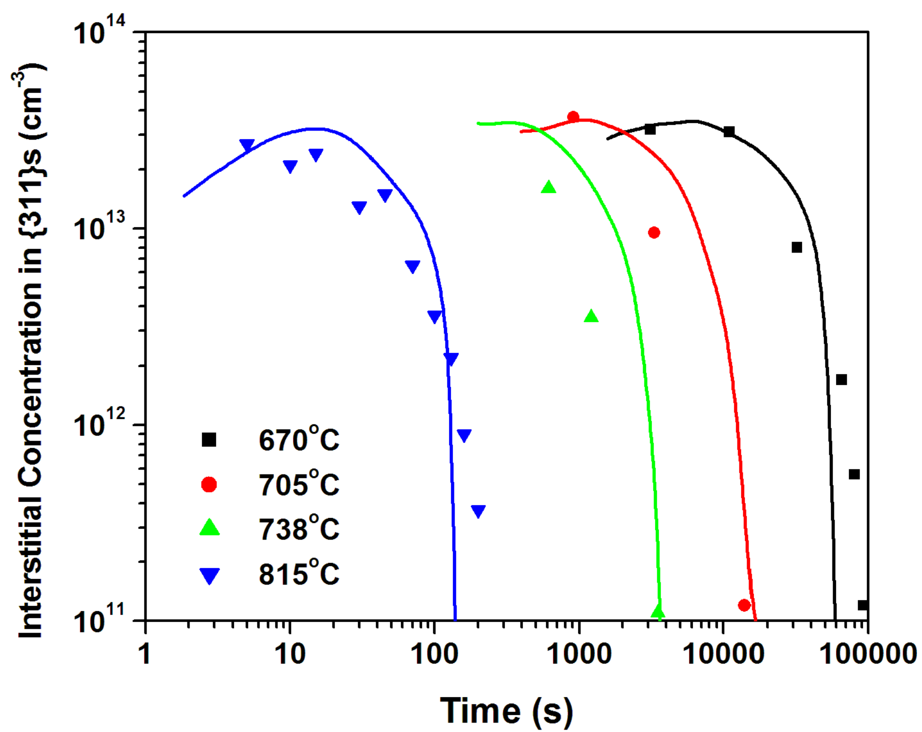

Figure 7.6: Number of interstitials in {311} defects as a function of time at various temperatures after 40 keV, $5 \times 10^{13}\,\mathrm{cm}^{-2}$ Si . Symbols represent experimental data and lines represent simulations. Experimental data is obtained from [Stolk et al., 1997].

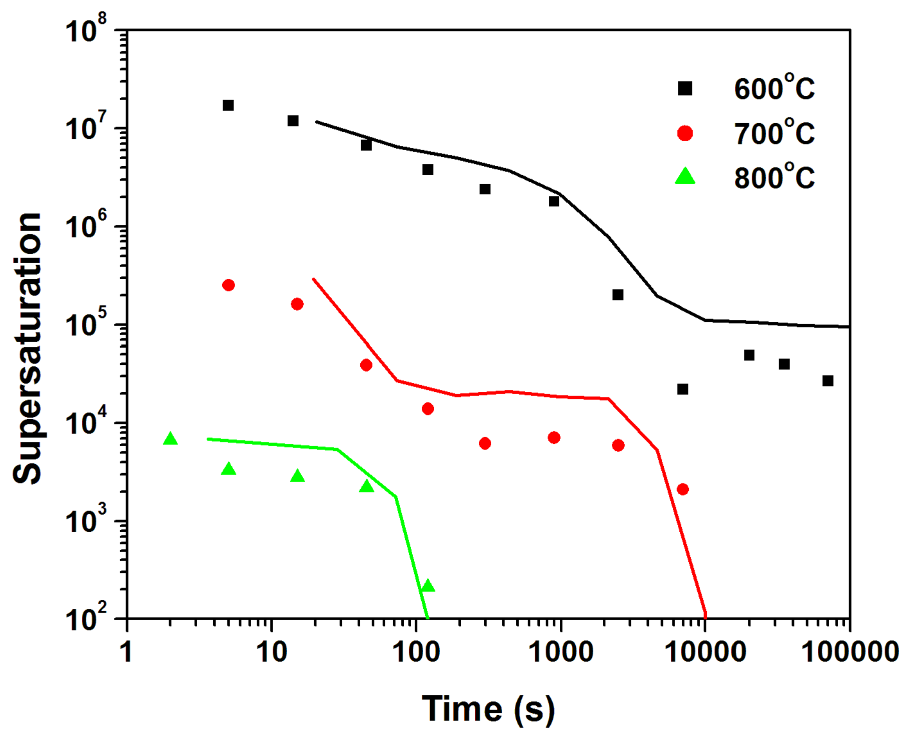

Figure 7.7: Interstitial supersaturation as a function of annealing time at various tempeartures after 40 keV, $2 \times 10^{13}\,\mathrm{cm}^{-2}$ Si implantation. Symbols represent experimental data and lines represent simulations. Experimental data from [Cowern et al., 1999c].

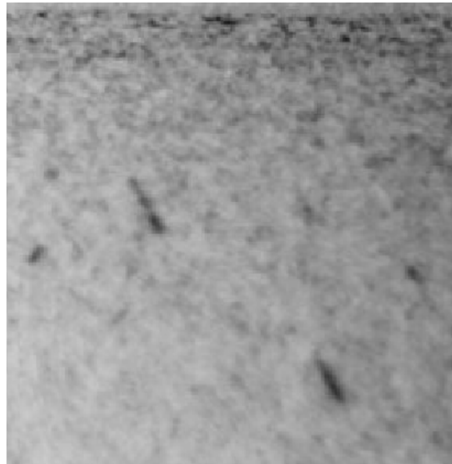

(a)

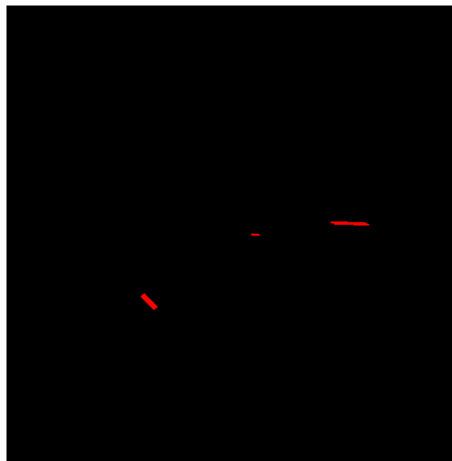

(b)

Figure 7.8: Cross-sectional images showing the damage morphology after 40 keV, $6 \times 10^{13}\,\mathrm{cm}^{-2}$ Si implantation, followed by annealing for 30 min at 740 °C. (a)Experimental image from Ref. [Colombeau et al., 2003]. (b) Simulation from DADOS showing only {311} defects and no dislocation loops. Scale for both (a) and (b): 200 nm × 200 nm.

7.3.2 Non-amorphizing Si implantation

One of the non-amorphizing Si implantations reported in literature corresponds to a room temperature, 100 keV Si^+-implant, with a dose of $2 \times 10^{14}\,cm^2$ and a dose rate of $2.5 \times 10^{13}\,cm^{-2}s^{-1}$, followed by 800 °C anneal [Li and Jones, 1998, Li et al., 1998]. These implant conditions are non-amorphizing, as confirmed by cross-section TEM [Li et al., 1998]. The simulation of the implant process, including dynamic annealing, confirms the lack of a continuous amorphous layer. (See also Fig. 5.7, which shows the proportion of different damage components for a similar implant condition, at a slightly different dose rate.)

During the subsequent annealing, {311} defects were formed and they were observed in situ to evolve into dislocation loops [Li and Jones, 1998]. The experimental time evolution of the interstitials in both types of defects is displayed in Fig. 7.9.

Due to the size of the {311} defects required for the transformation into dislocation loops, as well as to obtain meaningful statistical data of the different types of defects, a large simulation volume with implant area of at least $100\,nm \times 100\,nm$, is required for such simulations.

The simulation results (also shown in the figure) correctly reproduce the transformation timing of {311} defects into dislocation loops. However, the number of interstitials in defects seen by microscopy is only a third of the amount obtained in the simulation, and the simulated curves in the figure have been scaled by this factor. There may be several hypotheses to explain this discrepancy, like interstitial capture by carbon traps, microscopy resolution limitations, but the explanation is not conclusive. It should be pointed out that no simplifying assumptions about the initial damage (like the "+1 model" [Giles, 1991]) have been made in the simulations and the number of interstitials in the extended defects is close to the one interstitial per implanted ion (supporting the validity of the "+1" model for the

present conditions).

Figure 7.10 shows the TEM plan-views and the simulated configurations corresponding to the experiment of Fig. 7.9 after 10 min at 800 °C, taken from Ref. [Li et al., 1998].

A good resemblance is found between the morphology observed by TEM and the simulation. (The "simulated pictures" do not include calculations of the diffraction intensity but only the simulated coordinates of the particles. Therefore, no quantitative comparison with the TEM contrast can be done.) Note that there is not just a "threshold size" for the transformation from {311} defects to dislocation loops, but a size-dependent transformation rate. In addition, {311} defects that have high tilt angle makes them look thinner and shorter. This could be one of the possible reasons for the scaling factor needed in Fig. 7.9.

Simulations performed for the same implant energy and annealing temperature of the experiment of Fig. 7.9, but lowering the dose, indicate that the onset dose for dislocation loop formation is about $10^{14}\,\mathrm{cm}^{-2}$, in agreement with recent experiments [FRENTECH, 2004].

7.3.3 Amorphizing Si implantation

Figure 7.11 represents the time evolution of the extended defects during the annealing that follows an amorphizing Si^{+} implant [Robertson et al., 2000]. The implant energy is 20 keV, the dose and dose rate are $10^{15}\,\mathrm{cm}^{-2}$ and $1.9\times10^{15}\,\mathrm{cm}^{-2}\mathrm{s}^{-1}$, respectively, and the annealing has been performed at 750 °C. Although the conditions are different from the previous case, a good qualitative agreement is observed again between the experimental data and the simulation. In this case, the simulated number of interstitials in defects has been divided by 2 to account for the lower amount of interstitials observed in the experiment compared to the simulation.

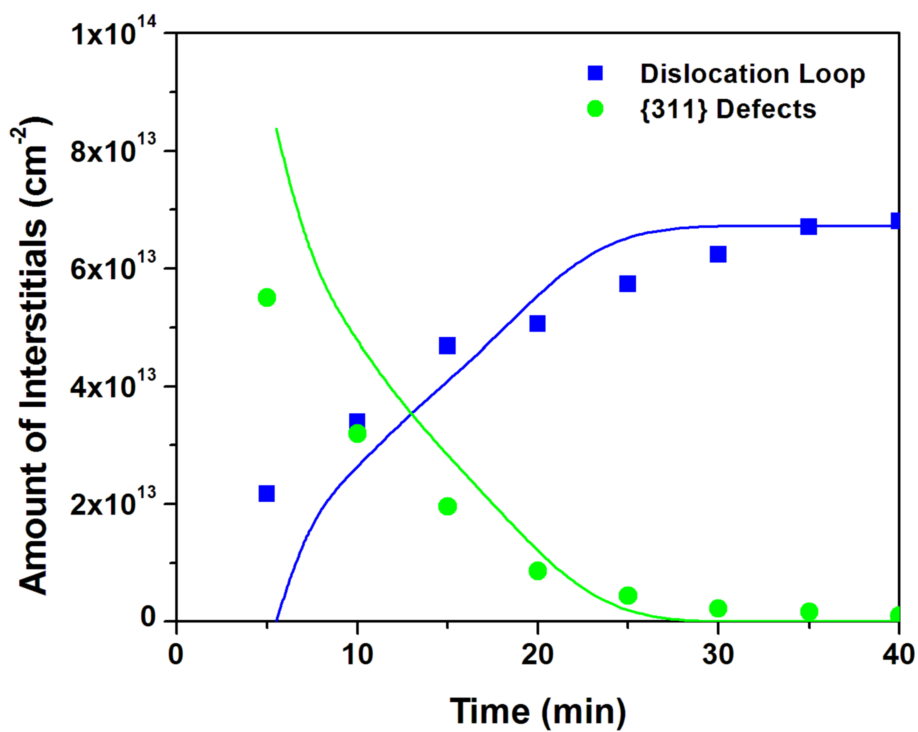

Figure 7.9: Time evolution of the amount of interstitials in extended defects for the 800 °C anneal that follows a non-amorphizing 100 keV, $2 \times 10^{14}\,\mathrm{cm}^{-2}$ Si implant. Symbols represent experimental data from Ref. [Li and Jones, 1998]. Simulation results are plotted as lines and have been divided by 3.

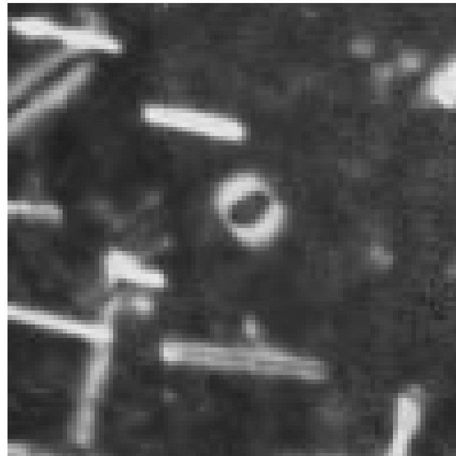

(a)

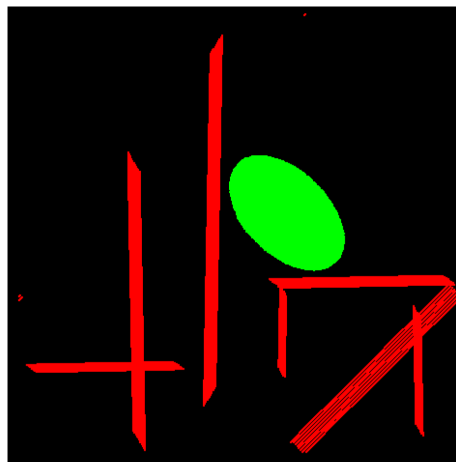

(b)

Figure 7.10: Plan-view of {311} defects and dislocation loops corresponding to the anneal of Fig. 7.9 after 10 minutes. (a) TEM image from Ref. [Li et al., 1998]. (b) Simulated plan-view. Scale for both (a) and (b): 100 nm x 100 nm.

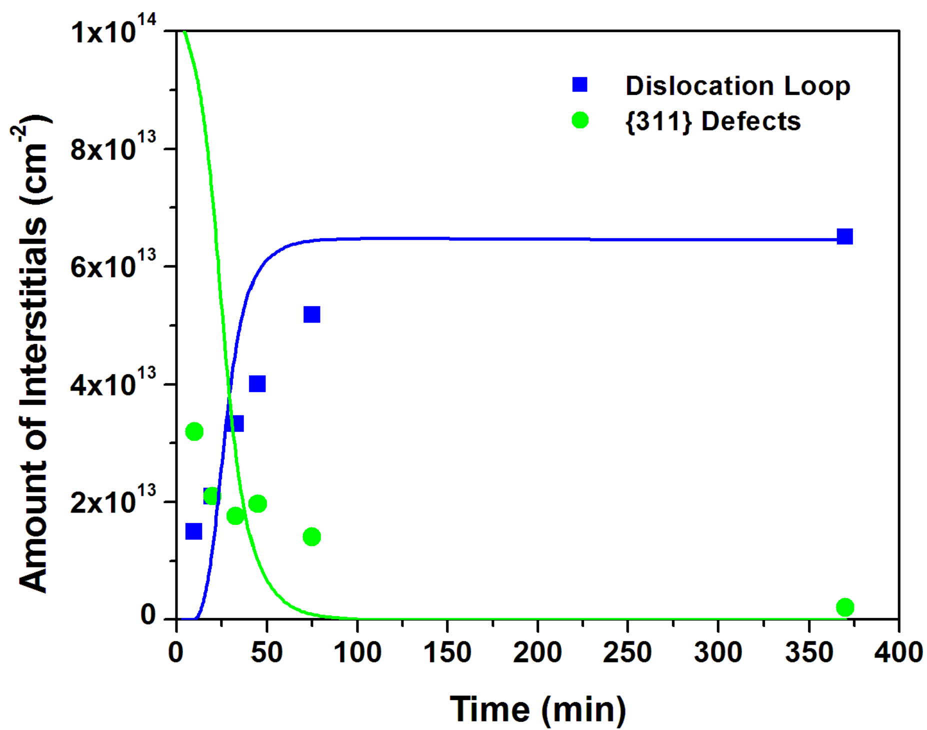

Figure 7.11: Time evolution of the amount of interstitials in extended defects for the 750 °C anneal that follows a Si 20 keV, 1×10^{15} cm^{-2} amorphizing implant. Symbols represent experimental data from Ref. [Robertson et al., 2000]. Simulation results are plotted as lines and have been divided by 2.

7.3.4 Damage Evolution of a Buried Amorphous Layer

Figures 7.12 to 7.15 show the comparison between simulated and experimental damage evolution of a buried amorphous layer.

In the experiment [Pan and Tu, 1997], ion implantation was performed at room temperature, 50 keV, with a high beam current of 8.0 mA, up to a dose of $3.6 \times 10^{14}\,\mathrm{cm}^{-2}$ in order to produce an amorphous surface layer. In addition, a number of rapid thermal anneals (RTA) were carried out at various temperatures and durations.

Figure 7.12 shows the as-implanted damage morphology, with a buried amorphous layer and a very thin surface layer of a few nanometres that is not amorphized.

Figure 7.13 shows the damage morphology after a 1 s, 800 °C anneal. One can clearly observe two interfaces on which defects are formed. The deeper defect interface corresponds to the original amorphous-crystalline interface, while the shallow defect interface is located approximately at the middle of the original amorphous layer. In the simulation, recrystallization takes place simulataneously from the two amorphous-crystalline interfaces of the as-implanted samples. The excess defects that are swept along by the two advancing amorphous-crystalline interfaces cannot be absorbed by a free surface, hence defects appear along the plane where the two interfaces meet.

Figure 7.14 shows the damage morphology after a 60 s, 800 °C anneal. At the deeper amorphous-crystalline interface, the density of defects is higher in the region closer to the original amorphous-crystalline interface. Simulated damage morphology produced similar results. The higher density of {311} defects closer to the original amorphous-crystalline interface is due to the fact that the amount of excess interstitials decreases with increasing depth from the amorphous-crystalline interface. Notice that dislocation loops have not evolved at this point, while the

{311} defects are growing and/or dissolving at the end-of-range.

Figure 7.15 shows the damage morphology after a 120 s, 900 °C anneal. At this stage, only dislocation loops are observed. All {311} defects have either dissolved or transformed into dislocation loops.

The similarities between experimental and simulated damage evolution give confidence in the damage accumulation model, not only in terms of amorphization and recrystallization, but also in terms of {311} defects to dislocation loops transformation.

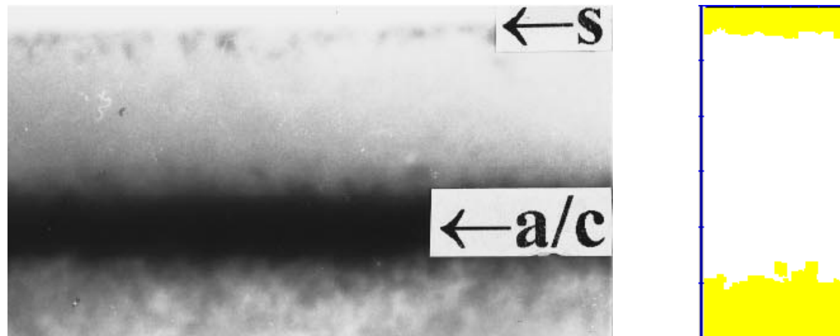

Figure 7.12: Comparison between experimental x-TEM [Pan and Tu, 1997] and simulation for as-implanted samples. Letters s and a/c indicate the implanted surface and the location of the as-implanted amorphous-crystalline interface. The same scale is used for both images, whereby the simulation width is 50 nm. In the simulation, white represents amorphous damage and yellow represents amorphous pockets.

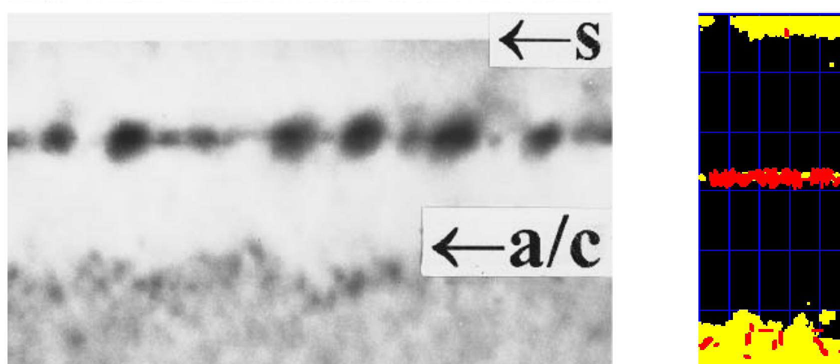

Figure 7.13: Comparison between experimental x-TEM [Pan and Tu, 1997] and simulation after 1 s, 800 °C. In the simulation, yellow represents amorphous pockets and red represents {311} defects.

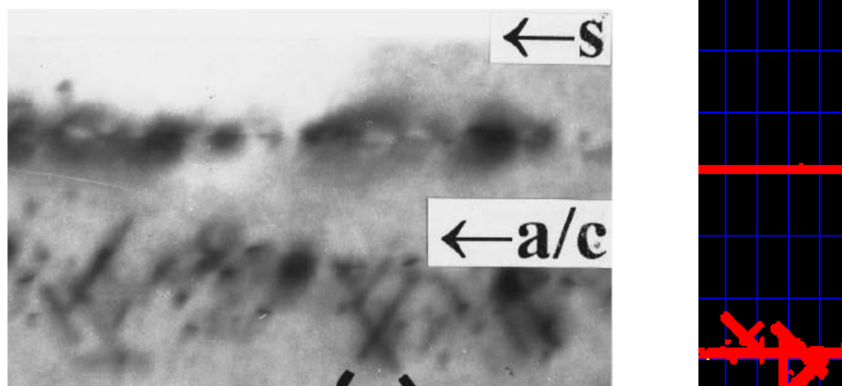

Figure 7.14: Comparison between experimental x-TEM [Pan and Tu, 1997] and simulation after 60 s, 800 °C.

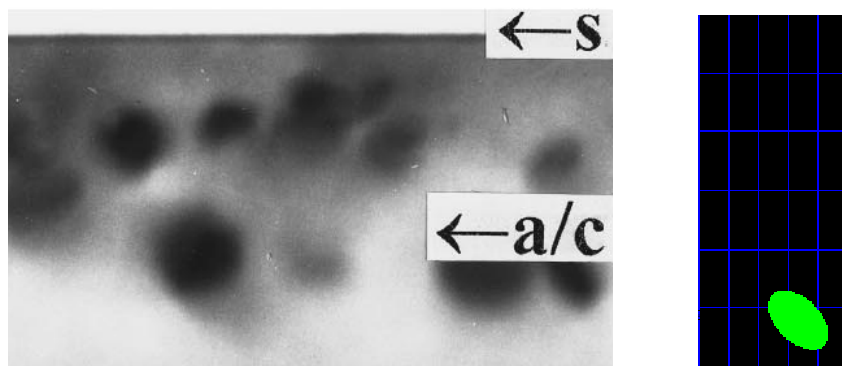

Figure 7.15: Comparison between experimental x-TEM [Pan and Tu, 1997] and simulation after 120 s, 900 °C. A dislocation loop is shown in the simulation.

7.4 Conclusion

In summary, a physically-based model for the transformation of {311} defects into dislocation loops considering a size-dependent energy barrier is presented. The model has been implemented in an atomistic kMC simulator that includes a comprehensive treatment of ion-induced damage evolution and realistic geometries and energetics for extended defects. The model has been tested both for amorphizing and non-amorphizing conditions, and provides a realistic three-dimensional description of damage morphology.

Chapter 8

Influence of SOI Structure on Defects

In an earlier chapter, a damage accumulation model, which accounts for dynamic annealing during the implantation process, was described. Subsequently, it was shown that the model is able to simulate very accurately a number of experimental observations of as-implanted damage with different implantation parameters. Building on that, modeling and simulation of extended defect transformation from {311} defects to dislocation loops was shown. This is essential as the actual processes in ultra-shallow junction (USJ) formation would involve a post-implantation thermal annealing process, whereby extended defects are formed. Finally in this chapter, the damage models that have been described earlier, are involved in simulating the technologically relevant processes in USJ formation. Coupled with dopant-defect interaction and dopant diffusion, simulation results of dopant concentration and activation are in good agreement with experimental data. In addition, with growing interest in the use of silicon-on-insulator (SOI) wafers, the influence of SOI structure on damage evolution and USJ formation is shown.

8.1 Introduction

To achieve the stringent requirements of the International Technology Roadmap for Semiconductors [Semiconductor Industry Association, 2005] in terms of sheet resistance and junction depth, one main method of forming highly-active, ultra-shallow junctions is to implant dopants with ultra-low energy into preamorphized

silicon, followed by a low temperature solid phase epitaxial regrowth (SPER) process. The amorphous silicon reduces dopant channeling, resulting in abrupt, shallow profiles, while SPER at low temperature, allows only slight diffusion and incorporates dopant atoms into substitutional lattice sites at metastably high concentrations above the equilibrium solid solubility limit [Tsai and Streetman, 1979]. This technique has been shown to be capable of forming USJ with junction characteristics in terms of depth, abruptness and sheet resistance, that meet the transistor requirements for the 65 nm and 45 nm CMOS nodes [Pawlak et al., 2002, Lindsay et al., 2004]. In addition, this is an attractive technique as it is compatible with current manufacturing capabilities, requiring only conventional implant and thermal processing equipment.

Besides forming USJ on conventional bulk Si wafers, the use of SOI is increasingly popular. In fact, SOI appears to be a potential replacement for bulk Si wafers in future CMOS technology due to the many inherent advantages that SOI wafers possess. The role of SOI is to electrically insulate a thin layer of crystalline Si from the rest of the wafer, for example, by having an oxide layer. The layer of insulation enables SOI-based integrated circuits to function at higher speeds, while reducing electrical losses. The result is an increase in performance and a reduction in power consumption. Other advantages include reduced latch-up, improved radiation hardness and higher operating temperatures [Corlinge, 2004].

With B, differences in B electrical activation and damage evolution could be expected in SOI [Saavedra et al., 2004], in the presence of a buried oxide (BOX) layer. This is due to the role of Si/BOX interface as point defect sinks and the direct correlation between B deactivation and interstitial defect dissolution from the end-of-range (EOR) defects [Colombeau et al., 2004, Pawlak et al., 2004, Aboy et al., 2005, Hamilton et al., 2005]. In fact, it has been shown experimentally that a Si/BOX interface can improve dopant activation [Hamilton et al., 2005]. However, the extent of improvement depends on the location of the EOR damage

with respect to the Si/BOX interface, which is in turn determined by the preamorphization condition and the depth of the Si/BOX interface in the SOI wafers used. In order to optimize the process conditions to achieve desirable junction characteristics, it is important to have reliable predictive models to simulate the SPER process and dopant electrical activity in preamorphized silicon in both bulk silicon and SOI.

To achieve this, it is necessary to have a good model for amorphization and recrystallization [Mok et al., 2005], which will be needed to provide reliable information on the number of interstitials in the EOR region in amorphizing conditions. In addition, it is crucial to correctly model the transition of extended defects in the EOR, from {311}s to dislocation loops [Castrillo et al., 2005]. Due to the difference in interstitial supersaturation of these extended defects, and the fact that B deactivation is driven by the interstitials released from the EOR, one needs to correctly predict whether or not, and when, the dislocation loops appear, as this will affect the simulation of dopant electrical activation, as well as the dopant concentration.

Furthermore, the capability to predict sheet resistance is important in process modeling, as it permits the estimation of the source and drain resistances, which are the limiting factors in performance of MOS devices. ITRS 2005 states that

> An optimum trade-off between minimized dopant diffusion and sufficient (maximized) dopant activation is the key for the formation of shallow junction and low device access resistance. Improved physical understanding of the related mechanisms is therefore directly important for technology development and also the prerequisite for any work on physical modeling.

In this chapter, modeling and simulation was done for the process of USJ formation by SPER, showing the evolution of the implantation-induced damage, the deactivation and reactivation of boron during isochronal thermal anneals at vari-

ous temperatures after SPER. In addition, the influence of the presence of a buried oxide, as in the case of SOI wafers, is shown.

The kMC simulator, DADOS, was used to model the different mechanisms involved in the process of USJ formation, including amorphization, recrystallization, defect interaction and evolution, as well as dopant-defect interaction. During the recrystallization of an amorphous layer in the presence of dopants, like B, B is deposited as active up to a concentration of $2 \times 10^{20}\,\mathrm{cm}^{-3}$ [Pawlak et al., 2004]. The remaining B atoms form small, immobile electrically inactive clusters, B_3I [Mattoni and Colombo, 2004]. In the non-amorphized region, interstitials and vacancies recombine, leaving a band of excess interstitials just below the amorphous-crystalline interface. With increasing annealing temperatures, the EOR defects evolve into increasingly stable defects by the Ostwald ripening process, from small interstitial clusters to {311} defects and into dislocation loops, which eventually dissolve. During the defect evolution and dissolution, the interstitial point defects released from these extended defects at the EOR may diffuse to the B-rich surface to form boron interstitial clusters, thereby deactivating the B, and they may lead to transient enhanced diffusion (TED). Otherwise, they may be lost to sinks, such as the surface [Lim et al., 1995] or the Si/BOX interface.

In the simulations shown, the Si/BOX interface was modeled as a perfect sink for the interstitial point defects. SOI wafers were simulated by changing the material from silicon to oxide at depths more than 55 nm, following the structure of the experimental SOI wafers, essentially creating an Si/BOX interface at 55 nm.

8.2 Results

The following experiments were considered [Hamilton et al., 2005]. Bulk silicon and SOI samples were preamorphized by Ge implanted at 8 or 20 keV at a dose of 1×10^{15} cm^{-2}, followed by 500 eV B at a dose of 2×10^{15} cm^{-2}. This was followed by an isochronal (60 s) anneal in the temperature range of 700 to 1000 °C. Simulations were performed in accordance with the experimental procedures, and simulated results of damage evolution are in good agreement with experimental observations. Since the dissolution of interstitial point defects from the EOR is the source of dopant (B) deactivation and B TED, the damage evolution in the simulation has to be accurate, in order to provide validity to the subsequent results on dopant concentration profile and dopant electrical activation.

8.2.1 Damage evolution

Figure 8.1 shows the as-implanted damage (interstitial) concentration profile following an 8 or 20 keV Ge implant and a 500 eV B implant. The amorphous depths are close to the 20 and 40 nm respectively determined experimentally by Rutherford Backscattering Spectrometry [Hamilton et al., 2005]. Figures 8.2 and 8.3 show 80 nm x 80 nm simulated plan views of defects. Evolution of the EOR defects in the case of the 20 keV Ge PAI in bulk silicon is shown in Fig. 8.2 and in SOI is shown in Fig. 8.3. In bulk silicon, after 60 s anneal at 700 °C, the EOR damage is in the form of small interstitial clusters and {311} defects. At 800 °C, the EOR damage consists of {311} defects and some dislocation loops. This is consistent with transmission electron microscopy analysis of similar experimental condition (with 30 keV Ge PAI instead) [Cristiano et al., 2004]. In bulk silicon, after 60 s anneal at 900 °C, the EOR damage is in the form of dislocation loops only. In contrast, in SOI, there is less damage in all cases and damage does not nucleate into dislocation loops. Furthermore, in SOI, after 60 s anneal at 900 °C,

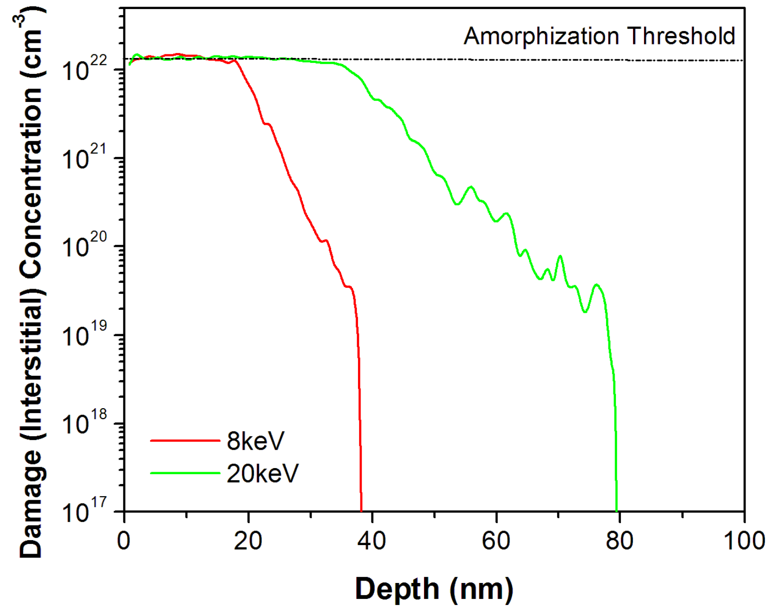

Figure 8.1: Simulated damage (interstitial) concentration profile of as-implanted 8 and 20 keV Ge, followed by 500 eV B. The saturated ($\approx 1 \times 10^{22}\,\mathrm{cm}^{-3}$) level corresponds to amorphized material.

the EOR damage has completely dissolved.

8.2.2 Dopant Concentration Profile

Figure 8.4 shows the B concentration profiles for the 20 keV Ge PAI case after a 60 s, 850 °C anneal in bulk silicon and SOI. The simulated B profiles are able to reproduce the "kink" in the experimental B profiles [Hamilton et al., 2005]. The impact of a buried oxide layer in the SOI case can be clearly seen. Experimentally, the secondary ion mass spectrometry (SIMS) for the B profile in the bulk silicon case (Fig. 8.4a) shows a peak in the tail of the boron profile at the EOR defect region. This peak corresponds to trapped B due to their interaction with EOR defects, like dislocation loops [Chao et al., 1997]. However, this peak is not seen in the corresponding SOI sample (Fig. 8.4b). This may imply that EOR defects did not nucleate dislocation loops in the SOI case by the same thermal budget. In

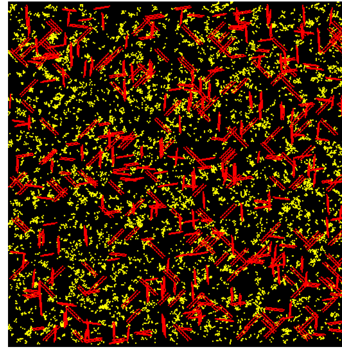

(a)

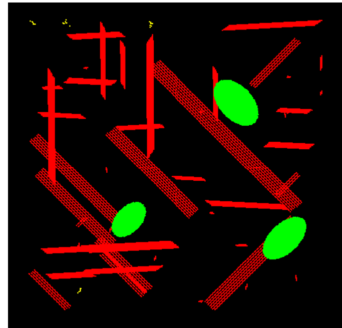

(b)

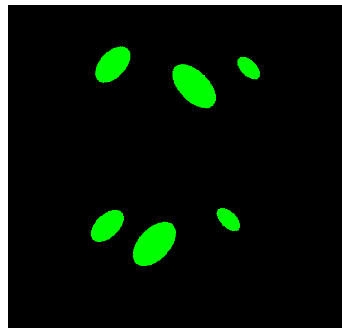

(c)

Figure 8.2: Simulated plan-view of defects in bulk Si corresponding to 60 s anneal at (a) 700 °C (b) 800 °C (c) 900 °C of damage induced by 20 keV Ge preamorphization implant at a dose of 1×10^{15} cm^{-2}, followed by 500 eV B at a dose of 2×10^{15} cm^{-2}. Scale: 80 nm x 80 nm. Yellow represents APs, red represents {311} defects and green represents dislocation loops.

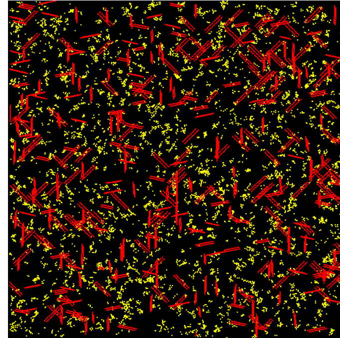

(a)

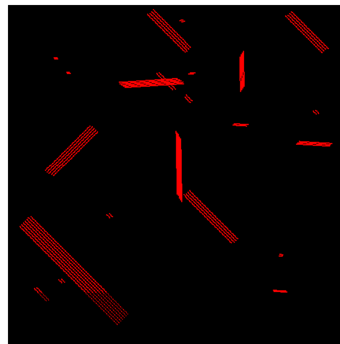

(b)

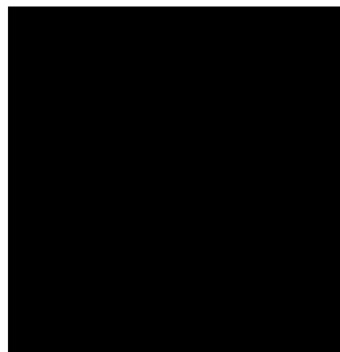

(c)

Figure 8.3: Simulated plan-view of defects in SOI corresponding to 60 s anneal at (a) 700 °C (b) 800 °C (c) 900 °C of damage induced by 20 keV Ge preamorphization implant at a dose of $1 \times 10^{15}\,\mathrm{cm}^{-2}$, followed by 500 eV B at a dose of $2 \times 10^{15}\,\mathrm{cm}^{-2}$. Scale: 80 nm x 80 nm. Yellow represents APs, red represents {311} defects and green represents dislocation loops.

the bulk silicon case, simulation shows that interstitial damage (dislocation loops) remains in the same location as the peak in the experimental B profile. In the corresponding case of the SOI sample, no defect is present in the EOR region from the simulation. In all cases, for the same anneal temperature, less defects (interstitials) remain in the EOR in the SOI case than in the bulk silicon case. This can be explained by the presence of the buried oxide layer, providing an additional mode for the removal of the EOR defects.

8.2.3 Sheet Resistance

A detailed understanding of the process can be obtained from the simulations of the dopant concentration profile, the type and amount of damage remaining and the level of dopant activation. Dopant activation is given by the sheet resistance, which is calculated by

$$R_s = \frac{1}{q\int_0^{x_j} \mu(x) C_B(x) dx} \tag{8.1}$$

where x_j is the junction depth, C_B(x) the carrier concentration, $\mu(x)$ the concentration dependent hole mobility [Caughey and Thomas, 1967], and q the electronic charge. Refer to the Appendix for calculation of the sheet resistance.

Figure 8.5 shows the variation in sheet resistance as a function of annealing temperature. For both the 8 keV and 20 keV Ge PAI, dopant deactivation is observed as sheet resistance increases with annealing temperature, up to a maximum, before dopant reactivation occurs, with sheet resistance rapidly decreasing to very low values.

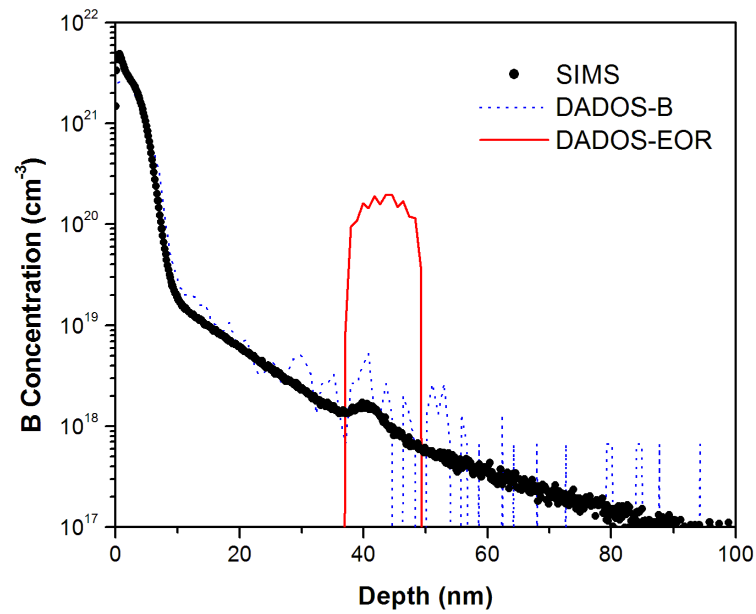

(a)

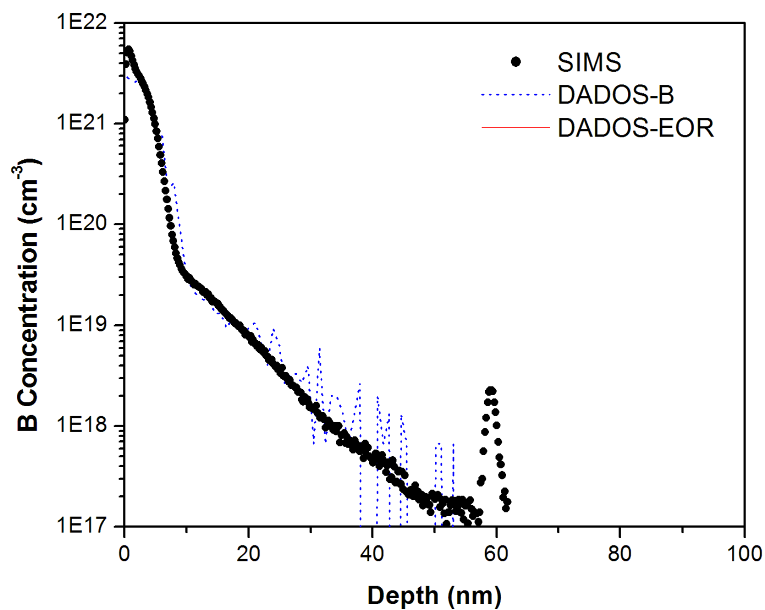

(b)

Figure 8.4: B concentration profile for 20 keV Ge PAI samples after 60 s, 850 °C anneal in (a) Bulk Si (b) SOI. Experimental SIMS obtained from Ref. [Hamilton et al., 2005]

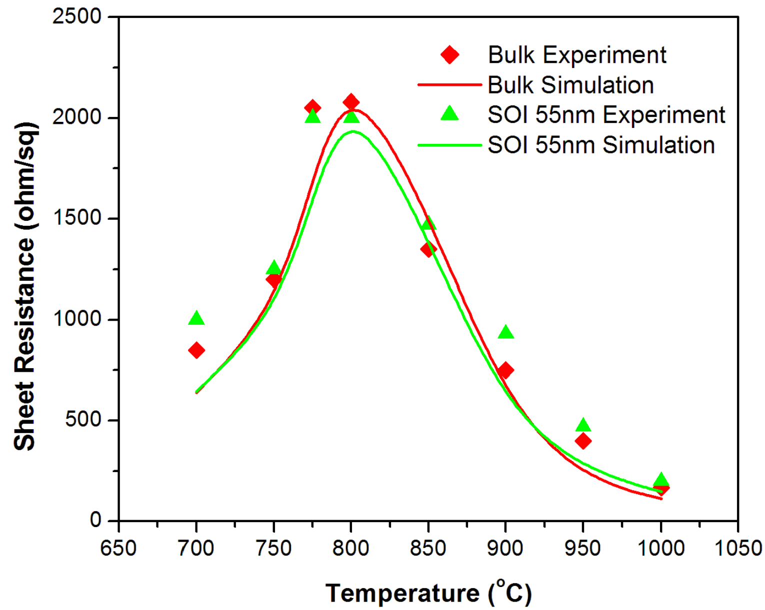

(a)

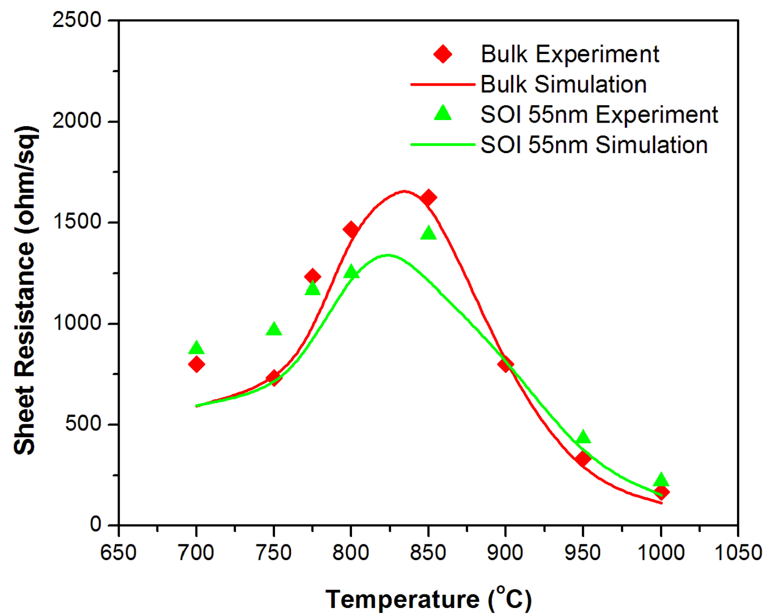

(b)

Figure 8.5: Sheet resistance as a function of annealing temperature, after 60 s isochronal anneal. (a) 8 keV Ge PAI (b) 20 keV Ge PAI. Experimental points from Ref. [Hamilton et al., 2005]

8.3 Discussion

The initial rise in sheet resistance (dopant deactivation) occurs during the ripening of EOR defects. The release of the free interstitial point defects from the EOR, diffuse towards the B-rich surface, forming boron interstitial clusters, deactivating B in the process. The subsequent decrease in sheet resistance (dopant reactivation) is mainly related to the dissolution of the boron interstitial clusters.

In the 8 keV Ge PAI case, the difference between the maximum deactivation in bulk silicon and SOI is small. This is due to the fact that the buried oxide interface is far from the EOR defects and the "sink" effect of the oxide surface is not significant. In the 20 keV Ge PAI case, in agreement with experimental results, the maximum sheet resistance in the SOI case is lower than the corresponding bulk silicon case, implying that B deactivates less in SOI. The higher electrical activation in the SOI case is due to the lower amount of interstitials in the SOI sample compared to the bulk silicon sample, consistent with Fig. 8.4.

The slight disagreement between the calculated and experimental values of sheet resistance for low temperatures in Fig. 8.5 could be related to damage effects. In fact, damage-related mobility decrease and deep-level compensation have not been taken into account for the sheet resistance calculations and they are expected to increase the sheet resistance in the case of (incomplete) low temperature anneals. In addition, the overestimation in the difference between the simulated sheet resistance for the bulk Si and SOI case (Fig. 8.5(b), 850 °C) could be the result of assuming the oxide interface as a perfect sink, which may in fact be a partial sink for interstitial point defects.

It is difficult to conclude from the sheet resistance results and the SIMS if the reduced amount of defects in SOI wafer is due to the buried oxide layer acting as a sink for the free interstitial point defects or if there is intrinsically less interstitial defects to begin with in the SOI wafer, as a portion of the as-implanted damage

induced by 20 keV Ge PAI case is trapped in the buried oxide (at 55 nm), as can be seen in the simulated profile in Fig. 8.1. The latter reason could be likely in light of the experimental Hall sheet resistance results for 8 keV Ge PAI, which shows little difference between the bulk silicon and SOI samples.

To get a better understanding, a test simulation was done using the 20 keV Ge PAI condition, with the buried oxide layer at 80 nm, instead of 55 nm. As one can see from Fig. 8.1, placing the oxide interface at 80 nm would not remove the as-implanted damage initially and at the same time, would act as a "sink" close enough to the EOR defects. Based on simulation of 20 keV Ge PAI condition, followed by a 60 s, 850 °C anneal (corresponding to the condition of Fig. 8.4), the EOR damage was also completely annealed out (not shown), implying that the buried oxide interface acting as an interstitial sink, could affect damage evolution and the remaining EOR. Furthermore, values of sheet resistance in this case are intermediate between the bulk Si case and the case where the buried oxide layer is at 55 nm (not shown).

The amount of EOR damage remaining would affect B profile, since B diffuses via interstitials. Two-dimensional views of a simulated source-drain extension formed in bulk Si and SOI (55 nm) is shown in Fig. 8.6. This provides better visualization of the dopant profile, where the lateral diffusion is particularly important for the source-drain extension, as excessive diffusion under the gate would lead to degraded performance. Figure 8.6(a) is simulated with a 750 °C anneal for 5 min, while Fig. 8.6(b) is simulated with a spike anneal up to 1050 °C.

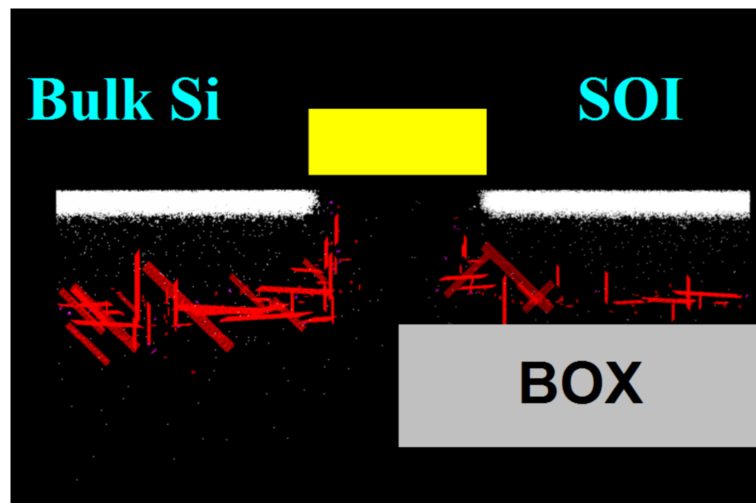

(a)

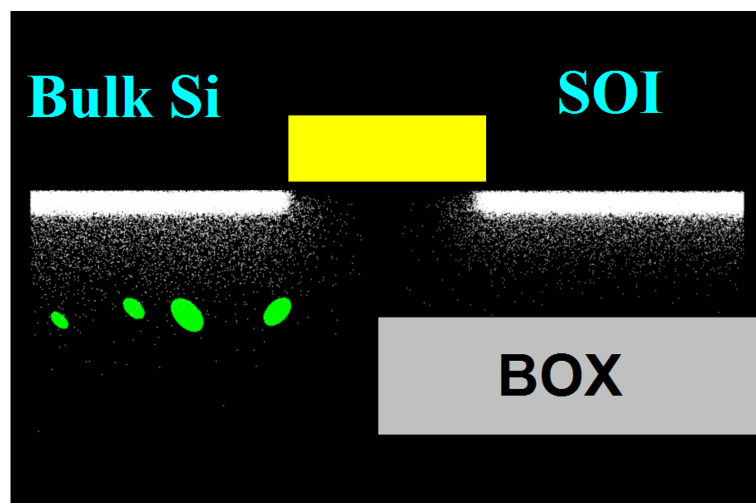

(b)

Figure 8.6: Two-dimensional view of a simulated source-drain extension formed in bulk Si and SOI (55 nm) with 20 keV $1 \times 10^{15}\,\text{cm}^{-2}$ Ge PAI, followed by 500 eV $2 \times 10^{15}\,\text{cm}^{-2}$ B. (a) 750 °C anneal for 5 min (b) spike anneal up to 1050 °C. (White represents B.)

8.4 Conclusion

Dopant concentration profile, activation and reactivation have been simulated in both bulk silicon and SOI, in an USJ formation process by the Ge PAI and SPER technique. Less defects remain in the EOR in the SOI case compared to the bulk Si case, which leads to less dopant deactivation in SOI. It is found that the position of the oxide interface affects damage remaining in the EOR and dopant activation, as it acts not only as a sink for the EOR defects, but also traps part of the as-implanted damage. The good agreement between simulation results and experimental data shows that the simulations are predictive and can provide valuable insights for optimizing processes in bulk Si and SOI.

Chapter 9

Conclusion

Most important and challenging in the area of silicon front-end process modeling is the modeling of ultra-shallow junction formation. The typical physical processes involved, include pre-amorphization implants (PAI), solid phase epitaxial regrowth (SPER) and thermal annealing. These processes affect dopant diffusion and activation. Ion implantation induced damage accumulation is crucial to the simulation of silicon front-end processing. However, difficulties arise due to the complex variety of damage induced by ion implantation. Furthermore, there are many interdependent implantation parameters, like implant species, dose, dose rate and substrate temperature, which would affect the kinetics of damage accumulation.

9.1 Summary of work

In this thesis, a damage accumulation model making use of defect structures known as the amorphous pockets, has been developed to simulate the damage evolution from point defects to a continuous amorphous layer, taking into account dynamic annealing during implantation.

Although the amorphous pocket recombination rate is only size dependent and does not take into account internal spatial configuration of the amorphous pocket, in order to model damage accumulation taking into account the ion mass effect, it is essential to preserve the interstitial, vacancy spatial correlation in the collision cascades to form the initial amorphous pockets with a size distribution dependent on implant ion mass.

The model parameters are obtained from experimental amorphous-crystalline transition temperatures for a range of implanted ions (C to Xe) to reproduce the experimentally observed dose rate effects. A fixed amorphization threshold has been established except for noble gas atoms, whereby the amorphization threshold was found to be lower than expected. In addition, the thicknesses of the amorphous layers are well simulated in a range of amorphizing conditions. The amorphous layer thickness is the direct result of dynamic annealing (recrystallization of APs), using a constant amorphization threshold. In terms of the dose effect, the proportion of amorphous pockets and amorphous regions has been reproduced as a function of dose. The two-layered damage distribution along the path of a high-energy ion has also been simulated, as is consistent with experimental observations. Furthermore, this model is able to show that dynamic annealing is more effective at removing damage than post-cryogenic implantation annealing at the same temperature, as amorphous pockets are allowed to grow to larger (thus more stable) sizes during cryogenic implantation than is allowed by dynamic annealing.

A similar study with different implant conditions shows that at the same damage level, different implant conditions can lead to different damage morphology, consisting of amorphous pockets, pure clusters or a mixture of both. Since APs and clusters have different thermal stability, with clusters being more stable and hence more difficult to anneal, the same amount of damage with different morphology consequently leads to different annealing behavior with interesting practical implications.

An important aspect of damage evolution involves the transformation of extended defects from {311} defects to dislocation loops. Based on a size-dependent energy barrier, the transformation model has been successfully tested against experimental data, providing realistic three-dimensional description of the damage morphology. Furthermore, damage evolution of a buried amorphous layer has been well-reproduced after thermal annealing at various conditions.

Finally, it has been shown that the damage model developed in this work can be successfully used in technologically relevant processes involved in the formation of ultra-shallow junctions. Dopant concentration, activation and reactivation calculated in terms of sheet resistance, have been simulated in both bulk silicon and SOI, in an ultra-shallow junction formation process by the Ge PAI and SPER technique. Less defects remain in the EOR in the SOI case compared to the bulk Si case, which leads to less dopant deactivation in SOI. It was found that the position of the oxide interface affects damage remaining in the EOR and dopant activation, as it acts not only as a sink for the EOR defects, but also traps part of the as-implanted damage.

The good agreement between simulation results and various experimental data shows that the simulations can be predictive and can be used in design and process optimization.

9.2 Recommendations for future work

Although the damage model presented in this thesis is able to simulate reasonably well in a wide range of ion implantation conditions, there are some conditions where more work needs to be done in order to accurately reproduce the expected experimental results.

9.2.1 Effect of dopant atoms on damage

The effect of ion mass on damage accumulation has been addressed in this thesis. For the same implant energy, a larger fraction of the incident energy is used in nuclear collisions in the case of higher mass ions, thus causing more atomic displacements. The differences come not only from the amount of generated defects, but also the morphology of the generated damage, in terms of the amorphous pockets' sizes, as shown in Chapter 4. However, distinct behavior of damage accumulation has been observed by different species of similar ion masses. For example, difference in damage accumulation has been observed for C and B, Si and P, and As and Ge.

Experimentally measured dependence of damage level with dose for 80 keV implantation at room temperature shows that the amorphizing dose for B (11 u) is about $3\times10^{16}\,\text{cm}^{-2}$, but for C (12 u), it is an order of magnitude less at $3\times10^{15}\,\text{cm}^{-2}$ [Baranova et al., 1973].

Moreover, it has been observed that doping strongly influences damage induced by subsequent implantation [Battaglia et al., 1991, Campisano et al., 1993]. The role of dopants in the ion implantation induced amorphization of doped crystalline silicon showed that damage induced by Ge is retarded by B, but enhanced by As [Campisano et al., 1993]. Like B, P-doped samples have been observed to retard damage induced by Au implantation [Battaglia et al., 1991].

Dopants affect not only damage accumulation leading to amorphization, but

also SPER. Common dopants (B, P, As) dissolved in amorphous layer can enhance SPER rate, while compound-forming ones like C, N and O decrease the SPER rate [Priolo et al., 1990b, Kennedy et al., 1977, Csepregi et al., 1977]. In addition, the combination of $n-$ and $p-$type dopants has been shown to produce compensating effects in SPER of Si [Lietoila et al., 1982, Suni et al., 1982].

More work can be done to understand the underlying mechanisms that lead to the differences observed, so that better models and/or parameters can be used to simulate the expected experimental results.

9.2.2 Effect of stress on damage

Although the model that is presented for the formation of dislocation loops seems to be applicable in a wide range of conditions, there are some extreme situations in which the underlying phenomenology may be substantially different. In particular, no {311} defect formation but direct dislocation loop nucleation can occur for very shallow (5 keV) Ge^+ implants [Gutierrez et al., 2001]. This different behavior could be related to the effect of stress, induced by high-defect density and affected by surface proximity. In fact, stress is expected to modify the energetics of extended defects, affecting both the crossover-size of formation energies of {311} defects and dislocation loops and the energy barrier for the transformation between them. In addition, the emission rates and, therefore, the ripening and dissolution rates might also be affected. A coherent stress assessment should include the reciprocal influence between the stress field and the exteneded defects: the stress would modify the energetics of extended defects and conversely the extended defects would produce a local stress field.

In addition to stress, chemical effects related to the Ge fraction in relaxed SiGe alloys have been reported to modify both the extended defect dissolution and the dislocation loop nucleation path. It has been observed that SiGe samples with $\leq 5\,\%$ Ge exhibited {311} defects formation and dissolution, while samples with

Ge fraction $\geq 25\,\%$ showed only dislocation loops formation. Furthermore, dislocation loops formation was observed to increase with increasing Ge concentration [Crosby et al., 2003]. These effects on the extended defects evolution should be further investigated and modeled.

9.2.3 Effect of SOI on damage accumulation

Chapter 8 shows accurate simulation of dopant concentration profile and dopant activation in both bulk Si and SOI, in an ultra-shallow junction formation process. A physical quantitative understanding of the role of the Si/buried oxide(BOX) interface in reducing the amount of end-of-range damage can be obtained by varying the depth of the Si/BOX interface and the Ge pre-amorphizing condition both experimentally and from simulations. From simulations, based on the amount of damage (interstitials) remaining after each anneal, it is possible to obtain quantitative understanding of the contribution of different factors, like the initial amount of interstitials initially trapped (or "truncated") by the BOX layer and the effect of the Si/BOX interface as a interstitial sink at various depths, and whether it is a perfect sink or a "partial" sink.

Bibliography

[Aboy et al., 2005] Aboy, M., Pelaz, L., Marques, L. A., López, P., Barbolla, J., Duffy, R., Venezia, V. C., and Griffin, P. B. (2005). Role of silicon interstitials in boron cluster dissolution. *Appl. Phys. Lett.*, 86:031908.

[Allen and Tildesley, 1987] Allen, M. P. and Tildesley, D. J. (1987). *Computer Simulation of Liquids.* Oxford University Press, New York.

[Arias et al., 1995] Arias, J., Jaraiz, M., Pelaz, L., Bailon, L. A., and Barbolla, J. (1995). Low energy ion implantation simulation using a modified binary collision approximation code. *Nucl. Instr. Meth. B*, 102:228–231.

[Avci et al., 2001] Avci, I., Law, M. E., Kuryliw, E., and Jones, K. S. (2001). Modeling the nucleation and evolution of end of range dislocation loops in silicon. In *IEDM Tech. Dig.* IEDM.

[Avci et al., 2004] Avci, I., Law, M. E., Kuryliw, E., Saavedra, A. F., and Jones, K. S. (2004). Modeling extended defects ({311} and dislocation) nucleation and evolution in silicon. *J. Appl. Phys.*, 95(5):2452–2460.

[Baranova et al., 1973] Baranova, E. C., Gusev, V. M., Martynenko, Y. V., Starinin, C. V., and Haibullin, I. B. (1973). On silicon amorphization during different mass ion implantation. *Radiat. Eff.*, 18:21–26.

[Battaglia et al., 1991] Battaglia, A., Priolo, F., and Rimini, E. (1991). Influence of doping on ion-induced growth and shrinkage of partial damage in silicon. *Nucl. Instr. Meth. B*, 59/60:382–385.

[Bedrossian et al., 1997] Bedrossian, P. J., Caturla, M. J., and Diaz de la Rubia, T. (1997). Damage evolution and surface defect segregation in low-energy ion-implanted silicon. *Appl. Phys. Lett.*, 70(2):176–178.

[Blöchl et al., 1993] Blöchl, P. E., Smargiassi, E., Car, R., Laks, D. B., Andreoni, W., and Pantelides, S. T. (1993). First-principles calculations of self-diffusion constants in silicon. *Phys. Rev. Lett.*, 70(16):2435–2438.

[Bonafos et al., 1998] Bonafos, C., Mathiot, D., and Claverie, A. (1998). Ostwald ripening of end-of-range defects in silicon. *J. Appl. Phys.*, 83(6):3008–3017.

[Bonafos et al., 1997] Bonafos, C., Omri, M., de Mauduit, B., BenAssayag, G., Claverie, A., Alquier, D., Martinez, A., and Mathiot, D. (1997). Transient enhanced diffusion of boron in presence of end-of-range defects. *J. Appl. Phys.*, 82(6):2855–2861.

[Bongiorno et al., 2000] Bongiorno, A., Colombo, L., Cargnoni, F., Gatti, C., and Rosati, M. (2000). Evolution of energetics and bonding of compact self-interstitial clusters in Si. *Europhys. Lett.*, 50(5):608–614.

[Bongiorno et al., 1998] Bongiorno, A., Colombo, L., and Diaz de la Rubia, T. (1998). Structural and binding properties of vacancy clusters in silicon. *Europhys. Lett.*, 43(6):695–700.

[Bracht et al., 1995] Bracht, H., Stolwijk, N. A., and Mehrer, H. (1995). Properties of intrinsic point defects in silicon determined by zinc diffusion experiments under nonequilibrium conditions. *Phys. Rev. B*, 52(23):16542–16560.

[Calvo et al., 2004] Calvo, P., Claverie, A., Cherkashin, N., Colombeau, B., Lamrani, Y., de Mauduit, B., and Cristiano, F. (2004). Thermal evolution of {113} defects in silicon: transformation against dissolution. *Nucl. Instr. Meth. B*, 216:173–177.

[Campisano et al., 1993] Campisano, S. U., Coffa, S., Raineri, V., Priolo, F., and Rimini, E. (1993). Mechanisms of amorphization in ion implanted crystalline silicon. *Nucl. Instrum. Meth. B*, 80/81:514–518.

[Castrillo et al., 2005] Castrillo, P., Martin-Bragado, I., Pinacho, R., Jaraiz, M., Rubio, J. E., Mok, K. R. C., Miguel-Herrero, F. J., and Barbolla, J. (2005). Physically-based modeling of dislocation loops in ion implantation processing in silicon. *Mat. Sci. Eng. B*, 124-125:404–408.

[Caturla et al., 1996] Caturla, M. J., Diaz de la Rubia, T., Marques, L. A., and Gilmer, G. H. (1996). Ion-beam processing of silicon at keV energies: A molecular-dynamics study. *Phys. Rev. B*, 54(23):16683.

[Caughey and Thomas, 1967] Caughey, D. M. and Thomas, R. E. (1967). Carrier mobilities in silicon empirically related to doping and field. In *Proceedings of the IEEE, December 1967*, pages 2192–2193.

[Cerva and Hobler, 1992] Cerva, H. and Hobler, G. (1992). Comparison of transmission electron microscope cross sections of amorphous regions in ion implanted silicon with point-defect density calculations. *J. Electrochem. Soc.*, 139(12):3631–3639.

[Chao et al., 1997] Chao, H. S., Griffin, P. B., and Plummer, J. D. (1997). The influence of amorphizing implants on boron diffusion in silicon. In *Mat. Res. Soc. Symp. Proc. Vol 469*, volume 469, pages 347–352. Mat. Res. Soc.

[Cherkashin et al., 2004] Cherkashin, N., Calvo, P., Cristiano, F., de Mauduit, B., and Claverie, A. (2004). On the “Life” of {113} Defects. In *Mat. Res. Soc. Symp. Proc. Vol 810*, volume 810, page C3.7. Mat. Res. Soc.

[Chichkine et al., 2002] Chichkine, M. P., de Souza, M. M., and Narayanan, E. M. S. (2002). Growth of precursors in silicon using pseudopotential calculations. *Phys. Rev. Lett.*, 88(8):085501–1–085501–4.

[Christel et al., 1981] Christel, L. A., Gibbons, J. F., and Sigmon, T. W. (1981). Displacement criterion for amorphization of silicon during ion implantation. *J. Appl. Phys.*, 52:7143–7146.

[Claverie et al., 2000] Claverie, A., Colombeau, B., Assayag, G. B., Bonafos, C., Cristiano, F., Omri, M., and de Mauduit, B. (2000). Thermal evolution of extended defects in implanted Si: Impact on dopant diffusion. *Mater. Sci. Semicond. Process.*, 3:269–277.

[Claverie et al., 2002] Claverie, A., Colombeau, B., Cristiano, F., Altibelli, A., and Bonafos, C. (2002). Modeling of the Ostwald ripening of extrinsic defects and transient enhanced diffusion in silicon. *Nucl. Instrum. Meth. B*, 186:281–286.

[Colombeau et al., 2003] Colombeau, B., Cowern, N. E. B., Cristiano, F., Calvo, P., Cherkashin, N., Lamrani, Y., and Claverie, A. (2003). Time evolution of the depth profile of {113} defects during transient enhnaced diffusion in silicon. *Appl. Phys. Lett.*, 83(10):1953–1955.

[Colombeau et al., 2001] Colombeau, B., Cristiano, F., Marrot, J.-C., Ben Assayag, G., and Claverie, A. (2001). Effect of the ge preamorphisation dose on the thermal evolution of End of Range defects. In *Mat. Res. Soc. Sym. Proc.*, volume 669, pages J481–J486. Mat. Res. Soc.

[Colombeau et al., 2004] Colombeau, B., Smith, A. J., Cowern, N. E. B., Lerch, W., Paul, S., Pawlak, B. J., Cristiano, F., Hebras, X., Bolze, D., Ortiz, C., and Pichler, P. (2004). Electrical deactivation and diffusion of boron in preamorphized ultrashallow junctions: Interstitial transport and F co-implant control. In *IEDM Tech. Dig.*, pages 971–974. IEDM.

[Corlinge, 2004] Corlinge, J. P. (2004). *Silicon-On-Insulator Technology: Materials to VLSI.* Kluwer Academic Publishers, 3 edition.

[Cowern et al., 1999a] Cowern, N. E. B., Alquier, D., Omri, M., Claverie, A., and Nejim, A. (1999a). Transient enhanced diffusion in preamorphized silicon: the role of the surface. *Nucl. Instrum. Meth. B*, 148:257–261.

[Cowern et al., 1999b] Cowern, N. E. B., Jaraiz, M., Cristiano, F., Claverie, A., and Mannino, G. (1999b). Fundamental diffusion issues for deep-submicron device processing. In *IEDM Tech. Dig.*, pages 333–336. IEDM.

[Cowern et al., 1999c] Cowern, N. E. B., Mannino, G., Stolk, P. A., Roozeboom, F., Huizing, H. G. A., van Berkum, J. G. M., Cristiano, F., Claverie, A., and Jaraiz, M. (1999c). Energetics of self-interstitial clusters in Si. *Phys. Rev. Lett.*, 82(22):4460–4463.

[Cowern et al., 1994] Cowern, N. E. B., van de Walle, G. F. A., Zalm, P. C., and Vandenhoudt, D. W. E. (1994). Mechanisms of implant damage annealing and transient enhanced diffusion in Si. *Appl. Phys. Lett.*, 65(23):2981–2983.

[Cristiano et al., 2004] Cristiano, F., Cherkashin, N., Calvo, P., Lamrani, Y., Hebras, X., Claverie, A., Lerch, W., and Paul, S. (2004). Thermal stability of boron electrical activation in preamorphised ultra-shallow junctions. *Mat. Sci. Eng. B*, 114-115:174–179.

[Cristiano et al., 2000] Cristiano, F., Grisolia, J., Colombeau, B., Omri, M., de Mauduit, B., Claverie, A., Giles, L. F., and Cowern, N. E. B. (2000). Formation energies and relative stability of perfect and faulted dislocation loops in silicon. *J. Appl. Phys.*, 87(12):8420–8428.

[Crosby et al., 2003] Crosby, R. T., Jones, K. S., Law, M. E., Larsen, A. N., and Hansen, J. L. (2003). {311} Defect evolution in Si-implanted $Si_{1-x}Ge_x$ alloys. *Mater. Sci. Semicond. Process.*, 6:205–208.

[Csepregi et al., 1977] Csepregi, L., Kennedy, E. F., Gallagher, T. J., Mayer, J. W., and Sigmon, T. W. (1977). Reordering of amorphous layers of Si implanted with ^{31}P, ^{75}As and ^{11}B ions. *J. Appl. Phys.*, 48(10):4234–4240.

[Csepregi et al., 1978] Csepregi, L., Kennedy, E. F., Mayer, J. W., and Sigmon, T. W. (1978). Substrate-orientation dependence of the epitaxial regrowth rate from Si-implanted amorphous Si. *J. Appl. Phys.*, 49(7):3906–3911.

[Csepregi et al., 1975] Csepregi, L., Mayer, J. W., and Sigmon, T. W. (1975). Channeling effect measurements of the recrystallization of amorphous Si layers on crystal Si. *Phys. Lett.*, 54A(2):157–158.

[Davies et al., 1975] Davies, J. A., Foti, G., Howe, L. M., Mitchell, J. B., and Winterbon, K. B. (1975). Polyatomic-ion implantation damage in silicon. *Phys. Rev. Lett.*, 34(23):1441–1444.

[de Mauduit et al., 1994] de Mauduit, B., Laanab, L., Bergaud, C., Faye, M. M., Martinez, A., and Claverie, A. (1994). Identification of EOR defects due to the regrowth of amorphous layers created by ion bombardment. *Nucl. Instrum. Meth. B*, 84:190–194.

[Dennis and Hale, 1976] Dennis, J. R. and Hale, E. B. (1976). Energy dependence of amorphizing implant dose in silicon. *Appl. Phys. Lett.*, 29(9):523–525.

[Dennis and Hale, 1978] Dennis, J. R. and Hale, E. B. (1978). Crystalline to amorphous transformation in ion-implanted silicon: A composite model. *J. Appl. Phys.*, 49(3):1119–1127.

[Diaz de la Rubia and Gilmer, 1995] Diaz de la Rubia, T. and Gilmer, G. H. (1995). Structural transformations and defect production in ion implanted silicon: A molecular dynamics simulation study. *Phys. Rev. Lett.*, 74(13):2507–2510.

[Donnelly et al., 2003] Donnelly, S. E., Birtcher, R. C., Vishnyakov, V. M., and Carter, G. (2003). Annealing of isolated amorphous zones in silicon. *Appl. Phys. Lett.*, 82(12):1860.

[Eaglesham et al., 1994] Eaglesham, D. J., Stolk, P. A., Gossmann, H. J., and Poate, J. M. (1994). Implantation and transient B diffusion in Si: The source of the interstitials. *Appl. Phys. Lett.*, 65(18):2305–2307.

[Elliman et al., 1988] Elliman, R. G., Linnros, J., and Brown, W. L. (1988). Amorphization of silicon by ion irradiation: The role of the divacancy. In *Mat. Res. Soc. Symp. Proc. Vol. 100*, pages 363–368.

[Fahey et al., 1989] Fahey, P. M., Griffin, P. B., and Plummer, J. D. (1989). Point defects and dopant diffusion in silicon. *Reviews of Modern Physics*, 61(2):289–384.

[FRENTECH, 2004] FRENTECH (2004). IST Project 2000-30129, Front-end models for silicon future technology (FRENTECH), Public Final Report.

[Gencer and Dunham, 1997] Gencer, A. H. and Dunham, S. T. (1997). A predictive model for transient enhanced diffusion based on evolution of {311} defects. *J. Appl. Phys.*, 81(2):631–636.

[Gencer and Dunham, 2002] Gencer, A. H. and Dunham, S. T. (2002). A combined model for {311} defect and dislocation loop evolution: Analytical formulation of kinetic precipitation model. *J. Appl. Phys.*, 91(5):2883–2889.

[Gibbons, 1972] Gibbons, J. F. (1972). Ion implantation in semiconductors-Part II: Damage production and annealing. In *Proc. IEEE*, volume 60, page 1062. IEEE.

[Giles, 1991] Giles, M. (1991). Transient phosphorus diffusion below the amorphization threshold. *Journal of the Electrochemical Society*, 138(4):1160.

[Goldberg et al., 1995] Goldberg, R. D., Williams, J. S., and Elliman, R. G. (1995). Amorphization of silicon by elevated temperature ion irradiation. *Nucl. Instrum. Meth. B*, 106:242–247.

[Gutierrez et al., 2001] Gutierrez, A. F., Jones, K. S., and Downey, D. F. (2001). Defect evolution from low energy, amorphizing, Germanium implants on Silicon. In *Mat. Res. Soc. Symp. Proc. Vol 669*, volume 669, page J5.11. Mat. Res. Soc.

[Hamilton et al., 2005] Hamilton, J. J., Collart, E. J. H., Colombeau, B., Jeynes, C., Bersani, M., Giubertoni, D., Sharp, J. A., Cowern, N. E. B., and Kirkby, K. J. (2005). Electrical activation of solid-phase epitaxially regrown ultra-low energy boron implants in Ge preamorphised silicon and SOI. *Nucl. Instrum. Meth. B*, 237:107–112.

[Haynes and Holland, 1991] Haynes, T. E. and Holland, O. W. (1991). Dose rate effects on damage formation in ion-implanted galium arsenide. *Nucl. Instrum. Meth. B*, 59/60:1028–1031.

[Hernandez-Mangas et al., 2002] Hernandez-Mangas, J. M., Arias, J., Bailon, L., Jaraiz, M., and Barbolla, J. (2002). Improved binary collision approximation ion implant simulators. *J. Appl. Phys.*, 91(2):658–667.

[Hernandez-Mangas et al., 2005] Hernandez-Mangas, J. M., Arias, J., Marques, L. A., Ruiz-Bueno, A., and Bailon, L. (2005). Dose-rate and temperature dependent statistical damage accumulation model for ion implantaion into silicon. *Nucl. Instr. Meth. B*, 228:235–239.

[Hobler and Otto, 2003] Hobler, G. and Otto, G. (2003). Status and open problems in modeling of as-implanted damage in silicon. *Mater. Sci. Semicond. Process.*, 6:1–14.

[Hobler and Rafferty, 1999] Hobler, G. and Rafferty, C. S. (1999). Modeling of {311} defects. In *Si Front End Processing*, volume 568, pages 123–134. Materials Research Society.

[Holland et al., 1988] Holland, O. W., El-Ghor, M. K., and White, C. W. (1988). Damage nucleation and annealing in MeV ion-implanted Si. *Appl. Phys. Lett.*, 53(14):1282.

[Holland et al., 1985] Holland, O. W., Fathy, D., and Narayan, J. (1985). Dose rate effects in silicon during heavy ion irradiation. *Nucl. Instrum. Meth. B*, 10/11:565–568.

[Holland et al., 1989] Holland, O. W., Pennycook, S. J., and Albert, G. L. (1989). New model for damage accumulation in Si during self-ion irradiation. *Appl. Phys. Lett.*, 55(24):2503–2505.

[Holland and White, 1991] Holland, O. W. and White, C. W. (1991). Ion-induced damage and amorphization in Si. *Nucl. Instrum. Meth. B*, 59/60:353.

[Holland et al., 1996] Holland, O. W., Xie, L., Nielsen, B., and Zhou, D. S. (1996). Implantation of Si under extreme conditions: The effects of high temperature and dose on damage accumulation. *J. Electron. Mater.*, 25(1):99–106.

[Howe and Rainville, 1981] Howe, L. M. and Rainville, M. H. (1981). Features of collision cascades in silicon as determined by transmission electron microscopy. *Nucl. Instrum. Meth.*, 182/183:143–151.

[Hu, 1994] Hu, S. M. (1994). Nonequilibrium point defects and diffusion in silicon. *Mater. Sci. Eng., R*, 13:105–192.

[Jackson, 1988] Jackson, K. A. (1988). A defect model for ion-induced crystallization and amorphization. *J. Mater. Res.*, 3:1218.

[Jain et al., 2002] Jain, S. C., Schoenmaker, W., Lindsay, R., Stolk, P. A., Decoutere, S., Willander, M., and Maes, H. E. (2002). Transient enhanced diffusion of boron in Si. *J. Appl. Phys.*, 91(11):8919–8941.

[Jaraiz, 2004] Jaraiz, M. (2004). Atomistic simulations in materials processing. In Dabrowski, J. and Weber, E. R., editors, *Predictive Simulation of Semiconductor Processing: Status and Challenges*, page 73, Berlin. Springer-Verlag.

[Jaraiz et al., 1993] Jaraiz, M., Arias, J., Rubio, J. E., Bailon, L. A., and Barbolla, J. (1993). Computer simulation of point-defect distributions generated by ion implantation. *Nucl. Instrum. Meth. B*, 80-81:172–175.

[Jaraiz et al., 2001] Jaraiz, M., Castrillo, P., Pinacho, R., Martin-Bragado, I., and Barbolla, J. (2001). Atomistic front-end process modeling: a powerful tool for deep-submicron device fabrication. In Tsoukalas, D. and Tsamis, C., editors, *Simulation of Semiconductor Processes and Devices 2001*, pages 10–17.

[Jaraiz et al., 1996] Jaraiz, M., Gilmer, G. H., Poate, J. M., and de la Rubia, T. D. (1996). Atomistic calculations of ion implantation in Si: Point defect and transient enhanced diffusion phenomena. *Appl. Phys. Lett.*, 68(3):409–411.

[Jaraiz et al., 1998] Jaraiz, M., Pelaz, L., Rubio, E., Barbolla, J., Eaglesham, D. J., Gossmann, H. J., and Poate, J. M. (1998). Atomistic modeling of point and extended defects in crystalline materials. In *Mat. Res. Soc. Symp. Proc. Vol. 532*, pages 43–53. Mat. Res. Soc.

[Jenčič and Robertson, 1996] Jenčič, I. and Robertson, I. M. (1996). Low-energy electron beam induced regrowth of isolated amorphous zones in Si and Ge. *J. Mater. Res.*, 11(9):2152–2157.

[Jin et al., 2002] Jin, J.-Y., Liu, J., Jeong, U., Mehta, S., and Jones, K. (2002). Study of reverse annealing behaviours of p^+/n ultrashallow junction formed using solid phase epitaxial annealing. *J. Vac. Sci. Technol., B*, 20(1):422–426.

[Jones and Rozgonyi, 1993] Jones, K. S. and Rozgonyi, G. A. (1993). Extended Defects from Ion Implantation and Annealing. In Fair, R. B., editor, *Rapid Thermal Processing: Science and Technology*, pages 123–168, Boston. Academic Press.

[Karmouch et al., 2005] Karmouch, R., Mercure, J.-F., Anahory, Y., and Schiettekatte, F. (2005). Concentration and ion-energy-independent annealing kinetics during ion-implanted-defect annealing. *Appl. Phys. Lett.*, 86:031912.

[Kennedy et al., 1977] Kennedy, E. F., Csepregi, L., Mayer, J. W., and Sigmon, T. W. (1977). Influence of ^{16}O, ^{12}C, ^{14}N, and noble gases on the crystallization of amorphous Si layers. *J. Appl. Phys.*, 48(10):4241–4246.

[Kim et al., 2000] Kim, J., Kirchhoff, F., Wilkins, J. W., and Khan, F. S. (2000). Stability of Si-interstitial defects: From point to extended defects. *Phys. Rev. Lett.*, 84(3):503–506.

[Kim et al., 1997] Kim, J., Wilkins, J. W., Khan, F. S., and Canning, A. (1997). Extended si {311} defects. *Phys. Rev. B*, 55(24):16186–16197.

[Klein et al., 1991] Klein, K. M., Park, C., and Tasch, A. F. (1991). Modeling of cumulative damage effects on ion-implantation profiles. *Nucl. Instrum. Meth. B*, 59/60:60–64.

[Kohyama and Takeda, 1992] Kohyama, M. and Takeda, S. (1992). Atomic structure and energy of the {113} planar interstitial defects in Si. *Phys. Rev. B*, 46(19):12 305–12 316.

[Koyanagi, 2000] Koyanagi, M. (2000). Requirements for junction technology from device design. *Extended abstracts of the first international workshop on junction technology*, 1:1–6.

[Laanab et al., 1993] Laanab, L., Roumili, A., Faye, M. M., Gessinn, N., and Claverie, A. (1993). Temperature dependence of the kinetics of silicon amorphization by he ion implantation. In *Mat. Res. Soc. Symp. Proc. Vol. 279*, pages 529–534.

[Lampin et al., 1999] Lampin, E., Senez, V., and Claverie, A. (1999). Modeling of the transient enhanced diffusion of boron implanted into preamorphized silicon. *J. App. Phys.*, 85(12):8137–8144.

[Law et al., 2000] Law, M. E., Gilmer, G. H., and Jaraiz, M. (2000). Simulation of defects and diffusion phenomena in silicon. *Mat. Res. Soc. Bulletin*, 25(6):45.

[Li and Jones, 1998] Li, J. and Jones, K. S. (1998). {311} defects in silicon: The source of the loops. *Appl. Phys. Lett.*, 73(25):3748–3750.

[Li et al., 1998] Li, J., Law, M. E., Jasper, C., and Jones, K. S. (1998). The effect of tem sample thickness on nucleation and growth and dissolution of {311} defects in Si^+ implanted Si. *Mater. Sci. Semicond. Process.*, 1:99–106.

[Lietoila et al., 1982] Lietoila, A., Wakita, A., Sigmon, T. W., and Gibbons, J. F. (1982). Epitaxial regrowth of intrinsic, ^{31}P-doped and compensated ($^{31}P+^{11}B$-doped) amorphous Si. *J. Appl. Phys.*, 53(6):4399–4405.

[Lim et al., 1995] Lim, D. R., Rafferty, C. S., and Klemens, F. P. (1995). The role of the surface in transient enhanced diffusion. *Appl. Phys. Lett.*, 67:2302–2304.

[Lindhard and Schaff, 1961] Lindhard, J. and Schaff, M. (1961). Energy dissipation by ions in the kev region. *Phys. Rev.*, 124:128.

[Lindsay et al., 2003] Lindsay, R., Pawlak, B., Kittl, J., Henson, K., Torregiani, C., Giangrandi, S., Surdeanu, R., W, V., Mayur, A., Ross, J., McCoy, S., Gelpey, J., Elliott, K., Pages, X., Satta, A., Lauwers, A., Stolk, P., and Maex, K. (2003). A comparison of spike, flash, SPER and laser annealing for 45 nm CMOS. In *Mat. Res. Soc. Proc.*, volume 765, page D7.4. MRS.

[Lindsay et al., 2004] Lindsay, R., Severi, R., Pawlak, B. J., Henson, K., Lauwers, A., Pages, X., Satta, A., Surdeanu, R., Lendzian, H., and Maex, K. (2004). SPER junction optimization in 45 nm CMOS devices. In *The Fourth International Workshop on Junction Technology*, pages 70–75. IEEE.

[Linnros et al., 1988] Linnros, J., Brown, W. L., and Elliman, R. G. (1988). Pulsed ion beam induced crystallization and amorphization of silicon. In *Mat. Res. Soc. Symp. Proc. Vol. 100*, pages 369–374.

[Marques et al., 2003] Marques, L. A., Pelaz, L., Aboy, M., Enriquez, L., and Barbolla, J. (2003). Microscopic description of the irradiation-induced amorphization in silicon. *Phys. Rev. Lett.*, 91(13):135504.

[Marques et al., 2001] Marques, L. A., Pelaz, L., Hernandez, J., Barbolla, J., and Gilmer, G. H. (2001). Stability of defects in crystalline silicon and their role in amorphization. *Phys. Rev. B*, 64:045214.

[Marques et al., 1997] Marques, L. A., Rubio, J. E., Jaraiz, M., Bailon, L. A., and Barbolla, J. (1997). Dose effects on amorphous silicon sputtering by argon ions: A molecular dynamics simulation. *J. Appl. Phys.*, 81(3):1488–1494.

[Martin-Bragado, 2005] Martin-Bragado, I. (2005). *Atomistic Process Simulation in Silicon.* PhD thesis, University of Valladolid.

[Martin-Bragado et al., 2005a] Martin-Bragado, I., Castrillo, P., Jaraiz, M., Pinacho, R., Rubio, J. E., and Barbolla, J. (2005a). Physical atomistic kinetic Monte Carlo modeling of Fermi-level effects of species diffusing in silicon. *Phys. Rev. B*, 72(3):35202–1–8.

[Martin-Bragado et al., 2005b] Martin-Bragado, I., Castrillo, P., Jaraiz, M., Pinacho, R., Rubio, J. E., Barbolla, J., and Moroz, V. (2005b). Fermi-level effects in semiconductor processing: a modeling scheme for atomistic kinetic Monte Carlo simulators. *J. Appl. Phys.*, 98(5):53709–1–7.

[Martin-Bragado et al., 2003] Martin-Bragado, I., Jaraiz, M., Castrillo, P., Pinacho, R., Barbolla, J., and de Souza, M. M. (2003). Mobile silicon di-interstitial: Surface, self-interstitial clustering, and transient enhanced diffusion phenomena. *Phys. Rev. B*, 68(19):195204–1/5.

[Martin-Bragado et al., 2004] Martin-Bragado, I., Jaraiz, M., Castrillo, P., Pinacho, R., Rubio, J. E., and Barbolla, J. (2004). Ion implant simulations: Kinetic Monte Carlo annealing assessment of the dominant features. *Appl. Phys. Lett.*, 84(24):4962–4964.

[Masaki et al., 1993] Masaki, Y., LeComber, P. G., and Fitzgerald, A. G. (1993). Solid phase crystallization of thin films of Si prepared by plasma-enhanced chemical vapor deposition. *J. Appl. Phys.*, 74(1):129–134.

[Maszara and Rozgonyi, 1986] Maszara, W. P. and Rozgonyi, G. A. (1986). Kinetics of damage production in silicon during self-implantation. *J. Appl. Phys.*, 60(7):2310–2315.

[Matsuo et al., 1998] Matsuo, J., Aoki, T., Goto, K., Sugii, T., and Yamada, I. (1998). Ultra shallow junction formation by cluster ion implantation. In *Mat. Res. Soc. Symp. Proc. Vol. 532*, pages 17–22. MRS.

[Mattoni and Colombo, 2004] Mattoni, A. and Colombo, L. (2004). Boron ripening during solid-phase epitaxy of amorphous silicon. *Phys. Rev. B*, 69:045204.

[Mok et al., 2005] Mok, K. R. C., Jaraiz, M., Martin-Bragado, I., Rubio, J. E., Castrillo, P., Pinacho, R., Barbolla, J., and Srinivasan, M. P. (2005). Ion-beam amorphization of semiconductors: A physical model based on the amorphous pocket population. *J. Appl. Phys.*, 98:046104.

[Morehead and Crowder, 1970] Morehead, F. F. and Crowder, B. L. (1970). A model for the formation of amorphous silicon by ion bombardment. *Radiat. Eff.*, 6:27–32.

[Morehead et al., 1972] Morehead, F. F., Crowder, B. L., and Title, R. S. (1972). Formation of amorphous silicon by ion bombardment as a function of ion, temperature, and dose. *J. Appl. Phys.*, 43(3):1112–1118.

[Motooka and Holland, 1992] Motooka, T. and Holland, O. W. (1992). Amorphization processes in ion implanted Si: Ion species effects. *Appl. Phys. Lett.*, 61(25):3005–3007.

[Narayan et al., 1983] Narayan, J., Holland, O. W., and Appleton, B. R. (1983). Solid-phase epitaxial growth and formation of metastable alloys in ion implanted silicon. *J. Vac. Sci. Technol., B*, 1:871–887.

[Nordlund et al., 1998] Nordlund, K., Ghaly, M., Averback, R. S., Caturla, M., Diaz de la Rubia, T., and Tarus, J. (1998). Defect production in collision cascades in elemental semiconductors and fcc metals. *Phys. Rev. B*, 57(13):7556–7570.

[Oen and Robinson, 1976] Oen, O. S. and Robinson, M. T. (1976). "computer studies of the reflection of light ions from solids". *Nucl. Instrum. Meth.*, 132:674.

[Oshiyama et al., 1995] Oshiyama, A., Saito, M., and Sugino, O. (1995). Covalency, elasticity and electron correlation in Si vacancies. *Appl. Surf. Sci.*, 85:239–245.

[Pan and Tu, 1997] Pan, G. Z. and Tu, K. N. (1997). Transmission electron microscopy on {113} rodlike defects and {111} dislocation loops in silicon-implanted silicon. *J. Appl. Phys.*, 82(2):601–608.

[Pawlak et al., 2002] Pawlak, B. J., Lindsay, R., Surdeanu, R., Stolk, P., Maex, K., and Pages, X. (2002). Optimizing p-type ultra-shallow junctions for the 65 nm cmos technology node. In *Proceedings of the 14th International Conference on Ion Implantation Technology*, pages 21–24. IEEE.

[Pawlak et al., 2004] Pawlak, B. J., Surdeanu, R., Colombeau, B., Smith, A. J., Cowern, N. E. B., Lindsay, R., Vandervorst, W., Brijs, B., Richard, O., and Cristiano, R. (2004). Evidence on the mechanism of boron deactivation in Ge-preamorphized ultrashallow junctions. *Appl. Phys. Lett.*, 84(12):2055–2057.

[Pelaz et al., 1997] Pelaz, L., Jaraiz, M., Gilmer, G. H., Gossmann, H.-J., Rafferty, C. S., Eaglesham, D., and Poate, J. M. (1997). B diffusion and clustering in ion implanted si: The role of b cluster precursors. *App. Phys. Lett.*, 70(17):2285–2287.

[Pelaz et al., 2003] Pelaz, L., Marques, L. A., Aboy, M., Barbolla, J., and Gilmer, G. H. (2003). Atomistic modeling of amorphization and recrystallization in silicon. *Appl. Phys. Lett.*, 82(13):2038.

[Pelaz et al., 2004] Pelaz, L., Marques, L. A., and Barbolla, J. (2004). Ion-beam-induced amorphization and recrystallization in silicon. *J. Appl. Phys.*, 96(11):5947–5976.

[Pinacho et al., 2002] Pinacho, R., Castrillo, P., Jaraiz, M., Martin-Bragado, I., and Barbolla, J. (2002). Carbon in silicon: Modeling of diffusion and clustering mechanisms. *J. Appl. Phys.*, 92(3):1582.

[Pinacho et al., 2005] Pinacho, R., Jaraiz, M., Castrillo, P., Martin-Bragado, I., Rubio, J. E., and Barbolla, J. (2005). Modeling arsenic deactivation through arsenic-vacancy clusters using an atomistic kinetic Monte Carlo approach. *Appl. Phys. Lett.*, 86:252103–1–3.

[Posselt et al., 2001] Posselt, M., Bischoff, L., and Teichert, J. (2001). Influence of dose rate and temperature on ion-beam-induced defect evolution in Si investigated by channeling implantation at different doses. *Appl. Phys. Lett.*, 79(10):1444–1446.

[Priolo et al., 1990a] Priolo, F., Battaglia, A., Nicotra, R., and Rimini, E. (1990a). Low-temperature reordering in partially amorphized Si crystals. *Appl. Phys. Lett.*, 57(8):768–770.

[Priolo et al., 1990b] Priolo, F., Spinella, C., and Rimini, E. (1990b). Phenomenological description of ion-beam-induced epitaxial crystallization of amorphous silicon. *Phys. Rev. B*, 41(8):5235–5242.

[Prussin and Zhang, 1996] Prussin, S. and Zhang, P. F. (1996). A physical model fo the role of dose and dose rate on amorphous depth generation. In *Proceedings of the 11th International Conference on Ion Implantation Technology*, pages 555–558. IEEE.

[Richie et al., 2004] Richie, D. A., Kim, J., Barr, S. A., Hazzard, K. R. A., Henning, R., and Wilkins, J. W. (2004). Complexity of small silicon self-interstitial defects. *Phys. Rev. Lett.*, 92(4):045501.

[Robertson et al., 2000] Robertson, L. S., Jones, K. S., Rubin, L. M., and Jackson, J. (2000). Annealing kinetics of {311} defects and dislocation loops in the end-of-range damage region of ion implanted silicon. *J. Appl. Phys.*, 87(6):2910–2913.

[Robertson et al., 1997] Robertson, L. S., Lilak, A., Law, M. E., Jones, K. S., Kringhoj, P. S., Rubin, L. M., Jackson, J., Simons, D. S., and Chi, P. (1997). The effect of dose rate on interstitial release from the end-of-range implant damage region in silicon. *Appl. Phys. Lett.*, 71(21):3105–3107.

[Robinson, 1989] Robinson, M. T. (1989). Slowing down time of energetic atoms in solids. *Phys. Rev. B*, 40(16):10717.

[Robinson and Torrens, 1974] Robinson, M. T. and Torrens, I. M. (1974). Computer simulation of atomic-displacement cascades in solids in the binary-collision approximation. *Phys. Rev. B*, 9:5008.

[Roorda and Sinke, 1989] Roorda, S. and Sinke, W. C. (1989). Rapid nucleation in pulsed laser heated amorphous Si. *Appl. Surf. Sci.*, 36:588–596.

[Rubio et al., 2005] Rubio, J. E., Jaraiz, M., Martin-Bragado, I., Castrillo, P., Pinacho, R., and Barbolla, J. (2005). Dose loss and segregation of boron and arsenic at the Si/SiO_2 interface by atomistic kinetic Monte Carlo simulations. *Mat. Sci. Eng. B*, 124-125:392–396.

[Rubio et al., 2003] Rubio, J. E., Jaraiz, M., Martin-Bragado, I., Hernandez-Mangas, J. M., Barbolla, J., and Gilmer, G. H. (2003). Atomistic Monte Carlo simulations of three-dimensional polycrystalline thin films. *J. App. Phys.*, 94(1):163–168.

[Saavedra et al., 2004] Saavedra, A. F., Jones, K. S., Law, M. E., Chan, K. K., and Jones, E. C. (2004). Electrical activation in silicon-on-insulator after low energy boron implantation. *J. Appl. Phys.*, 96(4):1891–1898.

[Schultz et al., 1991] Schultz, P. J., Jagadish, C., Ridgway, M. C., Elliman, R. G., and Williams, J. S. (1991). Crystalline-to-amorphous transition for Si-ion irradiation of Si(100). *Phys. Rev. B*, 44(16):9118–9121.

[Semiconductor Industry Association, 2005] Semiconductor Industry Association (2005). International technology roadmap for semiconductors. http://public.itrs.net.

[Solmi et al., 1991] Solmi, S., Baruffaldi, F., and Canteri, R. (1991). Diffusion of boron in silicon during post implantation annealing. *J. Appl. Phys.*, 69(4):2135–2142.

[Stolk et al., 1997] Stolk, P. A., Gossmann, H. J., Eaglesham, D. J., Jacobson, D. C., Rafferty, C. S., Gilmer, G. H., Jaraiz, M., Poate, J. M., Luftman, H. S., and Haynes, T. E. (1997). Physical mechanism of transient enhanced dopant diffusion in ion-implanted silicon. *J. Appl. Phys.*, 81(9):6031–6050.

[Suni et al., 1982] Suni, I., Göltz, G., Grimaldi, M. G., Nicolet, M.-A., and Lau, S. S. (1982). Compensating impurity effect on epitaxial regrowth rate of amorphized Si. *Appl. Phys. Lett.*, 40(3):269–271.

[SYNOPSYS, 2005a] SYNOPSYS (2005a). Floops-ISE User's Guide version w-2005.10.

[SYNOPSYS, 2005b] SYNOPSYS (2005b). TSuprem-4 User's Guide version w-2005.10.

[Takeda, 1991] Takeda, S. (1991). An atomic model of electron-irradiation-induced defects on {113} in Si. *Jap. J. Appl. Phys.*, 30(4A):639–642.

[Tsai and Streetman, 1979] Tsai, M. Y. and Streetman, B. G. (1979). Recrystallization of implanted amorphous silicon layers. i. Electrical properties of silicon implanted with ${BF_2}^+$ or $Si^+ + B^+$. *J. Appl. Phys.*, 50(1):183–187.

[Venezia et al., 2003] Venezia, V. C., Duffy, R., Pelaz, L., Aboy, M., Heringa, A., Griffin, P. B., Wang, C. C., Hopstaken, M. J. P., Tamminga, Y., Dao, T., Pawlak, B. J., and Roozeboom, F. (2003). Dopant redistribution effects in preamorphized silicon during low temperature annealing. In *IEDM 2003 proceedings*. IEDM.

[Vieu et al., 1989] Vieu, C., Claverie, A., Faure, J., and Beauvillain, J. (1989). A spatial damage energy distribution calculation for ion-implanted materials. *Nucl. Instrum. Meth. B*, 36(2):137–147.

[Wang et al., 1985] Wang, K.-W., Spitzer, W. G., Hubler, G. K., and Sadana, D. K. (1985). Ion implantation of si by ^{12}C, ^{29}Si, and ^{120}Sn: Amorphization and annealing effects. *J. Appl. Phys.*, 58:4553–4564.

[Watkins, 2000] Watkins, G. D. (2000). Intrinsic defects in silicon. *Mater. Sci. Semicond. Process.*, 3(4):227–235.

[Westmoreland et al., 1969] Westmoreland, J. E., Mayer, J. W., Eisen, F. H., and Welch, B. (1969). Production and annealing of lattice disorder in silicon by 200-keV boron ions. *Appl. Phys. Lett.*, 15(9):308–310.

[Williams et al., 1985] Williams, J. S., Elliman, R. G., Brown, W. L., and Seidel, T. E. (1985). Dominant influence of beam-induced interface rearrangement on solid-phase epitaxial crystallization of amorphous silicon. *Phys. Rev. Lett.*, 55(14):1482–1485.

[Wittmer et al., 1978] Wittmer, M., Roth, J., Revesz, P., and Mayer, J. W. (1978). Epitaxial regrowth of Ne- and Kr-implanted amorphous silicon. *J. Appl. Phys.*, 49(10):5207–5212.

[Ziegler et al., 1985] Ziegler, J. F., Biersack, J. P., and Littmark, U. (1985). *The Stopping and Range of Ions in Solids*. Pergamon, New York.

Appendix

A. Sheet Resistance Calculation

```
#include <stdio.h>
#include <stdlib.h>
#include <math.h>
#include <string.h>

main(){

float q, x[600], conc[600], miu[600], miuconc[600], miua[600],
miub[600], tabconc[36], emiu[36], hmiu[36], concXj, delx, invRs, Rs;

int i, j, numelem, carriertype, mobility, Xj, method;

FILE *infile, *table;

q=1.6022e-19;

//Initialize arrays
for (j=0; j<256; j++)
{
x[j]=0;
conc[j]=0;
miuconc[j]=0;
}

for (j=0; j<36; j++)
{
tabconc[j]=0;
emiu[j]=0;
hmiu[j]=0;
}

//Read infile
infile=fopen("Concentration.txt", "r");
j=0;
while ( fscanf(infile, "%f %f ", &x[j], &conc[j]) !=EOF) j++;
numelem=j;
fclose(infile);

table=fopen("mobility.txt", "r");
j=0;
for (j=0; j<36; j++)
{ fscanf(table, "%e %f %f ", &tabconc[j], &emiu[j], &hmiu[j]);  }
```

```
fclose(table);

delx=(x[1]-x[0])*1e-7; //in cm

printf ("Please choose empirical mobility[1]
or tabulated mobility[2]\n");
scanf ("%d", &mobility);

printf ("Please choose electron[1] or hole[2] carriers\n");
scanf ("%d", &carriertype);

concXj = 1e17;

j = 0;
if (mobility==1)
{
while (conc[j]>concXj)
{
if (carriertype==1) //electron
{
miu[j]=55.24+((1429.23-55.24)/(1+pow((conc[j]/1.072e17),0.73)));
miuconc[j]=miu[j]*conc[j];

Xj=j+1;
j++;
}
else if (carriertype==2) //hole
{
miu[j]=49.7+((479.37-49.7)/(1+pow((conc[j]/1.606e17),0.7)));
miuconc[j]=miu[j]*conc[j];

Xj=j+1;
j++;
}
}
}
else if (mobility==2)
{
while (conc[j]>concXj)
{
i=0;
while (conc[j]>tabconc[i])
{
i++;
}
if (carriertype==1)
{
if (conc[j]>tabconc[35])
```

```
{
miuconc[j]=conc[j]*emiu[35];
}
else
{
miua[j] = emiu[i-1];
miub[j] = emiu[i];

//Linear Interpolation of mobility
miu[j]=(conc[j]-tabconc[i-1])*(miub[j]
-miua[j])/(tabconc[i]-tabconc[i-1])+miua[j];

miuconc[j]=conc[j]*miu[j];
}
}
else if (carriertype = 2)
{
if (conc[j]>tabconc[35])
{
miuconc[j]=conc[j]*hmiu[35];
}
else
{
miua[j] = hmiu[i-1];
miub[j] = hmiu[i];

//Linear Interpolation of mobility
miu[j]=(conc[j]-tabconc[i-1])*(miub[j]
-miua[j])/(tabconc[i]-tabconc[i-1])+miua[j];

miuconc[j]=conc[j]*miu[j];
}
}

Xj=j+1;
j++;
}
}

invRs = 0;

for (j=1; j<(Xj-1); j++)
{
invRs = invRs +miuconc[j];
}
invRs = q*delx*(invRs+ 0.5*(miuconc[0]+miuconc[Xj-1]));

Rs = 1/invRs;
```

```
printf("Rs = %f \n", Rs);

}//end
```

A.1. Tabulated mobility of electrons and holes from TSUPREM [SYNOPSYS, 2005b].

Concentration	Mobility at 300 K	
(cm^{-3})	Electron	Hole
1e14	1350	495
2e14	1345	495
4e14	1335	495
6e14	1320	495
8e14	1310	495
1e15	1300	491.1
2e15	1248	487.3
4e15	1200	480.1
6e15	1156	473.3
8e15	1115	466.9
1e16	1076	460.9
2e16	960	434.8
4e16	845	396.5
6e16	760	369.2
8e16	720	348.3
1e17	675	331.5
2e17	524	279.0
4e17	385	229.8
6e17	321	203.8
8e17	279	186.9
1e18	252	178.0
2e18	182.5	130.0
4e18	140.6	90.0
6e18	113.6	74.5
8e18	99.5	66.6
1e19	90.5	61.0
2e19	86.9	55.0
4e19	83.4	53.7
6e19	78.8	52.9
8e19	71.6	52.4
1e20	67.8	52.0
2e20	52.0	50.8
4e20	35.5	49.6
6e20	23.6	48.9
8e20	19.0	48.4
1e21	17.8	48.0

List of Publications

1. Mok, K. R. C., Jaraiz, M., Martin-Bragado, I., Rubio, J. E., Castrillo, P., Pinacho, R., Barbolla, J., and Srinivasan, M. P. (2005). Ion-beam amorphization of semiconductors: A physical model based on the amorphous pocket population. *J. Appl. Phys.*, 98:046104.

2. Mok, K. R. C., Jaraiz, M., Martin-Bragado, I., Rubio, J. E., Castrillo, P., Pinacho, R., Srinivasan, M. P, and Bensitant, F. (2005). Comprehensive modeling of ion-implant amorphization in silicon. *Mat. Sci. Eng. B*,124-125:383-385.

3. Mok, K. R. C., Jaraiz, M., Martin-Bragado, I., Rubio, J. E., Castrillo, P., Pinacho, R., Srinivasan, M. P, and Bensitant, F. (2005). Ion-implant simulations: The effect of defect spatial correlation on damage accumulation. *Mat. Sci. Eng. B*, 124-125:386-388.

4. Mok, K. R. C., Jaraiz, M., Martin-Bragado, I., Rubio, J. E., Castrillo, P., Pinacho, R., Srinivasan, M. P, and Bensitant, F. (2005). Bimodal distribution of damage morphology generated by ion implantation. *Mat. Sci. Eng. B*, 124-125:389-391.

5. Mok, K. R. C., Colombeau, B., Jaraiz, M., Castrillo, P., Rubio, J. E., Pinacho, R., Srinivasan, M. P., Benistant, F., Martin-Bragado, I., and Hamilton, J. J. (2006). Modeling and simulation of the influence of SOI structure on damage evolution and USJ formed by Ge Preamorphization Implants and Solid Phase Epitaxial Regrowth. In *Mat. Res. Soc. Sym. Proc.*, volume 923, pages C03-04. Mat. Res. Soc.

6. Castrillo, P., Martin-Bragado, I., Pinacho, R., Jaraiz, M., Rubio, J. E., Mok, K. R. C., Miguel-Herrero, F. J., and Barbolla, J. (2005). Physically based modeling of dislocation loops in ion implantation processing in silicon. *Mat. Sci. Eng. B*,124-125:404-408.

7. Chan, H. Y., Srinivasan, M. P., Benistant, F., Mok, K. R. C., Chan, L., and Jin, H. M. (2006). Continuum modeling of post-implantation damage and the effective plus factor in crystalline silicon at room temperature. *Thin Solid Films*, 504(1-2):269-273.

8. Colombeau, B., Mok, K. R. C., Yeong, S. H., Indanjang, B., Tan, O., Yang, B., Li, Y., Benistant, F., Jaraiz, M., Cowern, N. E. B., and Chu, S. Optimization of nanoCMOS devices using predictive atomistic physics-based process modeling. (to be presented at IEDM, 2006.)